

Kinematics, structure and abundances of supernova remnant 0540-69.3[★]

P. Lundqvist^{1,2}, N. Lundqvist^{1,2}, and Yu. A. Shibano^{3,4}

¹ Department of Astronomy, AlbaNova University Center, Stockholm University, SE-10691 Stockholm, Sweden
e-mail: peter@astro.su.se

² The Oskar Klein Centre, AlbaNova, SE-10691 Stockholm, Sweden

³ Ioffe Institute, Politeknicheskaya 26, St. Petersburg, 194021, Russia

⁴ Peter the Great St. Petersburg Polytechnic University, Politeknicheskaya 29, St. Petersburg, 195251, Russia

Received ?, ?, 2021; accepted ?, ?, 2021

ABSTRACT

Aims. To investigate the structure, elemental abundances, physical conditions and the immediate surroundings of supernova remnant 0540-69.3 in the Large Magellanic Cloud.

Methods. Imaging in [O III] and spectroscopic studies through various slits were utilized using European Southern Observatory's Very Large and New Technology Telescopes. Densities, temperatures and abundances were estimated applying nebular analysis for various parts of the remnant.

Results. Several new spectral lines are identified, both in the pulsar-wind nebula part of the remnant, and in interstellar clouds shocked by the supernova blast wave. In the pulsar-wind nebula, all lines are redshifted by $440 \pm 80 \text{ km s}^{-1}$ with respect to the rest frame of the host galaxy, and a 3D-representation of the [O III] emission displays a symmetry axis of ring-like structures which could indicate that the pulsar shares the same general redshift as the central supernova ejecta. [O II], [S II], [Ar III] and H β share a common more compact structure than [O III], and possibly [Ne III]. The average [O III] temperature in the pulsar-wind nebula is $23\,500 \pm 1\,800 \text{ K}$, and the electron density derived from [S II] is typically $\sim 10^3 \text{ cm}^{-3}$. By mass, the relative elemental abundances of the shocked ejecta in the pulsar-wind nebula are O : Ne : S : Ar $\approx 1 : 0.07 : 0.10 : 0.02$, consistent with explosion models of 13 – 20 M_{\odot} progenitors, and similar to that of SN 1987A, as is also the explosive mixing of hydrogen and helium into the center. From H β and He I $\lambda 5876$, the mass ratio of He/H in the center is estimated to be in excess of ~ 0.8 . The rapid cooling of the shocked ejecta could potentially cause variations in the relative abundances if the ejecta are not fully microscopically mixed, and this is highlighted for S/O for the period 1989–2006. [O III] is also seen in presumably freely coasting photoionized ejecta outside the pulsar-wind nebula at inferred velocities out to well above $2\,000 \text{ km s}^{-1}$, and in projection [O III] is seen out to $\sim 10''$ from the pulsar. This is used to estimate that the pulsar age is $\approx 1\,200$ years. The freely coasting [O III]-emitting ejecta have a strictly non-spherical distribution, and their mass is estimated to be $\sim 0.12 M_{\odot}$. A possible outer boundary of oxygen-rich ejecta is seen in [O II] $\lambda\lambda 3726, 3729$ at $\sim 2\,000 - 2\,100 \text{ km s}^{-1}$. Four filaments of shocked interstellar medium are identified, and there is a wide range in degree of ionization of iron, from Fe⁺ to Fe¹³⁺. One filament belongs to a region also observed in X-rays, and another one has a redshift of $85 \pm 30 \text{ km s}^{-1}$ relative to the host. From this we estimate that the electron density of the [O III]-emitting gas is $\sim 10^3 \text{ cm}^{-3}$, and that the line of the most highly ionized ion, [Fe XIV] $\lambda 5303$, come from an evaporation zone in connection with the radiatively cooled gas emitting, e.g., [O III], and not from immediately behind the blast wave. We do not find evidence for nitrogen-enriched ejecta in the south-western part of the remnant, as was previously suggested. Emission in this region is instead from a severely reddened H II-region.

Key words. ISM: supernova remnants – supernovae: general – pulsars: individual: PSR B0540-69

1. Introduction

Supernova remnant (SNR) 0540-69.3 (henceforth simply 0540) has been observed at wavelengths ranging from X-rays to the radio. Both in the radio and in X-rays, the remnant is bounded by an outer shell, which has a radius of $\sim 20\text{--}35''$ (Manchester et al. 1993b; Gotthelf & Wang 2000). In the optical, the outer shell coincides with two bright filaments to the west and southwest (Mathewson et al. 1980), one emitting [O III] and the other [N II], respectively. As cautioned by these authors, the [N II] filament

may not belong to the remnant, as it coincides with two bright stars.

Inside the outer shell, the emission from the remnant is concentrated to a substantially smaller nebula (Mathewson et al. 1980; Kirshner et al. 1989; Caraveo et al. 1992; Morse 2003; Serafimovich et al. 2005; Lundqvist et al. 2011). In [O III] the diameter of the main emission is $\sim 8''$ (Caraveo et al. 1992). Henceforth we will refer to this as the ‘central part of the SNR’ (SNRC), and in [S II] and H α the observed structures are even smaller and weaker, decreasing in size and strength in this order.

The SNRC also contains an optical continuum source; this is synchrotron emission from the pulsar wind nebula (PWN) (Chanan et al. 1984; Serafimovich et al. 2004; Lundqvist et al. 2011). The synchrotron emission and its spectral characteristics

[★] Based on observations performed at the European Southern Observatory, La Silla and Paranal, Chile (ESO Programmes 56.C-0731 and 68.D-0394).

have been studied throughout the energy range from radio to X-rays (Serafimovich et al. 2004; Lundqvist et al. 2011; Mignani et al. 2012; Brantseg et al. 2014; Lundqvist et al. 2020). A PWN is expected since the remnant harbors the young pulsar (PSR B0540-69 whose pulsed emission has been documented in X-rays (Seward et al. 1984), in the UV (Mignani et al. 2019), in the optical (Middleditch & Pennypacker 1985), and in the radio (Manchester et al. 1993a).

The SNRC with its pulsar bears many similarities to the Crab Nebula, and a detailed discussion and comparison of 0540 with the Crab pulsar and its PWN can be found in Serafimovich et al. (2004). However, as revealed by spectral studies in the optical (Mathewson et al. 1980; Dopita & Tuohy 1984; Kirshner et al. 1989; Morse et al. 2006), the elemental abundances in 0540 are very different from those in the Crab. While the Crab is helium-rich, but not conspicuous in other respects (MacAlpine et al. 1996), 0540 is dominated by forbidden oxygen and sulphur lines, and is classified as an “oxygen-rich SNR” (OSNR). The most studied object in this class is undoubtedly Cas A, which, however, is not pulsar-powered, although it contains a neutron star (Tananbaum 1999; Pavlov et al. 2000). SN 1987A is another case that is now entering its remnant stage, with an oxygen-mass of $\sim 1.8 - 1.9 M_{\odot}$ within its innermost ejecta, i.e., out to $\sim 2000 \text{ km s}^{-1}$ (Kozma & Fransson 1998; Jerkstrand et al. 2011). 0540 makes an interesting link between pulsar-powered remnants in general and OSNRs.

In all the emission lines, projected images on the sky of the SNRC appear to be concentrated to a few blobs (e.g., Lundqvist et al. 2011). In addition, spectroscopy of 0540 by Kirshner et al. (1989) showed that the weighted emission of the SNRC is redshifted with respect to the LMC rest velocity. This was further studied by Morse et al. (2006) who, however, also revealed a faint [O III] “halo” between -1400 and $+1900 \text{ km s}^{-1}$, with the center of expansion close to the systemic velocity of the surrounding H II region. Sandin et al. (2013) used the the integral field unit (IFU) ESO/VLT/VIMOS to probe the 3D structure of the whole SNRC and found that [O III] the full velocity range between $-1650 \leq v_{[\text{O III}]} \leq +1700 \text{ km s}^{-1}$, where $v_{[\text{O III}]}$ is relative to the systemic velocity of local LMC redshift. In the plane of the sky, an [O III] halo can be traced out to $\sim 8''$ from the pulsar (Morse et al. 2006). Williams et al. (2008, who also included infrared observations with the Spitzer Space telescope) interpreted the halo emission to come from photoionized unshocked supernova ejecta outside the PWN, but inside the reverse shock of the SNR. At a distance of 50 kpc, $\sim 8''$ and $v_{[\text{O III}]} \approx 1700 \text{ km s}^{-1}$ would imply an age of $\sim 1.1 \times 10^3$ years for 0540, which is less than the spin down age of the pulsar (1.6×10^3 years, Reynolds 1985).

Spectroscopy and imaging show that there are clear differences, not only in the size of the SNRC, but also in the structure of the emitting gas depending on the emission line traced. In particular, the structures of [O III] and [S II] emission have a very low correlation in the bright southwest part of the SNRC, while the [S II] emission correlates well with continuum emission (Lundqvist et al. 2011). This could be due to differences in the ionization structure as a function of position angle, or it could be difference in elemental structure.

The 3D structure probed by Sandin et al. (2013) shows that [S II] comes from a more central part, $-1200 \leq v_{[\text{S II}]} \leq +1200 \text{ km s}^{-1}$, than [O III] with very weak emission in the $-1200 \leq v_{[\text{S II}]} \leq -800 \text{ km s}^{-1}$ range. Sandin et al. (2013) used the [S II] line to make a map of the electron density, n_e , and found that the [S II] emission mainly comes from regions with $n_e \lesssim 750 \text{ cm}^{-3}$, although there could be “pockets” with

$n_e \sim 2 \times 10^{-3} \text{ cm}^{-3}$. In particular, [S II] emission is strong from a specific feature called “the blob” in our previous papers (Serafimovich et al. 2004, 2005; Lundqvist et al. 2011; Sandin et al. 2013), located $\sim 1'3$ south-west of the pulsar. This blob is conspicuous in continuum emission from radio to X-rays (Lundqvist et al. 2011, 2020), and De Luca et al. (2007) argued for that the blob appears to change position and continuum brightness between 1995 and 2005. Lundqvist et al. (2011) offered the alternative explanation, also including optical polarimetry and X-ray data in their analysis, that a local energy deposition may have occurred around 1999, and that the emission from that faded until later epochs. Sandin et al. (2013) suggested that the energy deposition in the blob region could be due to interaction of the blob with the pulsar-wind torus.

There are also more recent evidence of time-varying emission from the PWN. Ge et al. (2019) showed that the sudden change in the spin-down rate in December 2011 could be linked to a gradual brightening of the PWN in X-rays by $\sim 30\%$ in about ~ 2 years. Lundqvist et al. (2011) suggested that spatial changes in polarization angle along an axis in the northeast-southwest direction, and crossing the blob, point to past changes in activity along this axis. It is intriguing that the presumed pulsar jet has been suggested to point nearly orthogonal to this axis (e.g., Gotthelf & Wang 2000).

Here we report on imaging and spectroscopic observations of 0540 and its immediate surroundings using NTT/EMMI from 1996 and VLT/FORS from 2002 (Sect. 2 & 3). We also include results from Sandin et al. (2013). Since our data are deeper than previously reported spectral studies, our aim is to improve the knowledge about the spatial velocity distribution of various elements, and on the temperature and ionization of the different parts of the remnant and its neighborhood (Sect. 4). We summarize our conclusions in Sect.5. A preliminary version of parts of our work was presented in Serafimovich et al. (2005).

2. Observations and data analysis

2.1. NTT Observations

Observations of 0540 were performed on 1996 January 17, using the 3.58m ESO/NTT equipped with the ESO Multi-Mode Instrument (EMMI). Narrow-band images were obtained in [O III] $\lambda = 5007 \text{ \AA}$ at zero velocity using the [O III]/0 filter¹, and through the [O III]/6000 filter which is shifted to $+6000 \text{ km s}^{-1}$ from the rest wavelength of [O III]. The pixel size was $0'268 \times 0'268$. On the same night we also carried out low-resolution (2.23 \AA/pixel) long-slit spectroscopy of 0540 in the $3850\text{--}8450 \text{ \AA}$ range using the EMMI RILD mode with grism#3². The log of the observations is presented in Table 1. The EMMI [O III]/0 image of the 0540 neighborhood is shown in Fig. 4, where we also show the slit position of the NTT spectral observation (marked by “2”). The position angle of the slit is $\text{PA}=22^\circ$, and the slit crosses the SNRC containing the pulsar and the PWN.

2.2. VLT observations

Further spectral observations were carried out in the $3600\text{--}6060 \text{ \AA}$ range on 2002 January 9 and 10 with the FOCal Reducer/low dispersion Spectrograph (FORS1) on the 8.2m UT3

¹ <http://www.lis.eso.org/lasilla/Telescopes/NEWNTT/emmi/emmiFilters.html>

² <http://www.lis.eso.org/lasilla/Telescopes/NEWNTT/emmi/emmiRild.html>

Table 1. Log of observations of SNR 0540-69.3.

<i>Imaging of 0540</i>						
Telescope	Instrument	Filter	UT	Exp. time (s)	sec z	Seeing ^a (arcsec)
NTT	EMMI	[O III]/0	04:24:54 ^b	900	1.37	1.20
NTT	EMMI	[O III]/6000	05:05:00	900	1.43	1.47
NTT	EMMI	[O III]/0	06:27:17	900	1.62	1.13
<i>Spectroscopy of 0540</i>						
Telescope	Instrument	Range (nm)	UT	Exp. time (s)	sec z	Seeing ^a (arcsec)
NTT	EMMI	385-845	07:26:45 ^c	2200	1.89	1.35
VLT	FORS1	360-606	01:59:32 ^d	1320	1.43	1.25
			02:23:25	1320	1.42	1.30
			02:52:38	1320	1.41	1.18
			03:16:31	1320	1.41	1.12
			03:42:32	1320	1.41	1.24
			04:06:25	1320	1.43	1.09
			04:32:42	1320	1.45	0.88
			02:07:57 ^e	1320	1.42	1.48
			02:31:50	1320	1.41	1.25
			03:39:58	1320	1.42	0.92
VLT	FORS1	360-606	04:03:52	1320	1.43	0.99
			04:30:26	1320	1.46	1.03
			04:54:20	1320	1.49	1.03
<i>Spectroscopy of standard star LTT 3864</i>						
Telescope	Instrument	Range (nm)	UT	Exp. time (s)	sec z	Seeing ^a (arcsec)
NTT	EMMI	385-845	08:14:55 ^b	900	1.91	1.02
VLT	FORS1	360-606	08:51:03 ^f	20	1.03	0.67

^a FWHM from stellar profiles^d 2002 Jan 9, slit “1” in Fig. 1, PA=88°^b 1996 Jan 17^e 2002 Jan 10, slit “3” in Fig. 1, PA=51°^c 1996 Jan 17, slit “2” in Fig. 1, PA=22°^f 2002 Jan 10

(MELIPAL) of ESO/VLT, using the grism GRIS_600B³. This has a dispersion of 50 Å/mm, or 1.18 Å/pixel. The optical path also includes a Linear Atmospheric Dispersion Corrector that compensates for the effects of atmospheric dispersion (Avila et al. 1997). The spatial scale of the FORS1 CCD is 0.2 pixel. On January 9 and 10 we obtained seven and six exposures of 1320 s each, respectively (see Table 1), i.e., a total exposure time of 154 and 132 minutes. The position angles, PA=88° and PA=51°, were the same in all these exposures, and the slit positions are marked by “1” and “3” in Fig. 1, respectively.

Slits 1 (VLT) and 2 (NTT) were chosen to include the SNRC and the pulsar. Slit 3 (VLT) does not cross the SNRC, but was placed west of it to probe the emission from the outer shell that is most clearly identified in the Chandra X-ray images (Hwang et al. 2001, see Fig. 2). All spectroscopic observations (both NTT and VLT) were performed using a slit width of 1” and the seeing was generally about 1”.

2.3. NTT and VLT data reduction

The spatial and spectral images were bias-subtracted and flat-fielded using standard procedures and utilities from the NOAO IRAF package. We used the averaged sigma clipping algorithm

avsigclip with the scale parameter set equal to none to combine the images. Wavelength calibration for the 2D spectral images were done using arc frames obtained with a He/Ar lamp and procedure transform. The spectra of the objects were then extracted from the 2D image using the apall and background tasks. Flux calibration of the spectra was accomplished by comparison to the spectrophotometric standard star LTT 3864 (Hamuy et al. 1994) for both the NTT and VLT spectra. Atmospheric extinction corrections were performed using a spectroscopic extinction table provided by ESO⁴.

2.4. HST and Chandra observations

The SNR 0540-69.3 field has been imaged with the HST several times in various bands. In particular, narrow and medium band filters are useful to compare with our spectral information. The HST data highlighted here are described and discussed in Morse (2003), Morse et al. (2006) and Lundqvist et al. (2011).

To compare the optical and X-ray data we also discuss data retrieved from the Chandra archive. In Lundqvist et al. (2011) we discuss these data in greater detail and how they were reduced.

⁴ <http://www.eso.org/observing/dfo/quality/UVES/files/atmoexan.tfits>

³ <http://www.eso.org/instruments/fors1/grisms.html>

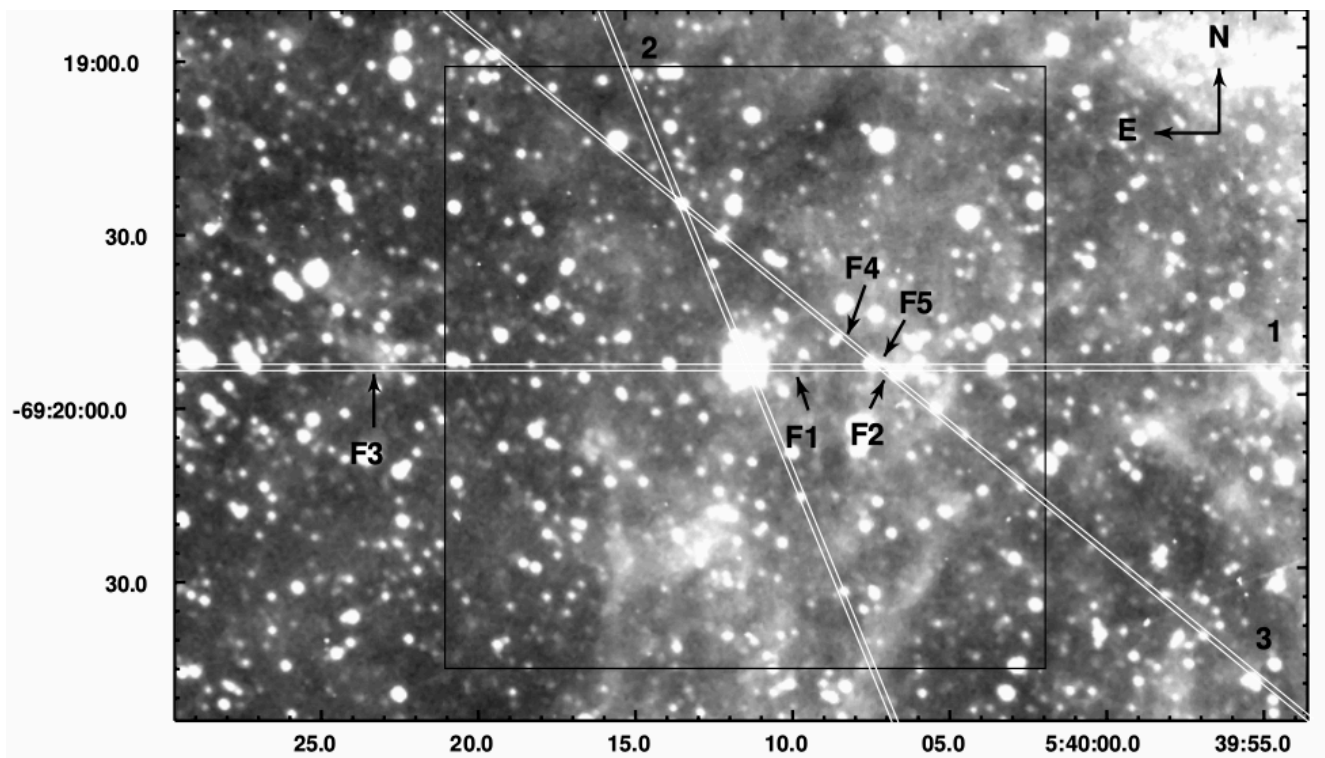


Fig. 1. $3.2' \times 2.0'$ [O III] image of SNR 0540-69.3 obtained with NTT/EMMI in 1996 using the narrow [O III]/0 filter centered at the rest wavelength of [O III] $\lambda 5007$. The bright extended object in the center of the image is the central part of the remnant containing the pulsar. The white lines marked by numbers show the slit positions used at the spectral observations of the SNR with NTT/EMMI (2) and VLT/FORS1 (1 and 3). The areas marked “F1-F5” show the positions of five H II regions identified from the spectral observations and described in the text. A $100'' \times 100''$ black box outline the region shown in Fig. 2.

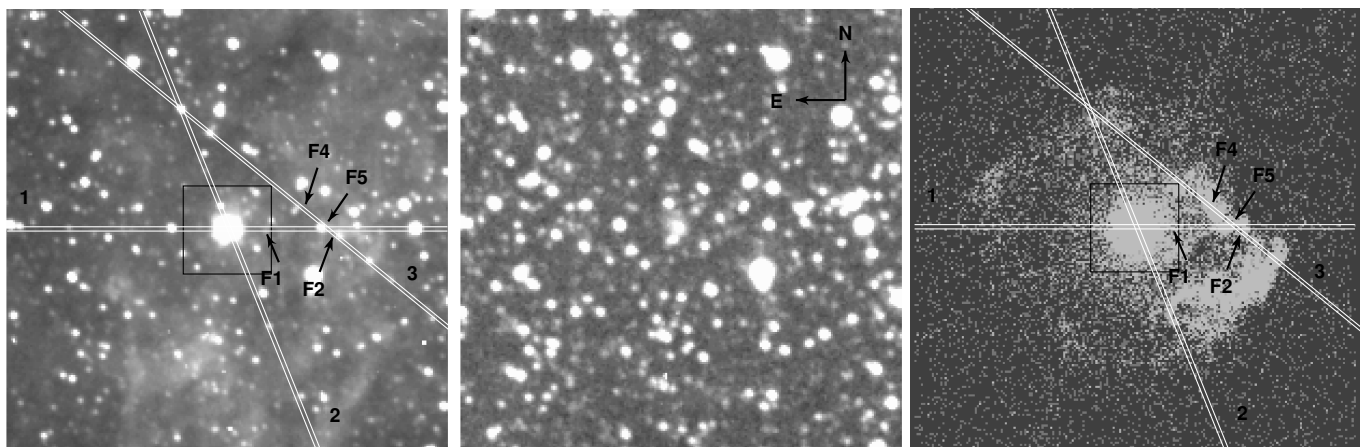


Fig. 2. The $100'' \times 100''$ region of the field around 0540 marked with a box in Fig. 1. The images are obtained in the [O III]/0 (*left*) and [O III]/6000 (*middle*) bands with NTT/EMMI, and in the 1.5–6.4 keV X-ray range (*right*) with Chandra/ACIS (Hwang et al. 2001). The positions of all the slits used in the spectral observations, and of the detected H II regions are marked as in Fig. 1. A $20'' \times 20''$ box marks the inner region of 0540 blown up in Fig. 4. Note that the H II structures named “F1”, “F2”, “F4” and “F5” are projected on regions with strong X-ray emission from the SNR.

3. Results and Discussion

3.1. Imaging

Narrow-band [O III] images of 0540 obtained with NTT/EMMI through the zero velocity and $+6\,000$ km s^{-1} filters ([O III]/0 and [O III]/6000, respectively) are shown in the left and middle panels of Fig. 2, respectively. The FWHM of the transmission curve for both filters corresponds to $3\,300$ km s^{-1} (cf. Fig. 3). The $+6\,000$

km s^{-1} image shows no obvious sign of [O III] emission in any part of the remnant, confirming the spectroscopic observations by Kirshner et al. (1989) who did not find any line emission with redshifts higher than $\sim 3\,000$ km s^{-1} . The only emission seen from the remnant in the $+6\,000$ km s^{-1} image is the continuum radiation from the PWN powered by the pulsar B0540-69.3 in SNRC (see Serafimovich et al. 2004; Lundqvist et al. 2011, for details on the continuum part).

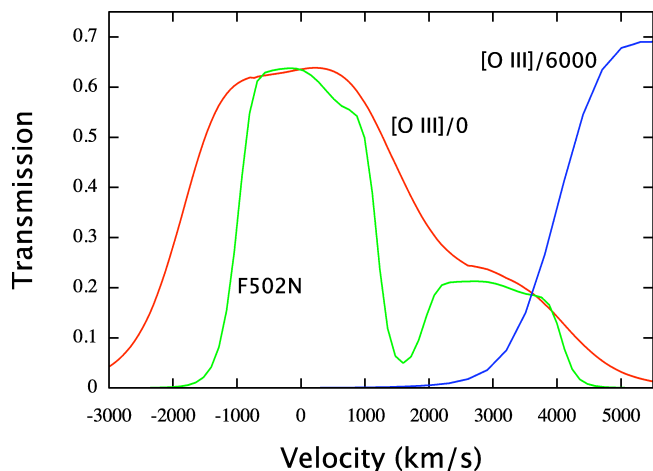


Fig. 3. Effective transmission curves for the ESO/[O III]/0 (red), ESO/[O III]/6000 (blue) and HST/F502N (green) filters. The velocity is centered on the rest velocity of [O III] λ 5007 in the local gas in the LMC, which we assume has a systemic shift of $+273 \text{ km s}^{-1}$ compared to Earth (cf. Morse et al. 2006). The red wings of the curves ESO/[O III]/0 and HST/F502N are due to emission from [O III] λ 4959 that enters the filter with a shift of $\sim 2870 \text{ km s}^{-1}$. We have assumed that this line is a factor of three weaker than [O III] λ 5007.

The zero-velocity [O III] image of Fig. 2 reveals more extended emission in accordance with Caraveo et al. (1992). Faint patchy nebulosity from the LMC background is also seen. A comparison between the [O III]/0 image and the X-ray image obtained with Chandra/ACIS (right panel of Fig. 2), where the shell-like structure associated with the outer SNR shock activity is clearly detected (Hwang et al. 2001), shows no obvious morphology that connects the optical to the X-ray emission. As seen in Fig. 4, the slits used for our spectroscopic observations encapsulate X-ray structures of the SNR. This enables us to test (see Sect. 3.2) whether or not optical structures projected on the regions with strong X-ray emission and named “F1”, “F2”, “F4” and “F5” in Figs. 1 and 2 belong to, or are affected by the SNR.

The high spatial resolution of HST/WFPC2 allows us to resolve in great detail the filamentary structure of the SNRC. In Fig. 4 we present an image of this field obtained in the narrow band F673N, centered on [S II] λ 6716,6731. The F673N data, and data for the F502N band, centered on [O III] λ 5007, were shown and discussed by Morse et al. (2006) and Lundqvist et al. (2011).

Although detailed, the HST [S II] and [O III] narrow-band images may not fully reliably reveal the real structure and size of the SNRC. The reason is that the narrow band filters F502N and F673N may not fully cover the whole line profiles of the [O III] and [S II] emission, respectively. As shown in Morse et al. (2006), the F502N filter cuts around 5035 \AA , which corresponds to $\sim +1415 \text{ km s}^{-1}$ from the rest wavelength of [O III] λ 5007 (if we include a systemic shift of $+273 \text{ km s}^{-1}$ for the local gas in the LMC), but spectroscopic studies show (Kirshner et al. 1989, Sect. 3.2 of this paper) that the faint [O III] emission extends up to at least $+1700 \text{ km s}^{-1}$ (in the rest frame of LMC). This can, as pointed out by Morse et al. (2006), mean that F502N image misses out some high-velocity features of the SNRC (see also below).

The F673N filter cuts around 6770 \AA , which corresponds to $\sim +1475 \text{ km s}^{-1}$ from the rest wavelength of [S II] λ 6731 (for the same systemic redshift). Since the [S II] emitting region is truly more compact than that emitting [O III] also along the line

of sight (Sandin et al. 2013), the F673N filter (cf. Fig. 4) should encapsulate most of the [S II] emission.

Figure 4 demonstrates the difference between the HST/WFPC2/F673N (left) and NTT/EMMI/[O III]/0 (right) images. The images are presented for the same spatial scale and the contours of the Chandra/ACIS X-ray image are overlaid on each optical image to help us to better compare the sizes and shapes of the SNRC in both images. In the F673N image the emission from the SNRC in the optical traces the X-ray emission, and we see no [S II] emission outside the X-ray PWN (see also Lundqvist et al. 2011).

One effect not discussed in Morse et al. (2006) is the influence of the [O III] λ 4959 line on filter observations centered on [O III] λ 5007. Since the velocities of the remnant are high enough for the λ 4959 component to be probed by the F502N filter at velocities in the range $1900 - 4000 \text{ km s}^{-1}$ (including LMC redshift), and since the expected intensity ratio $I_{\lambda 5007}/I_{\lambda 4959}$ is 3, the effective F502N filter transmission of [O III] λ 4959, 5007 looks like the green curve in Fig. 3. From this we can clearly see that [O III] λ 4959, 5007 is not probed well by F502N for $v_{[\text{O III}]} \leq -1200 \text{ km s}^{-1}$ and at a redshift between $1300 - 1900 \text{ km s}^{-1}$, bottoming at around 5% effective transmission at $\sim +1600 \text{ km s}^{-1}$, while emission from gas at higher velocities has about 20% effective transmission. If we compare with the velocity maps of Sandin et al. (2013) for the VIMOS/IFU field, the F502N filter mainly misses emission from gas moving away from us at projected positions $\sim 2'' - 3''$ north-east and north-west of the pulsar, close to the pulsar and $\sim 3''$ southwest of the pulsar. This is shown in Fig. 6. As we discuss in Sect. 3.2, there are also regions outside the VIMOS/IFU field that are not probed well by the F502N filter.

The [O III]/0 filter used in our NTT/EMMI observations has its peak transmission at 5009 \AA and has 25% transmission of the peak value at 5042 \AA . Including the emission in [O III] λ 4959, Fig. 3 shows that 20% effective transmission extends out to $\sim +3500 \text{ km s}^{-1}$ (including LMC redshift), without any dropouts in transmission like those of the F502N filter. The 20% transmission cutoff on the blue side of [O III] λ 5007 is at $\sim -2200 \text{ km s}^{-1}$. The [O III]/0 filter is therefore likely to probe gas with all likely velocities, and with less bias than the F502N filter. Fig. 3 also shows that the effective transmission is the same (19%) for [O III]/0 and [O III]/6000 filters at $\sim 3600 \text{ km s}^{-1}$, and that the [O III]/6000 filter only kicks in at velocities $\gtrsim 3000 \text{ km s}^{-1}$, which is higher than seen in spectra for [O III].

A difference image between [O III]/0 and [O III]/6000 filter observations should therefore remove stars and the synchrotron continuum from the PWN, and in principle provide a cleaner image than using HST/F502N to probe [O III]-emitting gas moving at velocities between $\sim -2200 \text{ km s}^{-1}$ and $\sim +3000 \text{ km s}^{-1}$, albeit at lower spatial resolution. We show such an image in Fig. 5. The [O III]/0 image was smoothed to match the slightly worse seeing of the [O III]/6000 image before subtraction. However, some residuals from the image subtraction remain. The surface intensity has a square root scaling to bring out faint emission. To guide the eye, we have included a circle, which corresponds to the distance freely expanding SN ejecta would reach in 1100 years if moving at 2150 km s^{-1} (or in 1200 years if moving at 1980 km s^{-1}) and for a distance to the LMC of 50 kpc (e.g., Pietrzyński et al. 2019). Although the nebulous [O III] emission is complex, there is a hint of emission associated with the SNRC out to this radius. Fig. 5 also highlights filaments F1, F2, F4 and F5.

For the PWN part of the SNRC, the ground-based VIMOS/IFU [O III] images in Sandin et al. (2013), are superior to

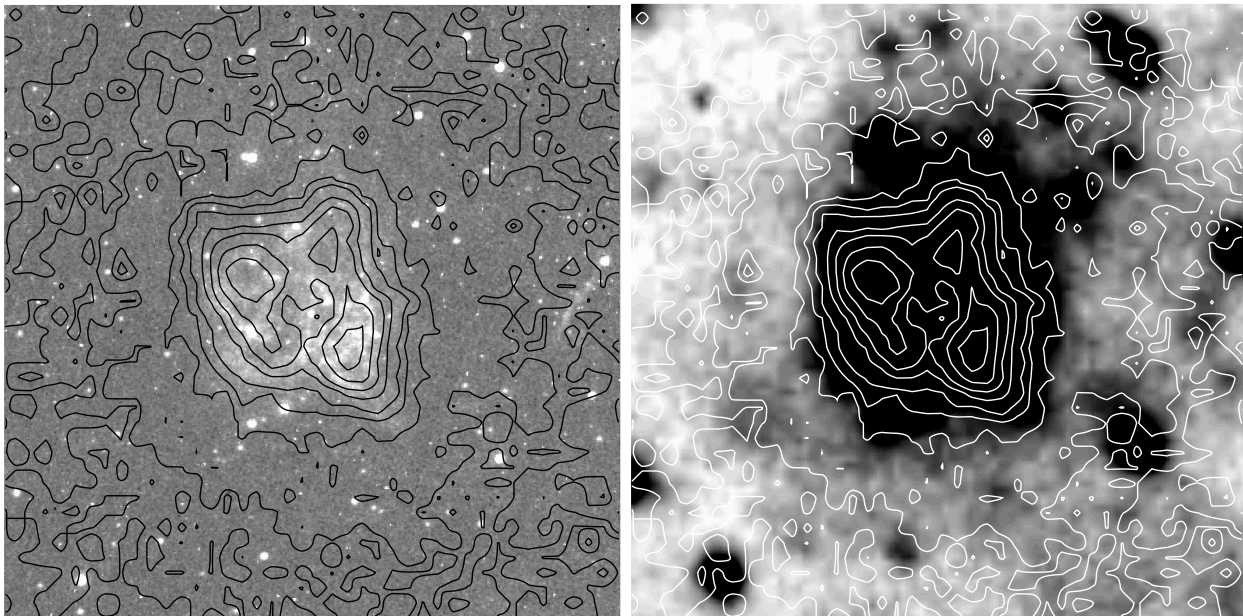


Fig. 4. Central $20'' \times 20''$ field of 0540 as viewed by HST/WFPC2/F673N (*left, positive*) and NTT/EMMI/[O III]/0 (*right, negative*). North is up and east to the left. The contours of the Chandra/ACIS X-ray fluxes in Fig. 2 are overlaid in both images. The spatial distribution of the X-ray emission shows an elongated structure with NW-SE jets, which is associated with the PWN (cf. Serafimovich et al. 2004; Lundqvist et al. 2011). As seen, the [S II] emission dominating in the HST image does not extend outside the PWN, whereas the [O III] glow in the NTT image extends far outside the PWN.

the combination of [O III]/0 and [O III]/6000 as it also adds velocity information, but those images only cover $13'' \times 13''$. A problem with all the mentioned methods to study the SNRC, even with the good spectral resolution of the VIMOS/IFU data, is to clean the images from [O III], and to a minor extent, He I $\lambda 5016$ (cf. Fig. 6) emission from H II regions in the LMC.

The [O III] emission in our NTT image extends outside the X-ray PWN, and the faint [O III] glow fills the space out to filament F1. This can certainly not be explained by worse spatial resolution of the ground-based observations, and further shows that we are losing some important information in the narrow band HST filters. Extended [O III] emission was discussed in Morse et al. (2006), and was traced out to a radius of $\sim 8''$. As filament F1 lies at a projected distance of $\approx 8''.5$ from the pulsar, the [O III] glow is therefore more extended than argued for by Morse et al. (2006, see also below). As shown in Fig. 5, there is in particular a broad region of [O III] glow to the southwest which extends well outside the ring with a radius of $10''$. We return to this below whether or not this glow is intrinsic to 0540, or emanates from other nebulae.

The [O III] glow in 0540 contrasts the situation for the Crab nebula, where the filamentary structure terminates with a shell-like structure. Observations of the filamentary ejecta in the Crab (e.g., Blair et al. 1997; Hester 1998) suggest that the filaments are the result of Rayleigh-Taylor instabilities at the interface between the synchrotron nebula and the swept-up ejecta. The emission comes from the cooling region behind the shock driven into the extended remnant by the pressure of the PWN. The same most likely applies to 0540 (cf. Williams et al. 2008, see also Section 3.4), but in the Crab there is no external glow (e.g. Tziampzis et al. 2009), presumably simply because of lack of fast SN ejecta (Yang & Chevalier 2015). Further comparing with the Crab, the protruded [O III] glow in the south-western direction in 0540, bears similarities with the Crab chimney (e.g., Rudie et al.

2008), especially when viewed through the HST/WFPC2/F502N filter (see Fig. 6).

3.2. Two-dimensional spectroscopy

As seen from Fig. 1, slits 1 and 2 cross the SNRC in two almost orthogonal directions. In both directions the angular sizes of the SNRC are about ten times larger than the $\sim 1''$ seeing value in our NTT and VLT spectral observations. This enables us to spectrally resolve different spatial parts of the SNRC projected on the slits, i.e., to create space-velocity maps of the encapsulated SN ejecta. In these space-velocity maps the continuum emission was subtracted using the IRAF background task along the spatial axis to reveal the kinematic structure from the emission lines. We caution that the uneven LMC background introduces some uncertainty in the derived velocity structure, especially for H α , at velocities embracing the LMC redshift, i.e., at $\sim 270 \pm 150 \text{ km s}^{-1}$. In Fig. 6, where we include results for [O III] from Sandin et al. (2013), we have used LMC redshift as the reference velocity, and will continue to do so as default throughout the paper, unless otherwise remarked.

The slit (“slit 2”) in Fig. 7 (top panel) is oriented almost along the continuum-emitting elongated structure of the central PWN, discussed in detail by Lundqvist et al. (2011). In Fig. 7 we have used a zoomed-in and rotated version of our NTT/EMMI [O III] difference image in the right panel of Fig. 6 for reference, as this image is free from continuum sources, to show how slit 2 probes 0540.

The second panel from the top in Fig. 7 shows the space-velocity distribution of the [O III] $\lambda 5007$ emitting material encapsulated by slit 2. The space-velocity structure of [O III] $\lambda 5007$ is unaffected by contamination from [O III] $\lambda 4959$ which is shifted in velocity to [O III] $\lambda 5007$ by $2\,870 \text{ km s}^{-1}$.

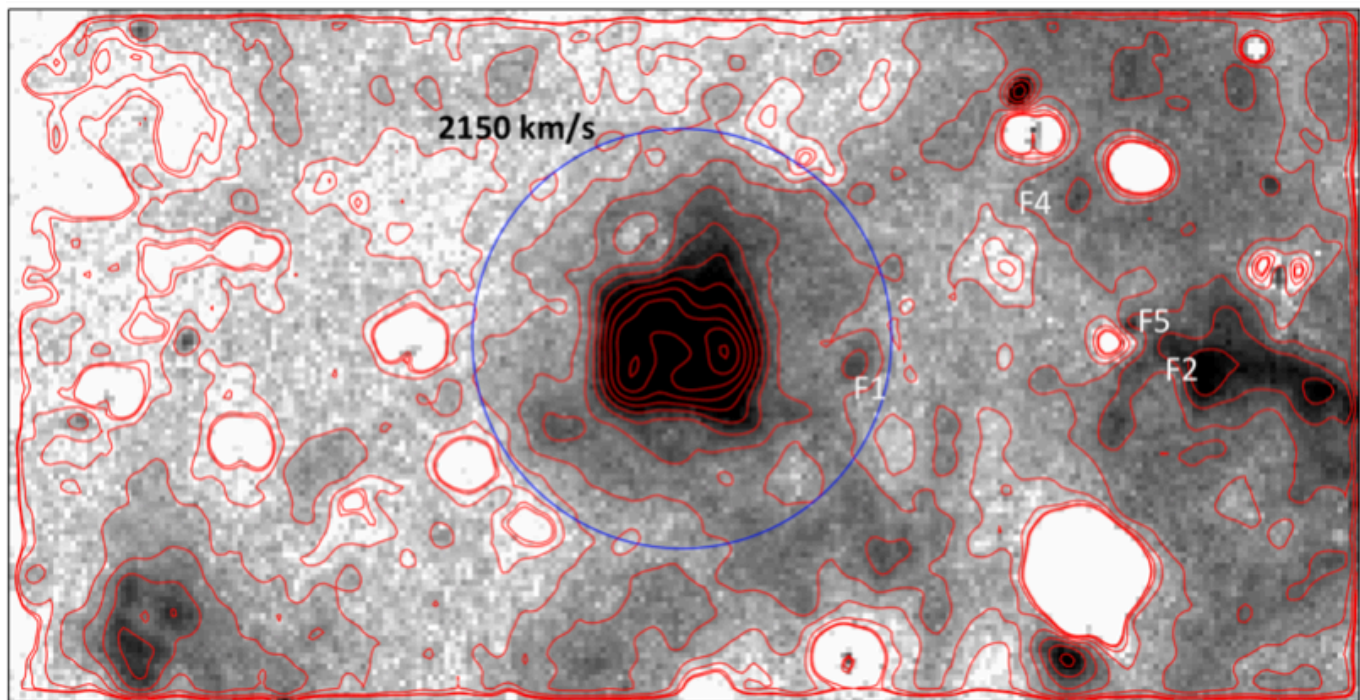


Fig. 5. *Right:* $65'' \times 33''$ difference image between NTT/EMMI/[O III]/0 and NTT/EMMI/[O III]/6000 with square root intensity scaling to bring out faint details. The [O III]/0 image was smoothed to match the slightly worse seeing of the [O III]/6000 image before subtraction. North is up and east is to the left. The image can trace faint [O III] emission to large distances from the pulsar. A blue circle is drawn with radius $10.0''$, corresponding to $\sim 2150 \text{ km s}^{-1}$ for ejecta coasting freely for 1100 years (or $\sim 1980 \text{ km s}^{-1}$ for 1200 years) at a distance of 50 kpc. The filaments F1, F2, F4 and F5, discussed in the text, are marked. Note PWN protrusions to the north, presumably in the pulsar jet direction, and to the southwest, which could be a structure similar to the Crab chimney.

The [O III] emission is dominated by a component with an average redshift velocity of $\sim 400 \text{ km s}^{-1}$ (relative to LMC redshift). There is a slight asymmetry with the northeast part being redshifted with a few hundred km s^{-1} more than the southwestern part. From the 3D structure of [O III] outlined by Sandin et al. (2013), the dominating centra of [O III] emission in our space-velocity map are parts of two separate dominating ring-like structures in the ejecta. They are clearly displayed in Fig. 6.

To highlight the fainter [O III] emission, we have constructed a similar plot to that in Fig. 7, but for wider velocity and spatial ranges. This is shown in Fig. 8 where we have again used our NTT/EMMI [O III] difference image, but this time a rotated version of that in Fig. 5 to highlight fainter emission. Fig. 8 also includes [O III] $\lambda 4959$, which is ≈ 3 times fainter than [O III] $\lambda 5007$, as expected. Both components of the doublet are shown to more easily evaluate high-velocity features, as well as the structure of the faint glow outside the SNRC. We have carefully subtracted stars, the PWN and LMC H II regions to trace the weakest features. Despite this, artifacts due to over-subtraction of the LMC background emission are seen, but are not crucial to conclusions about the space-velocity structure of the [O III] glow.

As seen, the faint glow has a completely different structure to that of the core, as its maximum redshift, close to $+2100 \text{ km s}^{-1}$, occurs in the southwestern part, whereas the maximum blueshift, $\sim -1300 \text{ km s}^{-1}$, is in northeastern part. The structures apparent for the two [O III] line components do not overlap, and have counterparts in both components that increase the reliability of the velocity structure. It is evident that the SNRC emission and the outer [O III] glow form two distinctly different ejecta components, which is fully consistent with the findings of Sandin et al. (2013) (see also Fig. 6), although the 3D cube of Sandin et al. (2013) did not include the highest velocities on the receding side.

We also note that the $+2100 \text{ km s}^{-1}$ component has a continuation from $\sim 3 - 4''$ southwest of the pulsar, and further along the slit in the same direction, all the way out to the edge of the frame at $9''$ from the pulsar, where the glow has a velocity just redward of LMC rest velocity, but perhaps also connects to emission on the blue side. It appears as if the glow is part of an incomplete shell structure with stronger emission on the receding side to the southwest and on the approaching side to the northeast. This is also consistent with the VIMOS/IFU image in Fig. 6. The glow continues further to the southwest, but the signal-to-noise is too low in the NTT/EMMI spectrum to trace the velocity outside the frame of Fig. 8. Signal-to-noise was also too low in the study of Mathewson et al. (1980) to probe possible broad-line emission in this direction (at PA = 60°).

Turning to [S II] $\lambda\lambda 6716, 6731$ in Fig. 7 we note that it has a smaller extent to the southwest than [O III], but similar extent to the northeast. Although not shown here, we see a similarly small extent in [Ar III] $\lambda 7136$. The two line components of [S II] blend together which makes the real space-velocity structure of each component more difficult to disentangle than for [O III]. In Sandin et al. (2013) we devised a way to separate the components, and at the same time create an electron density map from the relative intensities of the two [S II] line components, and we highlight this here in Sect. 3.2.2. The [S II] lines follow the trend for [O III] in Fig. 7, i.e., there is a general redshift towards the northeast compared to the southwest. The spectral structure range between a blueshift of $\sim 800 \text{ km s}^{-1}$ and a redshift of $\sim 1100 \text{ km s}^{-1}$.

The H α space-velocity structure (second panel from the bottom of Fig. 7) is less organized, mainly due to subtraction of the uneven LMC background in H α , but there is also a hint of subtraction residuals due to [N II] $\lambda\lambda 6548, 6583$. The bright emis-

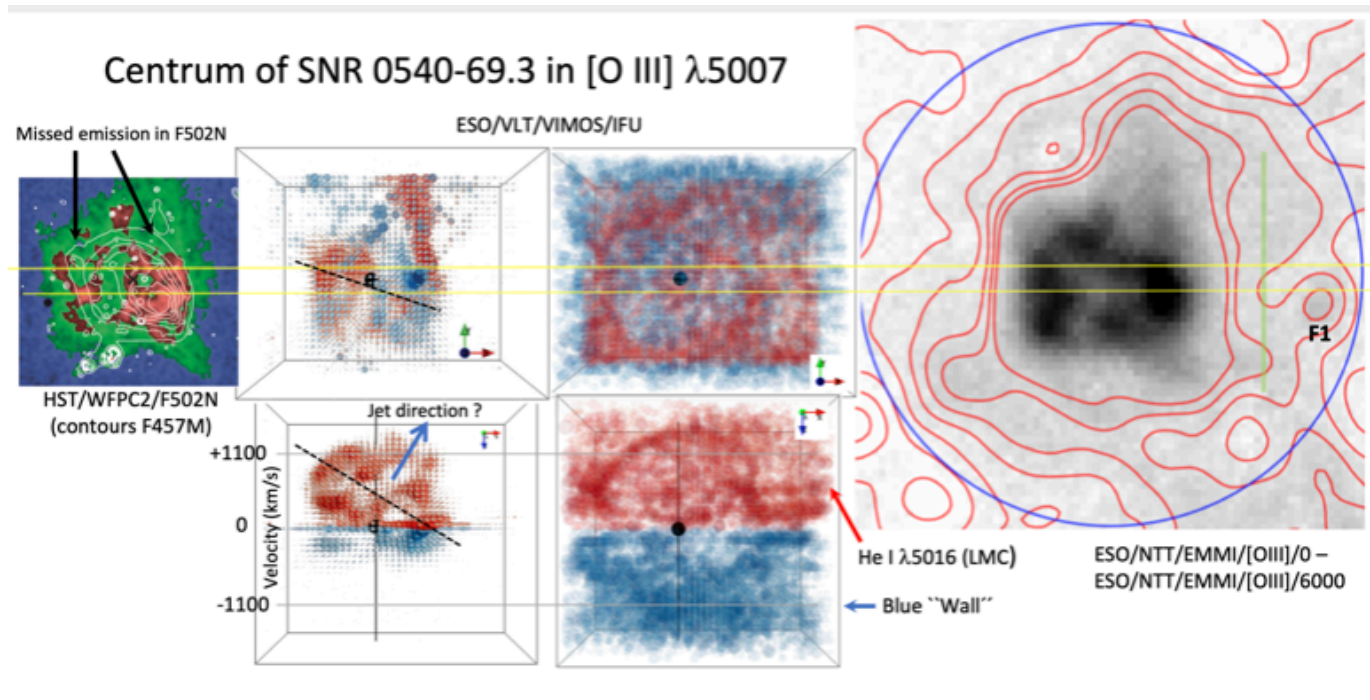


Fig. 6. *Right:* $20'' \times 20''$ difference image between the NTT/EMMI/[O III]/0 and NTT/EMMI/[O III]/6000 images. The blue circle has the same meaning as in Fig. 5. The flux scaling is linear. To highlight the [O III] glow, red contours are inserted for intensities up to 23% of the peak surface intensity of the PWN. Filament F1 has been marked. North is up and east to the left. *Middle two top panels:* [O III] $\lambda 5007$ as viewed by VIMOS/IFU Sandin et al. (2013). The left of the two middle panels shows the central part, where blue is for approaching ejecta, and red for receding. The right of the two panels brings out fainter halo emission. *Middle two bottom panels:* Same as the two top panels, but in velocity space. A symmetry axis (also shown in the top panel) is marked that goes through rings of [O III] emitting ejecta, and a possible jet axis is highlighted for the pulsar jet. For the lower right panel, likely contamination from LMC H II region He I $\lambda 5016$ is marked, as is also a region with emission on the approaching side (≤ -750 km s $^{-1}$) named the blue “Wall” (also seen for [O III] $\lambda 5007$ in Fig. 10). *Left:* Wavelet filtered HST/WFPC2/F502N map and contours of a wavelet filtered HST/WFPC2/F457M map (Lundqvist et al. 2011). Areas where the F502N fails to detect [O III] emission are highlighted. To guide the eye, a $1''$ slit with PA = 90° has been drawn across all top panels. A green line in the rightmost panel marks how far west the VIMOS field reaches. All images are to scale.

sion between $700 - 1200$ km s $^{-1}$ actually falls on top of the [N II] $\lambda 6583$ line from the LMC. H α or [N II] was a serious matter of discussion in Kirshner et al. (1989). To underline this, there is no strong [O III] or [S II] emission just north of the pulsar along the slit reaching out to $\sim +1900$ km s $^{-1}$, whereas the H α plot shows emission there. We agree with Morse et al. (2006) that [N II] $\lambda 6583$ from 0540 contributes at those wavelengths. That we expect H α from 0540 at all mainly rests on the results from slit 1 which clearly displays several Balmer lines (see below). This was reported for the first time in Serafimovich et al. (2005), and this has led to the interpretation that 0540 stems from a Type II SN explosion with a zero-age main-sequence mass of $\sim 20 M_\odot$ (Chevalier 2006; Williams et al. 2008; Lundqvist et al. 2011).

Moving to the space-velocity diagrams for slit 1, these are shown in the images in Fig. 9. We have again used a zoomed-in and rotated (this time by 2°) version of our NTT/EMMI [O III] difference image in the right panel of Fig. 6 for reference. The [O III] $\lambda 5007$ VLT/FORS image along slit 1 (Fig. 9) has a “pepper-slice”-like shape that also reflects the expansion of the SNRC. Like for slit 2, the emission is heavily redshifted, but less skewed in the space-velocity diagram. The line can be traced between about -700 km s $^{-1}$ and $+1400$ km s $^{-1}$. It is easy to imagine a relatively symmetric (but redshifted) shell with filamentary structures reaching inward toward the center around the average velocity of the shell, i.e., ~ 400 km s $^{-1}$. However, judging from the 3D structure derived by Sandin et al. (2013) and shown in

Fig. 6, the eastern and western parts of the “pepper” come from the same two ring-like features for the SNRC discussed for slit 2 above.

H β (panel two from the bottom of Fig. 9) is partly corrupted by the LMC background subtraction, but can be seen to have a surprisingly similar structure to that of [O II] $\lambda \lambda 3727, 3729$ (bottom panel of Fig. 9 in which the velocity scale is centered on 3727.5 \AA). Both H β and the [O II] lines lack emission at the highest velocities (≥ 1200 km s $^{-1}$) west of the pulsar. The different structures in [O II] and [O III] reveal different ionization conditions, especially in the western part along the slit. As a matter of fact, the [S II] 3D structure of Sandin et al. (2013) resembles those of H β and [O II] in Fig. 9, which may argue for that the differences between the [O III] and [S II] are more likely to be due to an effect of different levels of ionization rather than abundance effects. Moreover, the similarity between H β and [O II] further argues for contamination of [N II] in the H α image in Fig. 7.

Like the NTT data in Fig. 8, the VLT data in Fig. 10 show a glow of [O III] $\lambda 5007$ emission outside the inner part of the SNRC. The glow extends out to a radius of about $8'' - 10''$, and seems to connect to filament F1 in the west, which in turn appears to emit at a velocity close to LMC rest velocity. The blue circle in the upper panel marks a $10''$ radius from the pulsar. The space-velocity plot in Fig. 10 reveals four interesting features: fast blueshifted (at least to -1600 km s $^{-1}$) faint emission around the pulsar position, fast redshifted (at least to $+1800$ km s $^{-1}$) faint emission to the west of the pulsar, no redshifted emission

Table 2. Dereddened line fluxes relative to [O III] λ 5007 and line velocities in SNR 0540-69.3.

Line	VLT (PA=88°)			NTT (PA=22°)			Others ^d	
	Measured (Å)	flux ^a	velocity ^b (km s ⁻¹)	Measured (Å)	flux ^c	velocity ^b (km s ⁻¹)	flux	velocity ^b (km s ⁻¹)
[O II] $\lambda\lambda$ 3726,3729 ^e	3735.0	59.6	600 ± 90				52/61	732 ± 80
[Fe VII] λ 3759	3764.4	1.5	460 ± 30					
[Fe V] $\lambda\lambda$ 3783–3797	3797.8	1.7	690 ± 60					
[Ne III] λ 3869+H I, He I λ 3889 ^f	3878.2	3.3	710 ± 80				<2/7.3)	
[Ne III] λ 3967+H I λ 3970 ^f	3976.1	1.6	630 ± 120				-/1.7	
He I λ 4026	4034.0	0.4:	580 ± 90					
[S II] $\lambda\lambda$ 4069,4076 ^g	4078.1	3.5	700 ± 90				4/4.8	
H I λ 4102	4106.0	0.9:	310 ± 50					
He I λ 4143	4154.5	0.7:	780 ± 200					
[Fe V] λ 4227	4235.7	1.6	450 ± 170				6.7/-	
[Fe II] λ 4287	4295.3	0.9:	550 ± 180					
[O III] λ 4363+H γ	4368.7	5.7	380 ± 190				9.3/4.4	
[Fe II] λ 4414	4418.2	0.3:	250 ± 150					
[Fe II] $\lambda\lambda$ 4452,4458,4475 + He I λ 4471	4473.6	1.4	640 ± 250					
Mg I λ 4571	4576.8	0.4:	380 ± 90					
[Fe III] λ 4658	4665.5	1.9	480 ± 100	~4670	:: ⁱ		2:	
H β	4869.2	3.3	490 ± 70	~4870	:: ⁱ		<2/1.9	
[Fe III] λ 4881	4890.7	0.3:	590 ± 80					
[O III] λ 4959	4970.4	33.2	700 ± 120	4970.7	37	700 ± 50	33/33	515 ± 100
[Fe III] λ 4986	4987.6	1.4:	100 ± 300					
[O III] λ 5007	5017.9	100	660 ± 110	5016.3	100	560 ± 50	100/100	461 ± 120
[Fe II] λ 5044	5052.6	0.3:	540 ± 110					
[Fe II] λ 5159+[Fe VII] λ 5159	5171.0	1.6	700 ± 200	~5160	2:	100 ± 200		
[Fe III] λ 5270	5280.8	1.2	590 ± 120	~5280	2:	500 ± 200		
[Fe VII] λ 5721	5730.6	0.8:	520 ± 90					
He I λ 5876	5881.7	0.8:	310 ± 100				-/1.3	
[O I] λ 6300				6313.2	7	630 ± 20	6.7/4.4	
[O I] λ 6363				6374.3	4:	530 ± 70	-/1.2	
H α ^h				6577.8	17	680 ± 130	36/19.3	
[S II] $\lambda\lambda$ 6717,6731 ^g				6738.1	99	320 ± 50	67/45.1	
[Ar III] λ 7136				7151.0	9	630 ± 40	10.7/-	630 ± 100
[O II] λ 7325				7344.7	11	810 ± 120	8/-	
[Ni II] λ 7378				7390.5	9	520 ± 50	6.7/-	

^a The flux of [O III] λ 5007 is 4.1×10^{-14} ergs cm⁻² s⁻¹.

^c The flux of [O III] λ 5007 is 5.0×10^{-14} ergs cm⁻² s⁻¹.

^e [O II] λ 3727.5 was used for velocity estimate.

^g Velocity for [S II] λ 4069 and [S II] λ 6731, respectively.

ⁱ Line detected, flux uncertain.

^b Not corrected for the LMC redshift (~ 270 km s⁻¹).

^d Kirshner et al. (1989, PA=77°) / Morse et al. (2006, PA=124°).

^f Velocity estimated for [Ne III].

^h Blended with [N II] $\lambda\lambda$ 6548,6583.

at the pulsar position that was not already revealed by the bright emission in Fig. 9, and an intricate low-velocity structure which seems to form a loop to the east and a stream to the west possibly connecting to regions around filament F1. F1 itself stands out clearly, which could indicate that it is just an H II-region projected onto 0540. However, as we will see in Sect. 3.3.2, this is not the correct interpretation. In Section 3.3.2. we will also discuss [Fe III] λ 4986, which would introduce emission in Fig. 10 at ~ -1250 km s⁻¹. Contamination by He I λ 5016 would introduce emission at $\sim +530$ km s⁻¹, and could be responsible for the “horn” sticking out on the eastern side in the space-velocity plot, but a similar feature is seen for [O III] λ 4959, so background subtractions do not leave imprints from He I λ 5016 in Fig. 8, contrary to the VLT/VIMOS/IFU images of Sandin et al. (2013, cf. Fig. 6). We highlight that the VLT/VIMOS/IFU images neither cover F1 nor the low-velocity feature to the east.

The impression from slit 1 is the same as from slit 2, i.e. there appears to be glow from fast [O III]-emitting ejecta with a tilt to-

wards red on the western side and towards the blue on the eastern side. “Glow” (or at least fast [O III]-emitting ejecta) can be seen in the VIMOS/IFU image in Fig. 6 to be more pronounced for ejecta moving towards us than away from us, and this agrees with the fast blue-shifted ejecta in Fig. 10 with a projected center slightly to the east of the pulsar position.

The blue circle drawn in, e.g., Fig. 10 has a radius of 10'' and corresponds to a maximum velocity of freely coasting [O III]-emitting ejecta with velocity

$$v_{\max}([\text{O III}]) = 2150 \left(\frac{D_{\text{LMC}}}{50} \right) \left(\frac{t_{\text{yr}}}{1100} \right)^{-1} \text{ km s}^{-1}, \quad (1)$$

where D_{LMC} is the distance to 0540 in kpc and t_{yr} is the age of 0540 in years. As the space-velocity spectra do not really reveal [O III] at velocities $\gtrsim 2000$ km s⁻¹ (taking the spectral resolution into account), one may come to the conclusion that there is no support for space motions of [O III]-emitting gas much in excess of 2000 km s⁻¹ (relative to LMC). However, for both slits 1 and

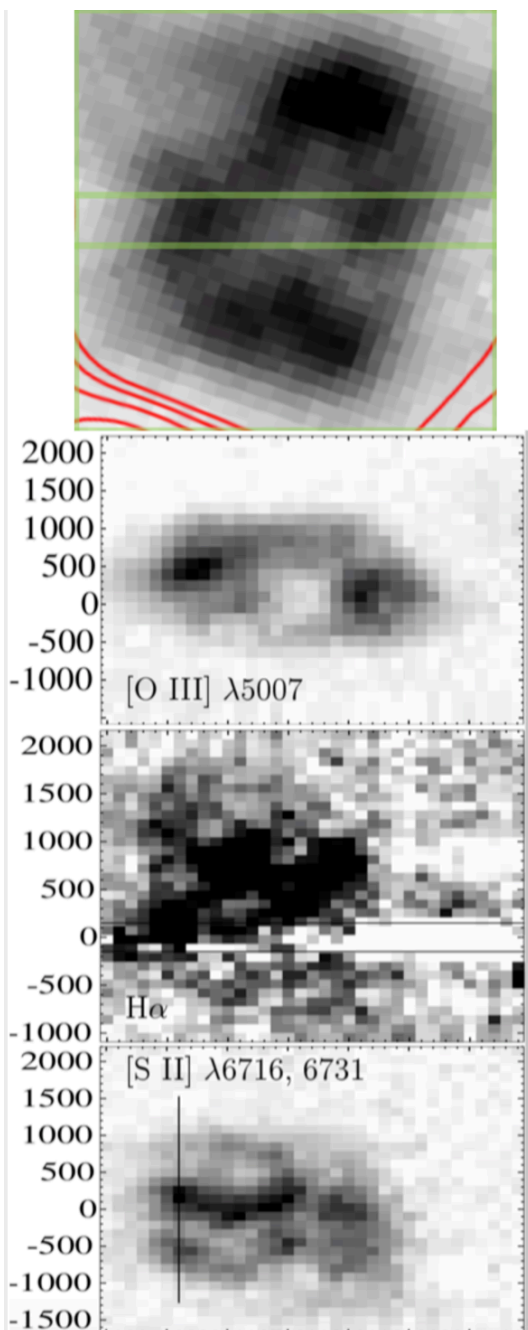


Fig. 7. *Top panel:* Central $8'' \times 8''$ of SNR 0540-69.3 using the NTT/EMMI difference image with linear intensity scaling in Fig. 6, rotated 68° to match the horizontally marked slit 2. *Lower panels:* Space-velocity images along slit 2 for [O III] $\lambda 5007$, $H\alpha$, and [S II] $\lambda\lambda 6716, 6731$. The vertical and horizontal axes show the velocity (in km s^{-1} , corrected for the LMC redshift) and the spatial coordinate (in arcseconds) along the slit, respectively. The horizontal black lines (for $H\alpha$) mark the velocity spread of H II regions in LMC ($\sim \pm 125 \text{ km s}^{-1}$). The velocity interval affected by the subtraction of the uneven LMC background is somewhat larger because of the finite spectral resolution. $H\alpha$ is more affected by the background subtraction than other lines, and blended with [N II] $\lambda\lambda 6548, 6583$. The vertical line in the [S II] image is described in Sect. 3.2.1.

2, the maximum velocity on the red side occurs $\sim 4''$ west and southwest of the pulsar, respectively. The true space motion of ballistic ejecta, v_{true} , if originating from a central position in the

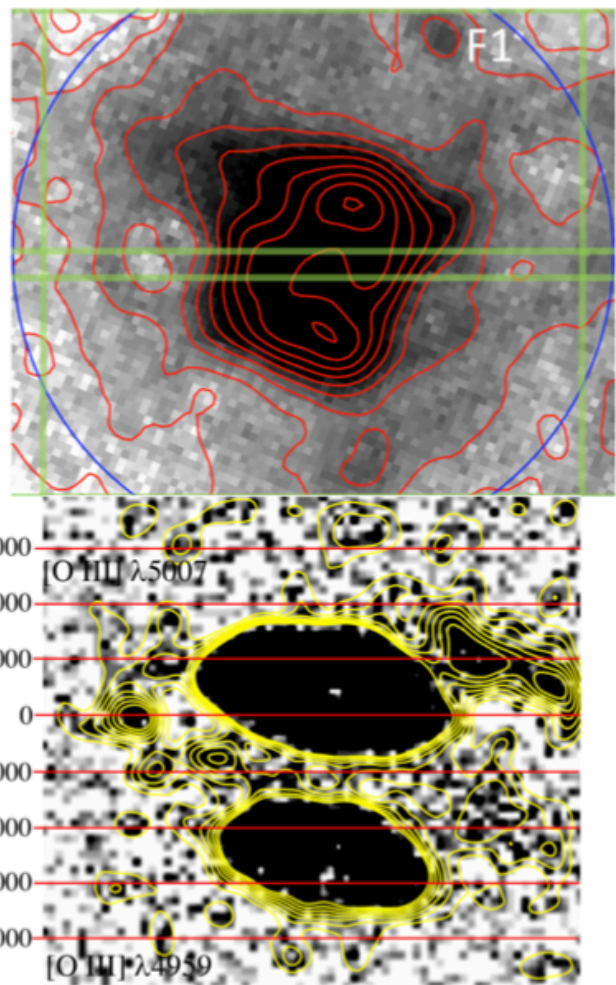


Fig. 8. *Top panel:* Central $20'' \times 17''$ of SNR 0540-69.3 using the NTT/EMMI difference image with square root intensity scaling in Fig. 5, rotated 68° to match the horizontally marked slit 2. *Bottom panel:* Space-velocity image along slit 2 for [O III] $\lambda\lambda 4959, 5007$. Velocity, corrected for the LMC redshift, is for [O III] $\lambda 5007$. The large dynamic range of the images reveals the faint glow emission outside the SNRC of 0540.

SNRC, is therefore

$$v_{\text{true}} = \sqrt{v_{\text{obs}}^2 + \left(\frac{r_{\text{obs}}}{t}\right)^2}, \quad (2)$$

where r_{obs} is the projected distance from the pulsar at which the maximum observed redshift velocity, v_{obs} , of [O III], emission occurs, and t is the age since explosion. With $D = 50 \text{ kpc}$ and $r_{\text{obs}} \approx 3.0 \times 10^{18} \text{ cm}$ (corresponding to $4''$), one obtains $v_{\text{true}}([\text{O III}]) \sim 2090$ (2060) km s^{-1} for $t_{\text{yr}} = 1100$ (1200) and $v_{\text{obs}} = 1900 \text{ km s}^{-1}$ for slit 1, and $v_{\text{true}}([\text{O III}]) \sim 2270$ (2240) km s^{-1} for $t_{\text{yr}} = 1100$ (1200) and $v_{\text{obs}} = 2100 \text{ km s}^{-1}$ for slit 2, respectively. This is several hundred km s^{-1} faster than $v_{\text{max}}([\text{O III}])$ for the SNRC on the red side, and also faster than the glow on the blue side, although confusion with [O III] $\lambda 4959$ causes uncertainty there.

To guide the eye, we have inserted two ellipses in Fig. 10. Both are for constant v_{true} in all azimuthal directions carved out by the slit, and they are both tuned to give $v_{\text{obs}} \pm 1900 \text{ km s}^{-1}$ at $4''$ west of the pulsar (as for slit 1). The blue and red curves

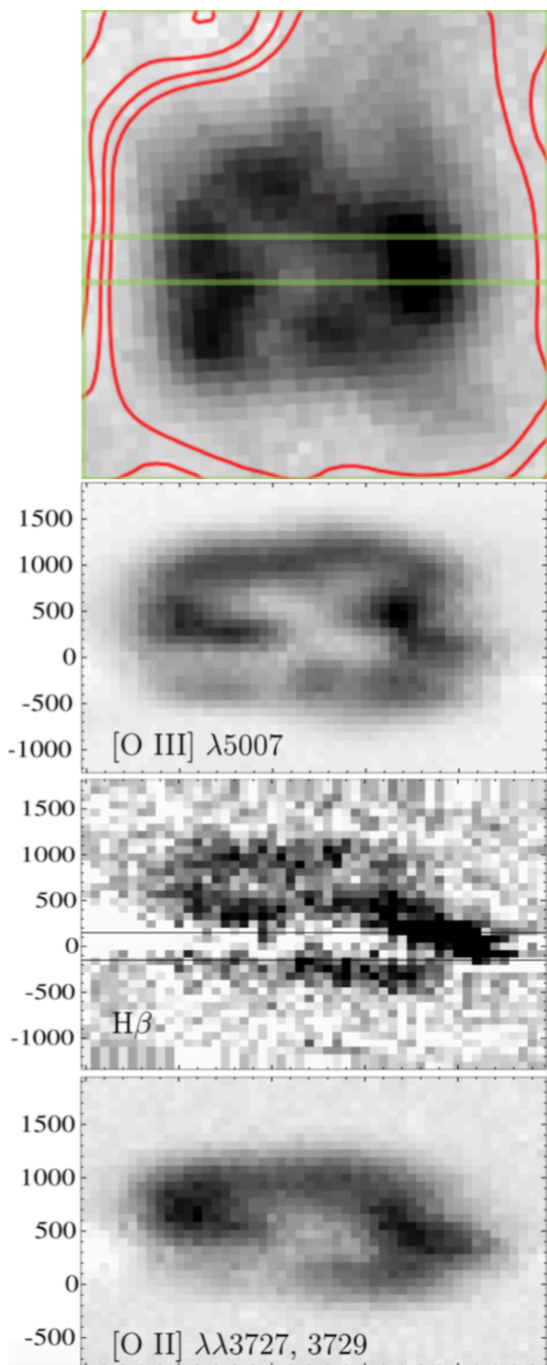


Fig. 9. Same as in Fig. 7, but for slit 1 (cf. Fig. 2), and for a different set of emission lines, as marked in the panels. The spatial extent of the images along the slit is $10''$. As for $H\alpha$ in Fig. 7, the $H\beta$ image is corrupted by subtraction of the uneven LMC background. Note the very different structures in [O II] and [O III].

are for $t_{\text{yr}} = 1100$ and $t_{\text{yr}} = 1200$, respectively, and $D_{\text{LMC}} = 50$. Both curves encapsulate F1, but reach zero velocity at $\pm 9''.7$ and $\pm 10''.4$, respectively. If v_{true} is indeed the same for the full region encapsulated by the slit west of the SNRC, Figs. 5 and 10 point to an age of $1100 \lesssim t_{\text{yr}} \lesssim 1200$. At the position of F1 (i.e., at $\sim 8''.5$), the red side of [O III] $\lambda 5007$ should reach 800 km s^{-1} for $t_{\text{yr}} = 1100$, and 1200 km s^{-1} for $t_{\text{yr}} = 1200$. For a non-accelerating scenario determining v_{true} (as in Eq. 2), the pulsar seems to be significantly younger than the spin-down age, i.e., ~ 1600 years. We return to the pulsar age in Section 3.4.3.

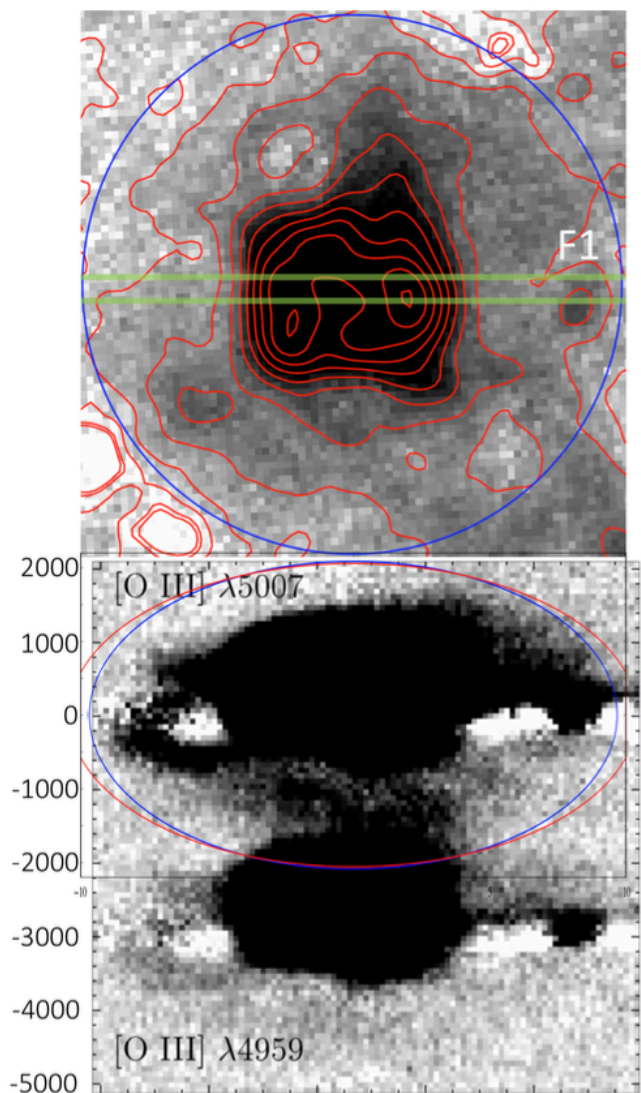


Fig. 10. Same as in Fig. 8, but for slit 1. The spatial extent of the images along the slit is $20''$. Filament F1 is highlighted. Ellipses are drawn around [O III] $\lambda 5007$ marking an ejecta velocity of $+1900 \text{ km s}^{-1}$ at $4''$ west of the pulsar, assuming freely coasting ejecta and an age of 1100 years (blue) and 1200 years (red) for 0540. See text for further details.

Looking at other parts of the space-velocity structure of the [O III] $\lambda 5007$ glow for slit 1, we note that v_{true} appears to be significantly lower than for the receding region west of the SNRC, perhaps except for the very eastern part, and towards the center of the SNRC on the blue side. The absence of [O III] $\lambda 5007$ at high velocities on the red side towards the SNRC is remarkable. This could be due real differences in the azimuthal distribution of [O III]-emitting gas, but it could in principle also be due dust absorption screening of the red side behind the SNRC. We find this explanation less likely though, since the dust would have to be located between the SNRC and fast (unseen due to dust) ejecta on the blue side, while there is no dust counterpart on the approaching side. Moreover, one does not see this effect in the Crab, despite it containing large amounts of dust (Gomez et al. 2012). In the Crab the dust is concentrated to filaments with modest filling factor which in the optical are notably strong in [O III].

The picture that emerges for the [O III] glow seen through slits 1 and 2 is that it does not come a spherically symmetric shell surrounding the SNRC, but from a much less complete structure.

On the blue side it appears to be concentrated to the “wall”-like structure centered just west of the pulsar position and reaching out to $\sim -1\,600\text{ km s}^{-1}$ seen and marked as “Blue Wall” in Fig. 6 and shown by Sandin et al. (2013). On the red side, the fastest glow is in the southwestern and western parts $\sim 4''$ from the pulsar reaching space velocities well in excess of $2\,000\text{ km s}^{-1}$. In the eastern part, velocities covered by slits 1 and 2 are less extreme, especially on the receding side. However, our slits do not cover the southeastern part. Here we make use of the long-slit observations by Morse et al. (2006) (described more in Section 3.3.1) as they cover the southeastern and northwestern parts of the [O III] glow region. Figure 5a of Morse et al. (2006) shows a clear asymmetry for the [O III] glow not covered by our slits 1 and 2, or the VIMOS/IFU data of Sandin et al. (2013). The figure of Morse et al. (2006) shows strong [O III] glow on the approaching side to the northwest, as well to the southeast for the receding side. Apart from the “wall”-like structure on the blue side (which is also evident as the blue-ward emission in the VIMOS/IFU spectrum in Fig 19), it appears as if the incomplete shell of [O III] glow is devoid of emission on the receding northern side, and on the approaching southern side.

3.2.1. Density from [S II] $\lambda\lambda 6716, 6731$

The two components of the [S II] doublet in Fig. 7 have a difference in wavelength corresponding to a velocity shift of $\approx 640\text{ km s}^{-1}$. In 0540 they blend together because of the velocity broadening of the emitting gas. There are, however, a few positions along the slit for which the blend is small. One such position is marked with a vertical solid line in Fig. 7, along detector row 29 in our notation. We discussed the deblending of [S II] $\lambda\lambda 6716, 6731$ along this row in Serafimovich et al. (2005), assuming that the line intensity ratio $R_{[\text{S II}]} = \frac{I(\lambda 6716)}{I(\lambda 6731)}$ is the same for all parts of the supernova remnant encapsulated by the slit row. As $R_{[\text{S II}]}$ is density sensitive (e.g., Osterbrock & Ferland 2006), we effectively assumed that the density is constant in this part of the remnant. The deblending in Serafimovich et al. (2005) resulted in $R_{[\text{S II}]} = 0.7$, and the multilevel model for [S II] described in Maran et al. (2000) was used to obtain $n_e = (1.4 - 4.3) \times 10^3\text{ cm}^{-3}$ for the temperature $T = 10^4\text{ K}$, and $n_e = (1.8 - 5.3) \times 10^3\text{ cm}^{-3}$ for $T = 2 \times 10^4\text{ K}$.

As we discuss in Sect. 3.4, the temperature in [S II]-emitting gas is probably $T \sim 15\,000\text{ K}$. In addition, a more careful background subtraction along row 29 than the preliminary one in Serafimovich et al. (2005) gives $R_{[\text{S II}]} = 0.85 \pm 0.10$, translating into $n_e = (0.9 - 2.0) \times 10^3\text{ cm}^{-3}$. This is fully consistent with densities found in the Crab Nebula for which [O II] and [S II] line ratios indicate electron densities in the range $4 \times 10^2 - 4 \times 10^3\text{ cm}^{-3}$ for the various filaments observed (Davidson & Fesen 1985). For the region mapped out by our detector row 29, Sandin et al. (2013) estimate $n_e \lesssim 1 \times 10^3\text{ cm}^{-3}$. As emphasized by these authors there are, however, pockets of ejecta with $n_e \sim (1 - 2) \times 10^3\text{ cm}^{-3}$ in the SNRC when spectra from individual fibers are studied; their density plot was smoothed over a 2×2 pixel kernel. Inspection of the individual fibre spectra of Sandin et al. (2013) also reveals background LMC residuals, which introduces a bias to underestimate electron densities from [S II]. The reason is the small field of view of VIMOS which makes background subtraction cumbersome. Our estimate of $n_e \sim (1 - 2) \times 10^3\text{ cm}^{-3}$ for detector row 29 are therefore not in conflict with Sandin et al. (2013). For a more complete discussion about the variation of electron density from [S II] within the SNRC we refer to Sandin et al. (2013), with the caveat in mind that the electron densities in that

paper could be somewhat underestimated in general. In addition, we emphasize that the densities derived for detector row 29 and in Sandin et al. (2013) are average densities along the line-of-sight for the SNRC, unlike the situation in the Crab for which more detailed 3D studies can be done more easily due its proximity (e.g., Charlebois et al. 2010; Martin et al. 2021). In the analysis in Sect. 3.4 for the SNRC we will use $n_e = 10^3\text{ cm}^{-3}$ unless otherwise specified.

3.3. One-dimensional spectroscopy

3.3.1. The central part of 0540

Previous optical spectroscopic studies of the SNRC were carried out by Mathewson et al. (1980), Kirshner et al. (1989) and Morse et al. (2006), and we reported preliminary results of our NTT/EMMI and VLT/FORS observations in Serafimovich et al. (2005). We will mainly compare with Kirshner et al. (1989) and Morse et al. (2006). Kirshner et al. (1989) used a slightly larger slit ($1''.5$) than us, and positioned their slit to cross the SNRC at PA = 77° . Morse et al. (2006) used an even wider slit ($2''$) at PA = 124° , and we discussed some of their results already in Sect. 3.2.

We extracted 1D spectra of the SNRC from our spectral images using the IRAF procedure `apall` and spatial extents of $10''$ and $8''$ centered on the pulsar for slits “1” and “2”, respectively. The extracted windows correspond to the observed extents of the SNRC along the respective slit directions. The extracted spectra are shown in Fig. 11 and 12.

Line fluxes were derived by integrating over each line profile. (No Gaussian fitting can be done since the line profiles are strongly non-Gaussian.) This gives accurate fluxes for strong lines like [O II] and [O III] as found from a test where we varied the background level up and down by 1σ from the mean value; the statistical error of the strongest lines is less than 5%. For faint lines like the [Fe II] lines and Mg I the flux uncertainty can be up to 40%. In Table 2 we have marked the fluxes of such lines by a colon.

A list of identified lines and their measured fluxes, central wavelengths and velocities is presented in Table 2. The results of Kirshner et al. (1989) and Morse et al. (2006) are also included for comparison. All our fluxes have been dereddened using $E(B - V) = 0.19$ and $R=3.1$, as was also done by Kirshner et al., while Morse et al. (2006) used $E(B - V) = 0.20$. A detailed discussion on the extinction towards 0540 can be found in Serafimovich et al. (2004). The fluxes were then normalized to [O III] $\lambda 5007$. We note that Kirshner et al. (1989) and Morse et al. (2006) normalized to the sum of [O III] $\lambda 4959$ and [O III] $\lambda 5007$. In Table 2 we therefore simply assumed a 1 : 3 line ratio of those two components, and renormalized all fluxes in Kirshner et al. (1989) and Morse et al. (2006) to [O III] $\lambda 5007$. Guided by the VIMOS/IFU observations of Sandin et al. (2013), who concentrated on the two doublets [O III] $\lambda\lambda 4959, 5007$ and [S II] $\lambda\lambda 6716, 6731$, one expects line fluxes for the various slit orientations shown in Table 2 to be different just because of different parts of the SNRC being caught by the slits.

Our 1D spectra of the SNRC are consistent with those of the other studies but also reveal many differences. The higher sensitivity of the VLT observations allowed us in Serafimovich et al. (2005) to report many new lines not detected in previous studies, and we report more here. The most important findings in Serafimovich et al. (2005) were [Ne III] $\lambda\lambda 3869, 3967$ and Balmer lines of hydrogen all the way down to H I $\lambda 3889$ (H ζ). While the neon lines constrain the supernova, the Balmer lines show that

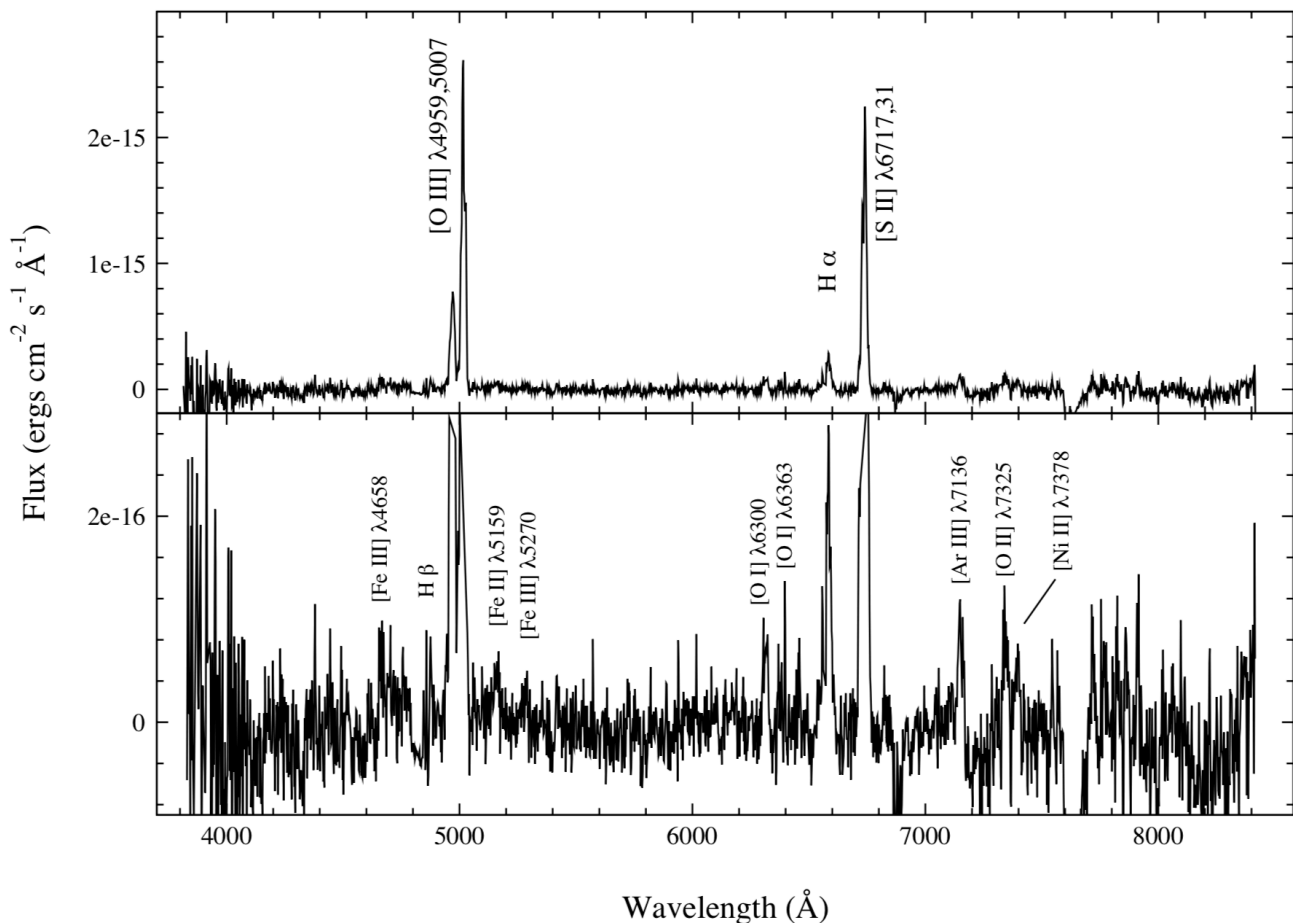


Fig. 11. Spectrum of the central part of the SNR 0540-69.3 obtained with ESO/NTT (PA=22°). The lower panel has an expanded flux scale to highlight weaker lines. The spectrum has been dereddened using $E(B - V) = 0.19$ and $R=3.1$. “H α ” is a blend of H α and [N II] $\lambda\lambda 6548, 6583$.

the previously detected emission around H α is at least partly due to H α , and not only to [N II] $\lambda 6583$, or any other line as discussed by Caraveo et al. (1998). We do not try to separate H α from [N II] $\lambda\lambda 6548, 6583$. However, from the H α panel of Fig. 7 it is clear that [N II] is present with a velocity structure that looks similar to that of [S II], and with a velocity for [N II] $\lambda 6583$ that reaches at least +1 000 km s $^{-1}$ in the LMC rest frame. Morse et al. (2006) estimated an intensity ratio of $I_{H\alpha}/I_{[N II]} \sim 1.1$ for their slit position.

The [Ne III] $\lambda\lambda 3869, 3967$ lines, and [O III] $\lambda 4363$ are all contaminated by H I lines, which leads to an overestimate of the fluxes of these lines not accounted for in Table 2, and for [O III] $\lambda 4363$ fluxes in previous investigations. Another complication is that all H I lines suffer from influence of the uneven LMC background which must be compensated for. We discuss this further Sect. 3.4.

Using unblended lines we estimate that the mean velocity of the central region of the 0540 system is $+500 \pm 55$ km s $^{-1}$ for slit “1” and $+380 \pm 60$ km s $^{-1}$ for slit “2”, respectively, when the LMC redshift of 270 km s $^{-1}$ is accounted for. Within errors both values are consistent with each other, and a mean velocity of the two gives $+440 \pm 80$ km s $^{-1}$. This is ~ 100 km s $^{-1}$ higher than the value of Kirshner et al. (1989), but the two investigations are consistent with each other, despite different slit orientations.

The redshift of the SNRC of 0540 is indeed large. An explanation could be that the 0540 system is the result of an asymmetric explosion, as discussed by Serafimovich et al. (2004). The

SNRC of 0540 is not unique in that sense. Balick & Heckman (1978) found that the oxygen-rich SNR NGC 4449 also moves at a velocity of ~ 500 km s $^{-1}$ relative to its surrounding H II regions. Like 0540, this remnant is also oxygen-rich. Over a larger scale, 0540 may not be all that asymmetric as revealed by the [O III] glow from ejecta moving at high speed ($\geq 1\,500$ km s $^{-1}$) both towards and away from us discussed in Sect. 3.2. (see also Morse et al. 2006; Sandin et al. 2013).

3.3.2. Filaments

SNR 0540-69.3 is near the LMC H II region DEM 269 and the OB association LH 104 (see Kirshner et al. 1989, and references therein, as well as below.) This is consistent with that we detect narrow emission lines that vary spatially in strength along our slits. The lines are spectrally unresolved (except for one case, see below).

To study whether or not some of these emitting regions are affected by the SNR activity, we looked at filaments detected along the slits. We mainly considered those with an [O III] temperature in clear excess of 10^4 K, as is usually observed in shocks or photoionization heated regions of known SNRs. We assumed the same extinction for the filaments as for the remnant, and used the standard ratio $R_{[O III]} = \frac{I(\lambda 4959) + I(\lambda 5007)}{I(\lambda 4363)}$ for the temperature (e.g., Osterbrock & Ferland 2006). We also looked for lines of highly ionized ions as tracers of influence by the SNR. We de-

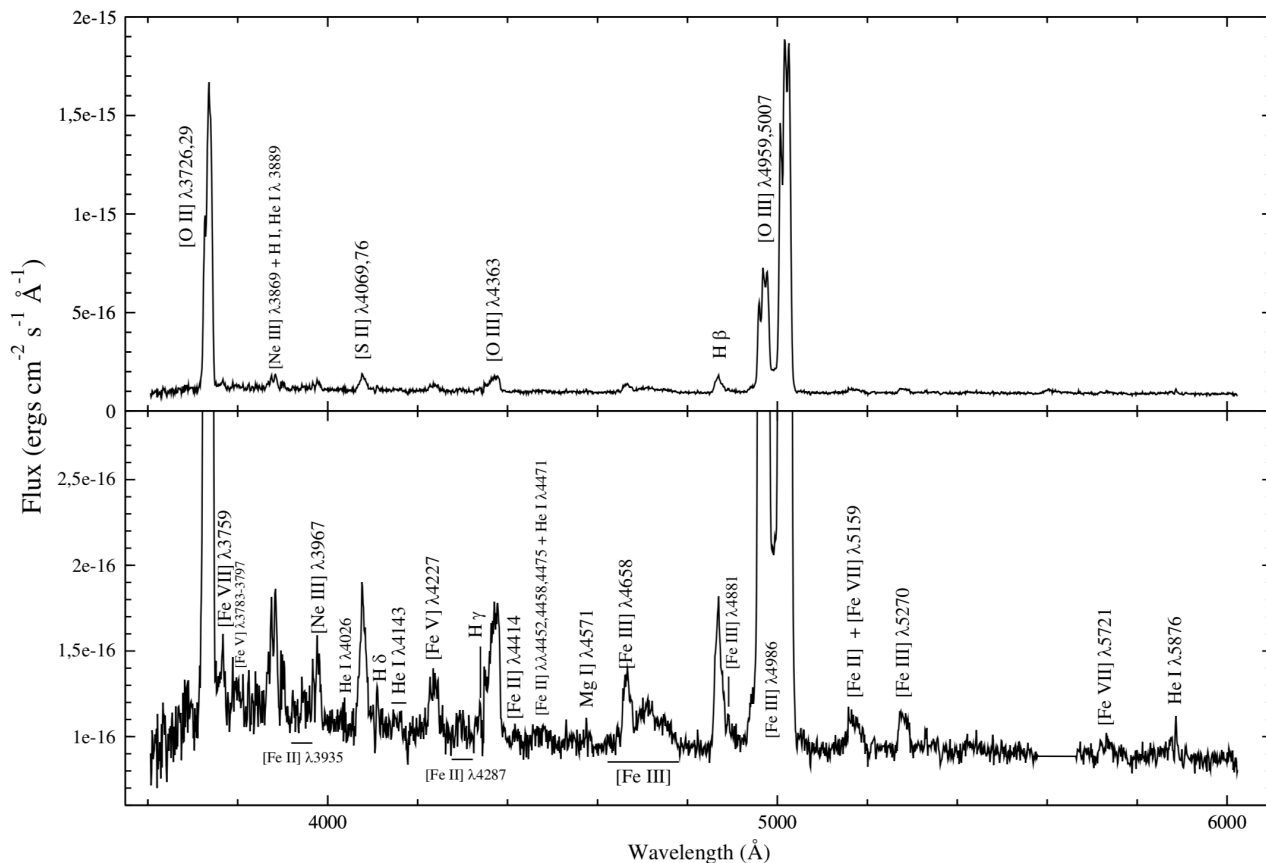


Fig. 12. Spectrum obtained with ESO/VLT (PA=88°), and again (like in the Fig. 11) the lower panel is plotted to bring out weaker lines. The spectrum has been dereddened using $E(B - V) = 0.19$ and $R=3.1$. Note the significantly higher signal-to-noise in the VLT spectrum compared to Fig. 11, which made it possible to detect new lines in SNR 0540-69.3 as reported in Serafimovich et al. (2005) and here. Of particular importance are the [Ne III] lines and H β (see text).

ected a few filaments of interest along the VLT slits “1” and “3”, and they are marked as F1, F2, F4 and F5 in Fig. 1. We also mark filament F3, and use this as reference for a presumed LMC H II region.

The typical size of the filaments along the slit is $\sim 3''$. As in the case of the SNRC we have constructed 1D spectra for each filament. The dereddened spectra of F1, which is closest to the SNRC in projection, and F5, which appears close to the outer shock front detected in X-rays, are shown in Figs. 13 and 14, respectively. Spectra of the other filaments are similar to the ones presented. Lists of identified spectral lines for F1-F5 with measured fluxes, central wavelengths and velocities, are presented in Tables 3 and 4. We return to a more detailed discussion of the filaments in Sect. 3.4.2.

3.4. Line profiles and intensities

3.4.1. The central part

Supernova remnants are good laboratories to test the theory of stellar evolution, explosive nucleosynthesis, radiation processes and shock physics. To test the first two items, an estimate of elemental abundances of the ejecta is essential. As the information from SNRs mainly rests on collisionally excited lines, we therefore also require knowledge about the density and temperature of the emitting gas.

The observed strength of the spectral lines allow us to deduce this information. The prime thermometer is $R_{[\text{O III}]}$. Because we see [O III] $\lambda\lambda 4959, 5007$ and [O III] $\lambda 4363$ in all VLT spectra of 0540 and the filaments, we are able to estimate the temperature of the [O III] emitting plasma in both the SN ejecta and the filaments.

Unfortunately, for the SNRC with its broad lines, [O III] $\lambda 4363$ is blended with H γ . This may lead to overestimating the [O III] temperature. To get the real [O III] temperature we subtracted H γ from the line profile of the observed [O III] $\lambda 4363$ +H γ blend. As a template profile for all H I lines we used H β . As shown in Fig. 15, the H β template is affected by [Fe III] $\lambda 4481$, but this has very small impact on the process of removing the bluer Balmer lines. A further complication is that all hydrogen lines suffer from background contamination of emission around LMC rest velocity. We approximated this for all H I lines by a linear approximation of the flux across the corrupted frequency range.

The expected flux of H γ relative to H β was estimated from Case B theory (Brocklehurst 1971). The bottom panel of Fig. 15 shows how we were able to remove H γ from the [O III] $\lambda 4363$ +H γ blend. As a spin-off, the line subtraction confirms the values we used for the dereddening, i.e., $E(B - V) = 0.19$ and $R = 3.1$; when the Balmer line was removed, continuum level was attained.

After the H γ subtraction, the flux of [O III] $\lambda 4363$ relative to [O III] $\lambda 5007$ (set to 100) is ~ 4.3 (instead of 5.7, if H γ

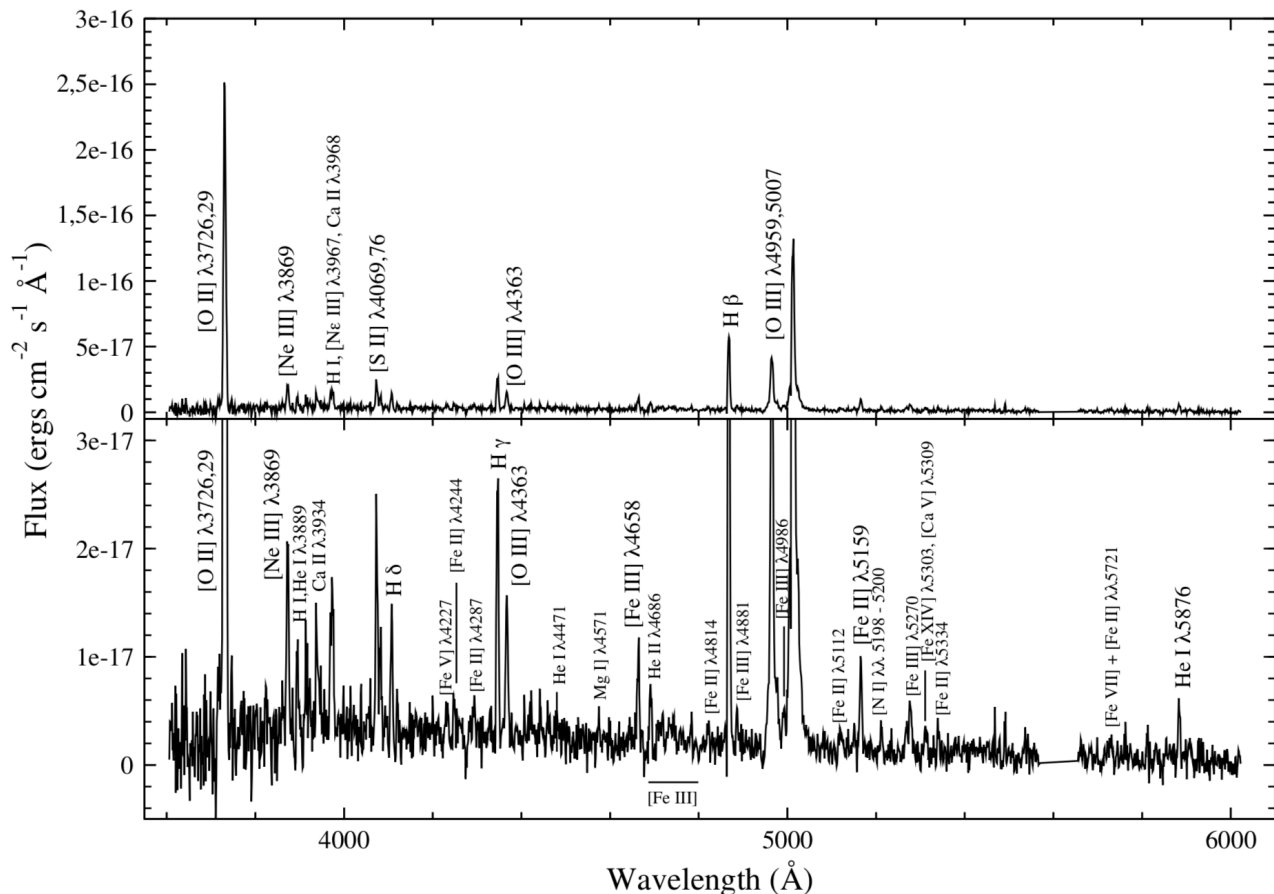


Fig. 13. Spectrum of filament F1 in the vicinity of SNR 0540-69.3. The filament is situated only 8'' west of the pulsar (see Figs. 1 and 2). As in Figs. 11 and 12, we have also plotted the spectra with expanded flux scales to highlight weaker lines. The spectrum was dereddened using $E(B - V) = 0.19$ and $R=3.1$. Note the broad base of the [O III] $\lambda\lambda 4959, 5007$ lines skewed to the red as compared to the narrow components, reaching at least +1700 km s⁻¹. No such features are seen in spectra of the emission from filaments F2, F3, F4 or F5 (see Fig. 14) as marked in Fig. 1. Line fluxes of all filaments are given in Tables 3 and 4.

is unaccounted for). This gives $R_{[\text{O III}]} \sim 31$. We can, however, refine this analysis by comparing the deblended profile of [O III] $\lambda 4363$ to that of a template profile for [O III] $\lambda\lambda 4959, 5007$. The template for the latter was made from a similar procedure to what was done in Sandin et al. (2013), i.e., the blue part of [O III] $\lambda 4959$ and the red part of [O III] $\lambda 5007$ were used as initial guesses for the template. With the known intensity ratio of 3 for $I(\lambda 5007)/I(\lambda 4959)$, we constructed the combined [O III] $\lambda\lambda 4959, 5007$ template shown in red in Fig. 16. The template is for the sum of the two line components. In the same figure we have also included the “clean” [O III] $\lambda 4363$ profile from Fig. 15. Once multiplied by a factor of 28, and once by 34. In general, the [O III] $\lambda 4363$ profile is similar to that of the [O III] $\lambda\lambda 4959, 5007$ template, although noise limits the usefulness of the [O III] $\lambda 4363$ profile in its wings.

We thus find $R_{[\text{O III}]} = 31 \pm 3$, with a tendency for a lower ratio in the blue part of the line profile compared to the red. The corresponding [O III] temperature range for the SNRC is $23\,500 \pm 1\,800$ K (cf. Table 5). This is less than $\sim 34\,000$ K, but consistent with $\approx 25\,500$ K estimated by Kirshner et al. (1989) and Morse et al. (2006), respectively. In neither of those two studies H γ was accounted for. The slightly larger ratio we find for $R_{[\text{O III}]}$ for the receding side of the remnant (compared to LMC rest velocity) could be due to a lower temperature in this part of the SNRC, or intrinsic dust reddening. The latter would not be

surprising considering that dust in the Crab nebula is concentrated to [O III]-emitting filaments, and the pathlength through dust to the receding side of the SNRC is likely to be longer than to ejecta moving toward us. To compensate for the factor ~ 1.2 in larger $R_{[\text{O III}]}$ -value for the red side, $E(B - V)$ would have to be ~ 0.5 instead of 0.19. This would depress the red side of the line profiles severely, which is not what we see. Dust is therefore not a likely reason for the large $R_{[\text{O III}]}$ -value on the red side of the [O III] lines.

Fig. 16 shows that the blue sides of [O III] $\lambda 4959$ and [O III] $\lambda 5007$ nearly reach $-1\,900$ km s⁻¹, which was difficult to disentangle from Fig. 10 due to blending. For the red side, the maximum velocity is +1700 km s⁻¹, which is consistent with the space-velocity results. Fig. 17 shows that the construction of the [O III] $\lambda\lambda 4959, 5007$ template reveals a residual that we attribute to [Fe III] $\lambda 4986$, a line that is also seen in the spectra of the filaments and other SNRs (Fesen & Hurford 1996).

The [Ne III] $\lambda\lambda 3869, 3967$ doublet is also affected by blending with Balmer lines. The same subtraction routine was applied for both components of [Ne III], and in Fig. 15 we show how the Balmer lines H ζ and H ϵ were removed from their blends with [Ne III] $\lambda 3869$ and [Ne III] $\lambda 3968$, respectively. As seen from the figure, [Ne III] $\lambda 3869$ is insignificantly contaminated by Balmer line emission, whereas [Ne III] $\lambda 3967$ is more affected.

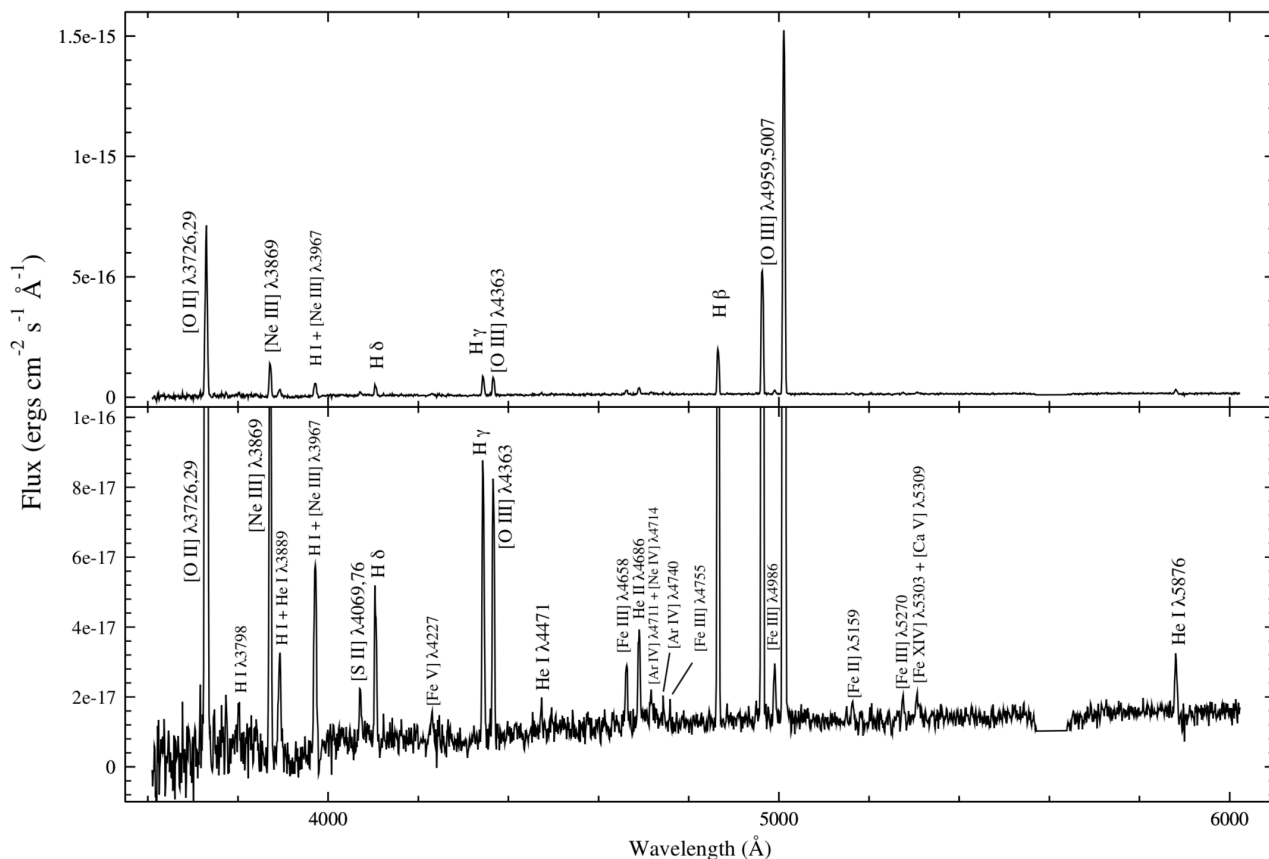


Fig. 14. Spectrum of an H II region along the VLT slit “3” at a projected distance of 25” to the west of the pulsar (called filament F5 in Figs. 1 and 2). As in Fig. 11, we have also plotted spectra with expanded flux scales to highlight weaker lines. The spectrum have been dereddened using $E(B - V) = 0.19$ and $R=3.1$.

A direct comparison between [Ne III] $\lambda 3869$ and [O III] $\lambda 5007$ is shown in Fig. 18. The profile of the neon line is fairly noisy, but it is consistent with the general features and maximum velocities of [O III] $\lambda 5007$. The ratio of the two lines is $I_{[\text{O III}] \lambda 5007} / I_{[\text{Ne III}] \lambda 3869} \sim 30$. With a temperature in the $23\,500 \pm 1\,800$ K, and assuming similar ionization structures of O^{2+} and Ne^{2+} , our multilevel atom models (e.g., Maran et al. 2000; Mattila et al. 2010), updated with the recent atomic data in the CHIANTI database (Del Zanna et al. 2021), result in a mass ratio $M_{\text{Ne}}/M_{\text{O}} \sim 0.07$, which should probably be considered a lower limit since the ionization zone of O^{2+} is likely to be wider than that of Ne^{2+} . In this context, we highlight the observations of Morse et al. (2006). They detected [Ne III] $\lambda 3869$, but neither got a 3σ detection of [Ne III] $\lambda 3967$, nor corrected for Balmer line contamination. Their flux values translate into $M_{\text{Ne}}/M_{\text{O}} \sim 0.13$ for the temperature we find from [O III].

Williams et al. (2008) modeled the emission from 0540, and in those models they assumed the abundance ratio $\text{Ne}/\text{O} = 0.2$ (i.e., a mass ratio of 0.25), and obtained $I_{[\text{Ne III}] \lambda 3869} / I_{[\text{O III}] \lambda 5007} = 0.093$. This is almost three times the value we obtain from our observations; if the $M_{\text{Ne}}/M_{\text{O}}$ ratio in their model is lowered to 0.085 (i.e., close to our value of 0.07), their predicted line ratio should agree with our observations. The question is how likely a value of $M_{\text{Ne}}/M_{\text{O}} \sim 0.1$ could be. It is, for example, about half the mass ratio for the inner ejecta found in a recent model for the nucleosynthesis yields for the central part of an exploding $11.8 M_{\odot}$ star (Sieverding et al. 2020), but the models of Chieffi & Limongi (2013), which take rotation of the progenitor into ac-

count, yield $M_{\text{Ne}}/M_{\text{O}} = 0.063$ (0.053) (0.21) M_{\odot} for progenitor masses of 13 (15) (20) M_{\odot} . For non-rotating progenitors Chieffi & Limongi (2013) find $M_{\text{Ne}}/M_{\text{O}} = 0.22$ (0.46) (0.32) M_{\odot} . Judging from this, rotation could be important as $M_{\text{Ne}}/M_{\text{O}}$ in those models agree with the values derived from observations.

In the models of Williams et al. (2008), infrared lines observed with *Spitzer Space Telescope* were included. To compare the IR lines to optical lines, these authors multiplied the fluxes in Morse et al. (2006) by a factor of 4 to account for the 2” slit in the optical as the infrared observations observed the full region. We use the same procedure, but to put the slit compensation on firmer footing, we make use of the VLT/VIMOS observations of Sandin et al. (2013). In Fig. 19 we show the line profile of [O III] $\lambda 5007$ for the full $13'' \times 13''$ field observed with VIMOS, and compare this to 7.2 \times the template [O III] $\lambda 5007$ profile from our slit 1 observations. With the 7.2 factor, the integrated emission of the two profiles is the same for velocities $\gtrsim -750$ km s $^{-1}$. About 10% of the VIMOS [O III] $\lambda 5007$ flux falls at velocities below -750 km s $^{-1}$, and is mainly attributed to [O III] glow not captured efficiently by the slits used by Morse et al. (2006) and us. We therefore use the factor of 7.2 for most lines. For lines with suspected glow we use 8.0 since the *Spitzer* field-of-view is likely to capture much of the glow. (The corresponding numbers for our NTT/EMMI slit, i.e., slit 2, is 6.3 and 6.6, respectively.) As Morse et al. (2006) obtain ≈ 1.6 times larger [O III] $\lambda 5007$ flux through their $2'' \times 11''$ slit than we do through our $1'' \times 10''$ slit, the conversion factor Williams et al. (2008) should have used for most lines is 4.5, instead of their 4. For [O III] $\lambda 5007$, and

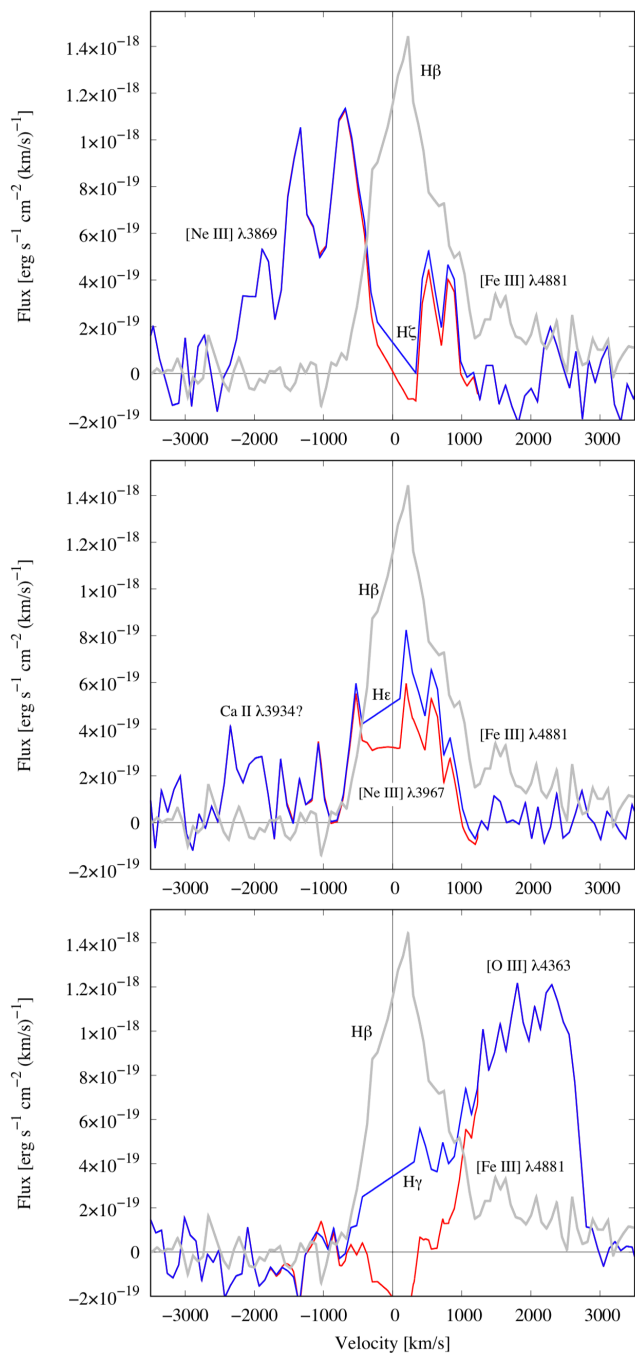


Fig. 15. Line profiles of the Balmer lines from 0540 in velocity space relative to LMC for the VLT spectrum in Fig. 12. *Top panel:* $H\zeta$ blended with $[\text{Ne III}] \lambda 3869$, *Middle panel:* $H\epsilon$ blended with $[\text{Ne III}] \lambda 3967$, and *bottom panel:* $H\gamma$ blended with $[\text{O III}] \lambda 4363$. In all panels we also show $H\beta$ (grey) and the continuum level (black). $H\beta$ was used as a template to subtract the expected emission from $H\gamma$, $H\epsilon$ and $H\zeta$ using Case B line ratios (Brocklehurst 1971). The blue and red solid lines show $[\text{O III}] \lambda 4363$ and $[\text{Ne III}] \lambda 3869, 3967$ before and after deblending, respectively.

other possible lines with glow, a conversion factor of 5 would have been more appropriate.

Williams et al. (2008) measure $(7.29 \pm 0.56) \times 10^{-14} \text{ erg cm}^{-2} \text{ s}^{-1}$ for $[\text{Ne III}] 15.6\mu$. If we use our VLT observations, multiplied by 8, the $[\text{Ne III}] \lambda 3869$ flux is $1.1 \times 10^{-14} \text{ erg cm}^{-2} \text{ s}^{-1}$, i.e., $I_{[\text{Ne III}] 15.6\mu} / I_{[\text{Ne III}] \lambda 3869} \sim 6.7$,

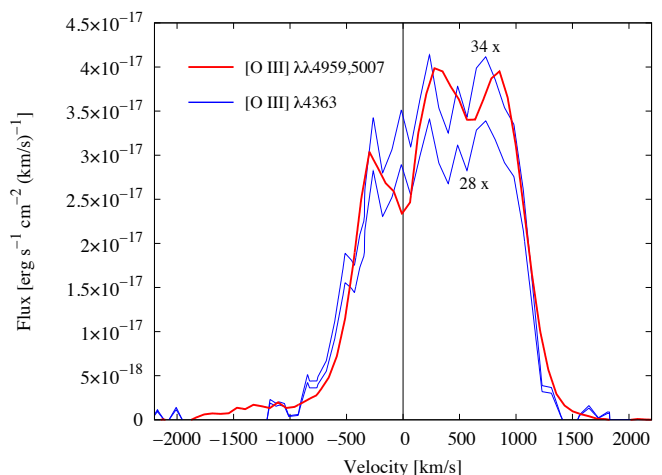


Fig. 16. Line profiles of $[\text{O III}] \lambda 4959, 5007$ and $[\text{O III}] \lambda 4363$ of the emission from 0540 as observed through the VLT slit. The velocity is relative to LMC. The $[\text{O III}] \lambda 4959, 5007$ profile was created from a cleaning procedure described in the text, and is for the sum of the two line components. The $[\text{O III}] \lambda 4363$ is the blue-red profile in the bottom panel of Fig. 15. The flux of $[\text{O III}] \lambda 4363$ has been multiplied by 28 and 34 to match the various parts of the line profiles. There is a tendency of relatively weaker $[\text{O III}] \lambda 4363$ on the blue side, which could mean hotter $[\text{O III}]$ -emitting plasma on the receding side of 0540 (see text).

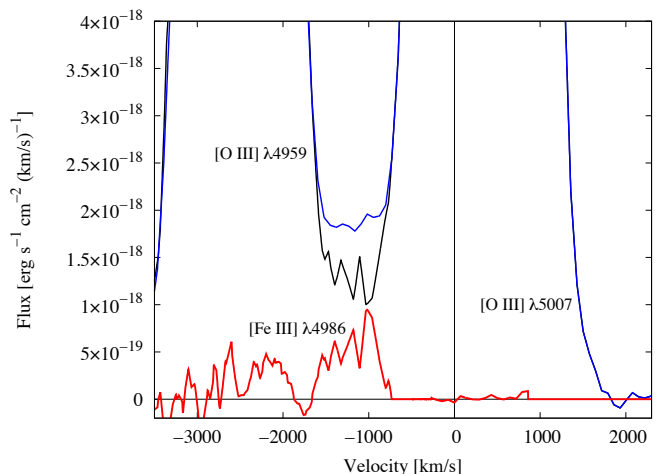


Fig. 17. Sum of the “cleaned” $[\text{O III}] \lambda 4959, 5007$ profiles (cf. Fig. 16) of the emission from 0540 (black) compared to the observed emission (blue). The velocity scale is for the $\lambda 5007$ component relative to LMC. The difference (red) is attributed to $[\text{Fe III}] \lambda 4986$. The maximum velocity on the red side of $[\text{O III}] \lambda 5007$ is $\approx +1800 \text{ km s}^{-1}$, which may be less than on the blue side ($\approx -1900 \text{ km s}^{-1}$, see Fig. 16).

which is twice as high as in the model of Williams et al. (2008). From our multilevel modeling it is obvious that the $[\text{Ne III}] 15.6\mu$ flux cannot come from the same hot gas as the $[\text{O III}]$ lines we observe, since the ratio for this at 23 000 K is $I_{[\text{Ne III}] 15.6\mu} / I_{[\text{Ne III}] \lambda 3869} \sim 0.14$. An intensity ratio of 6.7 is only obtained for temperatures $\lesssim 7000 \text{ K}$. Although there are several uncertainties, the main explanation must be that $[\text{Ne III}] 15.6\mu$ predominantly comes from regions with much lower temperatures than that emitting the optical $[\text{O III}]$ and $[\text{Ne III}]$ lines. The most likely region is gas heated by photonization rather than by shocks, as shock-heated material would be hotter. Extinction

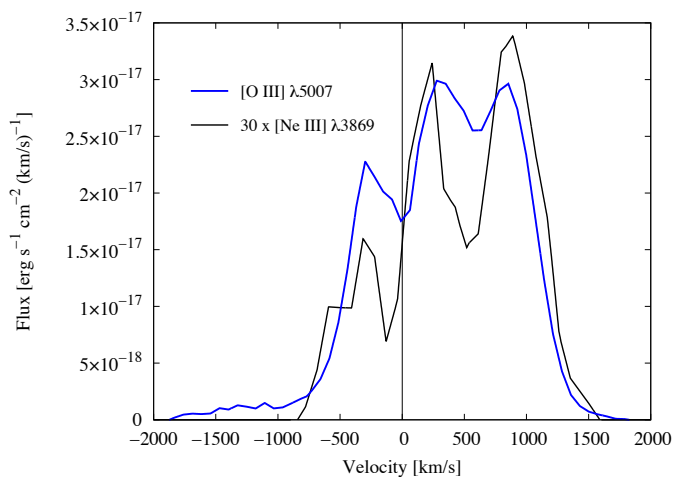


Fig. 18. Same profile for [O III] as in Fig. 16, but only for [O III] $\lambda 5007$ (blue) together with the “cleaned” [Ne III] $\lambda 3869$ profile in Fig. 15. The [Ne III] profile was multiplied by a factor of 30 to match [O III] $\lambda 5007$. Note the similar widths and structures of the two profiles. Noise is too high for the [Ne III] line to trace it out the highest velocities on the blue side.

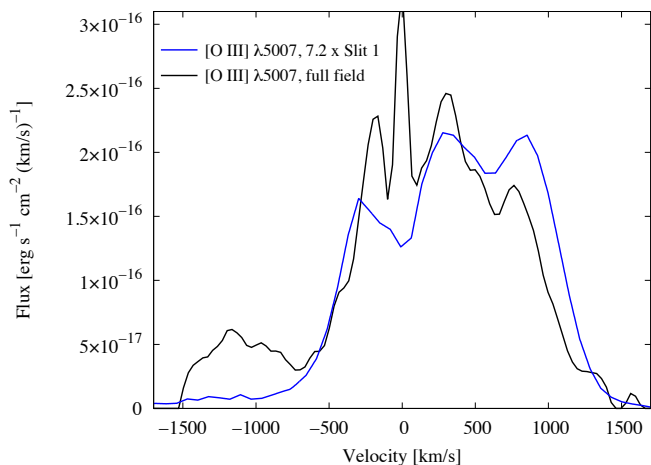


Fig. 19. Same profile for [O III] $\lambda\lambda 4959,5007$ as in Fig. 16 (blue) together with the [O III] $\lambda\lambda 4959,5007$ profile for the full $13'' \times 13''$ field as observed by Sandin et al. (2013). The slit 1 profile was multiplied by a factor of 7.2 to match the integrated emission at ≥ -750 km s $^{-1}$. Note the strong [O III] emission for ≤ -750 km s $^{-1}$ for the larger field-of-view compared to the slit 1 observations. This emission corresponds to about 10% of the total [O III] emission. A minor fraction ($\sim 10\%$) of the emission at ≤ -750 km s $^{-1}$ could be due to [Fe III] $\lambda 4986$, as displayed in Fig. 17, but most of it comes from the approaching “wall” described in Sect. 3.2.

due to internal dust may be a complementary explanation as this would not affect the IR line.

Fig. 19 emphasizes the redshift of all [O III] emission from the full SNRC, and shows that the line profile through slit 1 surprisingly well represents the emission at most velocities. The most obvious difference is the strong emission at velocities $\gtrsim -750$ km s $^{-1}$ (which is also evident from Fig. 6, and which is mainly due to the approaching “wall” described in Sect. 3.2) as well as slightly more emission at $\gtrsim +750$ km s $^{-1}$. The peak around LMC rest velocity is at least to some extent artificial due to difficulty with removing LMC background emission due to the

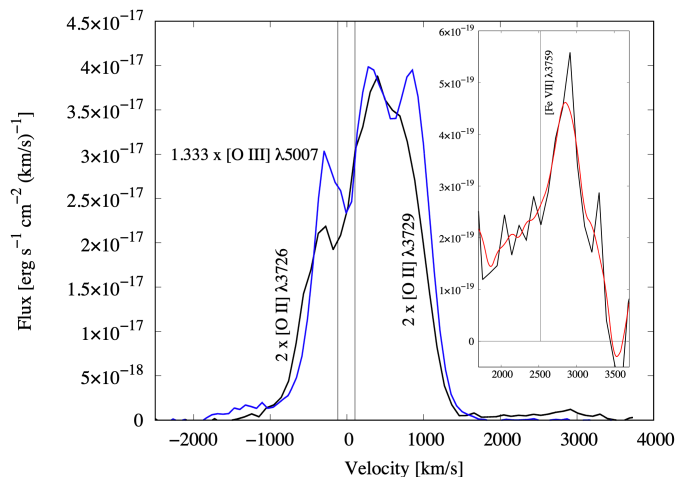


Fig. 20. Same profile for [O II] $\lambda\lambda 4959,5007$ as in Fig. 16 (blue) together with the combined [O II] $\lambda\lambda 3726,3729$ profile. The velocity for the [O II] lines is centered on 3727.5 Å. The [O II] profile was multiplied by a factor of 2 to match $1.33 \times$ [O III] $\lambda 5007$. Note that [O II] $\lambda 3726$ only reaches ≈ -1400 km s $^{-1}$ on the blue side (when the 118 km s $^{-1}$ difference between [O II] $\lambda 3726$ and 3727.5 Å is accounted for). On the red side of [O II] $\lambda 3729$ the emission is blended with [Fe VII] $\lambda 3759$ as shown by the inset. The red curve is Savitzky-Golay fitting to the noisy [Fe VII] line profile.

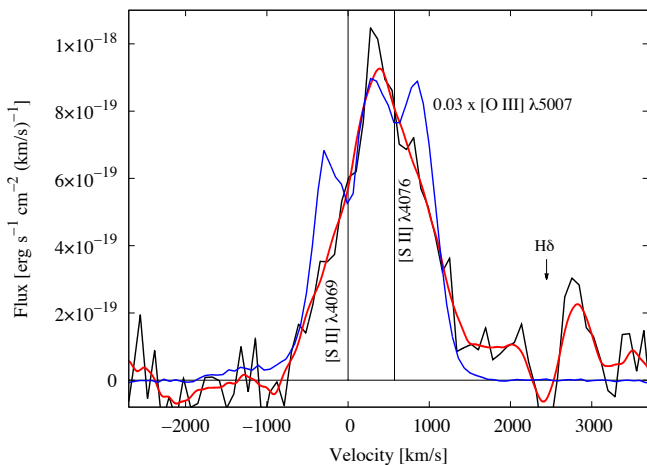


Fig. 21. Same in Fig. 18, but for [S II] $\lambda\lambda 4069,4076$ (black, and smoothed in red) instead of [Ne III] $\lambda 3869$. The [O III] profile was multiplied by a factor of 0.03 to match [S II]. The sulphur doublet was velocity-centered on the $\lambda 4069$ component. LMC rest frame velocities for both components are marked by vertical thin lines. The red side of the [S II] doublet is affected by H δ . (The dip in H δ is due to over-subtraction of the LMC background.)

small field-of-view of VIMOS. The VIMOS data are not sensitive enough to trace velocities $\gtrsim |\pm 1500|$ km s $^{-1}$.

Turning to ions of lower degree of ionization observed through slit 1, we show [O II] $\lambda\lambda 3726,3729$ in Fig. 20, [S II] $\lambda\lambda 4069,4076$ in Fig. 21, and He I $\lambda 5876$ in Fig. 22. For [O II] and [S II] we have centered the velocity on 3727.5 Å and the strongest component of [S II] (i.e., $\lambda 4069$), respectively. As already discussed in Sect. 3.2, [O II] has a profile similar to that of H β , and [S II] $\lambda\lambda 4069,4076$ is similarly narrow, i.e., primarily extends from ~ -700 km s $^{-1}$ to $\sim +1000$ km s $^{-1}$, although there is a blue wing of [O II] that reaches ~ -1400 km s $^{-1}$. This is not

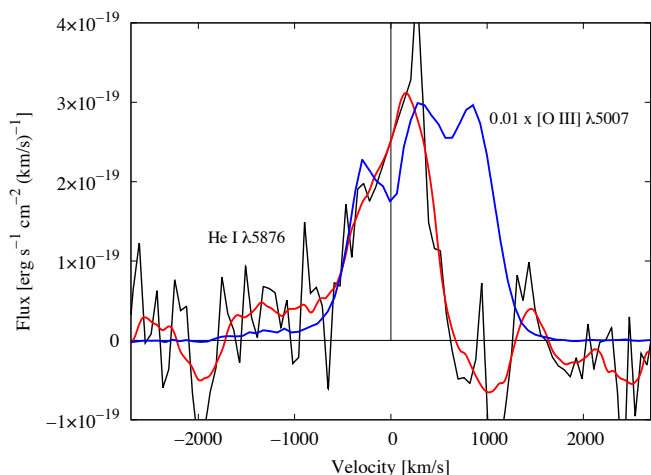


Fig. 22. Same in Fig. 18, but for He I $\lambda 5876$ (black, and smoothed in red) instead of [Ne III] $\lambda 3869$. The [O III] profile was multiplied by a factor of 0.01 to match the He I line. LMC rest frame velocity is marked by a vertical thin line. The red side of the He I line appears depreciated compared to [O III], similar to H β in Fig. 15.

seen for [S II] $\lambda\lambda 4069,4076$ in Fig. 21, but the low signal-to-noise does not allow us to draw firm conclusions on that part of the line profile. Interestingly enough, the full view SNRC observations of [S II] $\lambda\lambda 6716,6731$ by Sandin et al. (2013, their Figure 2) does show a blue wing between $-1\,200$ km s $^{-1}$ and -700 km s $^{-1}$. Our choice to center the [O II] doublet on 3727.5 Å is because this does not introduce any bias for either of the two doublet components. What is intrinsically assumed by centering on 3727.5 Å is that we assume that $I_{[\text{O II}] \lambda 3729}/I_{[\text{O II}] \lambda 3726} \approx 1.11$, which means $n_e \sim 350$ (400) cm $^{-3}$ for $T \sim 20\,000$ (30 000) K. According to our multilevel model, the intensity ratio decreases from ≈ 1.35 to ≈ 0.38 as electron density increases from 10^2 cm $^{-3}$ to 10^4 cm $^{-3}$.

Our observed $I_{[\text{S II}] \lambda\lambda 4069,4076}/I_{[\text{O II}] \lambda\lambda 3726,3729}$ ratio is ~ 0.06 . For the temperature interval $10\,000 - 15\,000$ K and density interval $500 - 1\,000$ cm $^{-3}$, our multilevel model atoms translate the observed ratio into an abundance ratio of $\text{S/O} = 0.05 \pm 0.01$, and thus a mass ratio $M_S/M_O = 0.10 \pm 0.02$. The models of Chieffi & Limongi (2013) predict a ratio of $0.05 - 0.06$ for rotating progenitors for progenitor masses between $13 - 20 M_\odot$, and between $0.05 - 0.13$ for non-rotating (with 0.05 for $20 M_\odot$). The more recent model of Sieverding et al. (2020) predicts $M_S/M_O = 0.085$ from their $11.8 M_\odot$ model for the inner ejecta and $0.12 M_\odot$ for all ejecta. Williams et al. (2008) assumed $M_S/M_O = 0.05$ in their models, and underproduced [S III] 18μ and [S IV] 10μ by factors of ~ 1.4 and ~ 2.8 , respectively, when we adjust their results with more accurate slit compensations. It therefore appears as if their model would fit the *Spitzer* data better with $M_S/M_O \sim 0.1$, which is consistent with both Chieffi & Limongi (2013) and Sieverding et al. (2020), albeit perhaps not for non-rotating low-mass progenitors in the case of Chieffi & Limongi (2013). However, the model of Williams et al. (2008) gives an $I_{[\text{S II}] \lambda\lambda 4069,4076}/I_{[\text{O II}] \lambda\lambda 3726,3729}$ ratio which is ~ 0.09 , and that is on the high side compared to our observations already with $M_S/M_O = 0.05$.

M_S/M_O can also be estimated from our slit 2 data for which we have $I_{[\text{S II}] \lambda\lambda 6716,6731}/I_{[\text{O II}] \lambda\lambda 7319-7331} \sim 9.0$. This is similar to ≈ 8.4 by Kirshner et al. (1989), and 10 in the model of Williams et al. (2008) assuming $\text{S/O} = 0.1$. Our multilevel atom modeling shows that a temperature $\gtrsim 20\,000$ K is needed to excite

O $^+$ to emit [O II] $\lambda\lambda 7319-7331$ at the observed relative intensity. In particular, for the [O III] temperature $T \sim 23\,000$ K, $I_{[\text{S II}] \lambda\lambda 6716,6731}/I_{[\text{O II}] \lambda\lambda 7319-7331} \sim 7$ for $\text{S/O} = 0.1$ and electron densities estimated by Sandin et al. (2013). The ratio rises steeply below $20\,000$ K.

Another way to estimate a temperature in the [O II]-emitting regions is from the ratio $I_{[\text{O II}] \lambda\lambda 3726,3729}/I_{[\text{O II}] \lambda\lambda 7319-7331}$, but for this we have to combine slits 1 and 2. Using the slit correction factors 7.2 and 6.3 , respectively, we obtain ~ 6.2 , which is very close to ~ 6.5 by Kirshner et al. (1989), but very different from the modeled flux by Williams et al. (2008), which is ≈ 14.7 . Our multilevel model suggests very high temperatures (well above $30\,000$ K) to get a ratio below 8.0 , which appears unlikely. Since our flux agrees with that of Kirshner et al. (1989), a possible explanation could be that [O II] $\lambda\lambda 7319-7331$ is contaminated by [Ca II] in both our slit 2 and the data in Williams et al. (2008). Such contamination (at 20% level) was already discussed by Kirshner et al. (1989).

A combination of slits 1 and 2 can also be used to estimate an [S II]-temperature from $I_{[\text{S II}] \lambda\lambda 6716,6731}/I_{[\text{S II}] \lambda\lambda 4069,4076}$, which with our slit compensations is ~ 30 . This is much higher than ~ 17 by Kirshner et al. (1989), and inconsistent with ~ 9.4 by Morse et al. (2006) as well as the model by Williams et al. (2008) which predicts ~ 7.4 . Our multilevel models show some density dependence, but intensity ratios such as those by Morse et al. (2006) and Williams et al. (2008) require temperatures at least as high as our derived [O III] temperature from slit 1, whereas our ratio and that of Kirshner et al. (1989) indicate temperatures of well below $10\,000$ K and around $15\,000$ K, respectively. Comparing observations through different slits, and at different epochs, admittedly increases the risk of systematic errors, so to make a consistency check we have used the full SNRC [S II] spectra of Sandin et al. (2013) to make artificial observations of [S II] through slits 1 and 2. From this exercise we find that the slit compensation for [S II] $\lambda\lambda 6716,6731$ is 6.5 for slit 1 and 7.7 for slit 2 (instead of the values 7.2 and 6.3 , as indicated by [O III]). This is not large enough to change our $I_{[\text{S II}] \lambda\lambda 6716,6731}/I_{[\text{S II}] \lambda\lambda 4069,4076}$ ratio by much (and actually makes it even larger).

The source of inconsistency for $I_{[\text{S II}] \lambda\lambda 6716,6731}/I_{[\text{S II}] \lambda\lambda 4069,4076}$ could either lie in the large relative [S II] $\lambda\lambda 6716,6731$ flux we get for slit 2 compared to others (cf. Table 2), and/or the lower flux we measure for [S II] $\lambda\lambda 4069,4076$. The latter is not unreasonable since [S II] $\lambda\lambda 4069,4076$ is affected by H δ . From Brocklehurst (1971) we estimate that H δ would amount to $\sim 25\%$ of H β , which would decrease the $I_{[\text{S II}] \lambda\lambda 6716,6731}/I_{[\text{S II}] \lambda\lambda 4069,4076}$ ratio accordingly, if not corrected for. This effect, of course, does not affect the modeled results of Williams et al. (2008). Regarding [S II] $\lambda\lambda 6716,6731$ we can do a direct test against the VIMOS observations of Sandin et al. (2013) by placing artificial slits on the VIMOS images to simulate slits 1 and 2. From figure 3 of Sandin et al. (2013) it can be seen that $I_{[\text{S II}] \lambda\lambda 6716,6731}/I_{[\text{O III}] \lambda 5007}$ is never higher than ~ 0.8 , and for slits 1 and 2 we get ~ 0.47 and ~ 0.35 , respectively. Even if we allow for slight displacement of slit 2 due to atmospheric dispersion (which was not accounted for in the NTT/EMMI observations), the ratio will not increase by more than $\sim 20\%$. Careful check of possible erroneous background subtraction of [S II] $\lambda\lambda 6716,6731$, together with the fact that the flux of other lines through slit 2 agrees with the results of Kirshner et al. (1989) and Morse et al. (2006), leaves us no choice other than to suggest that the [S II] $\lambda\lambda 6716,6731$ flux could vary with time. If we use a ratio of 0.35 from a simulated slit 2, we obtain $I_{[\text{S II}] \lambda\lambda 6716,6731}/I_{[\text{S II}] \lambda\lambda 4069,4076} \sim 12$,

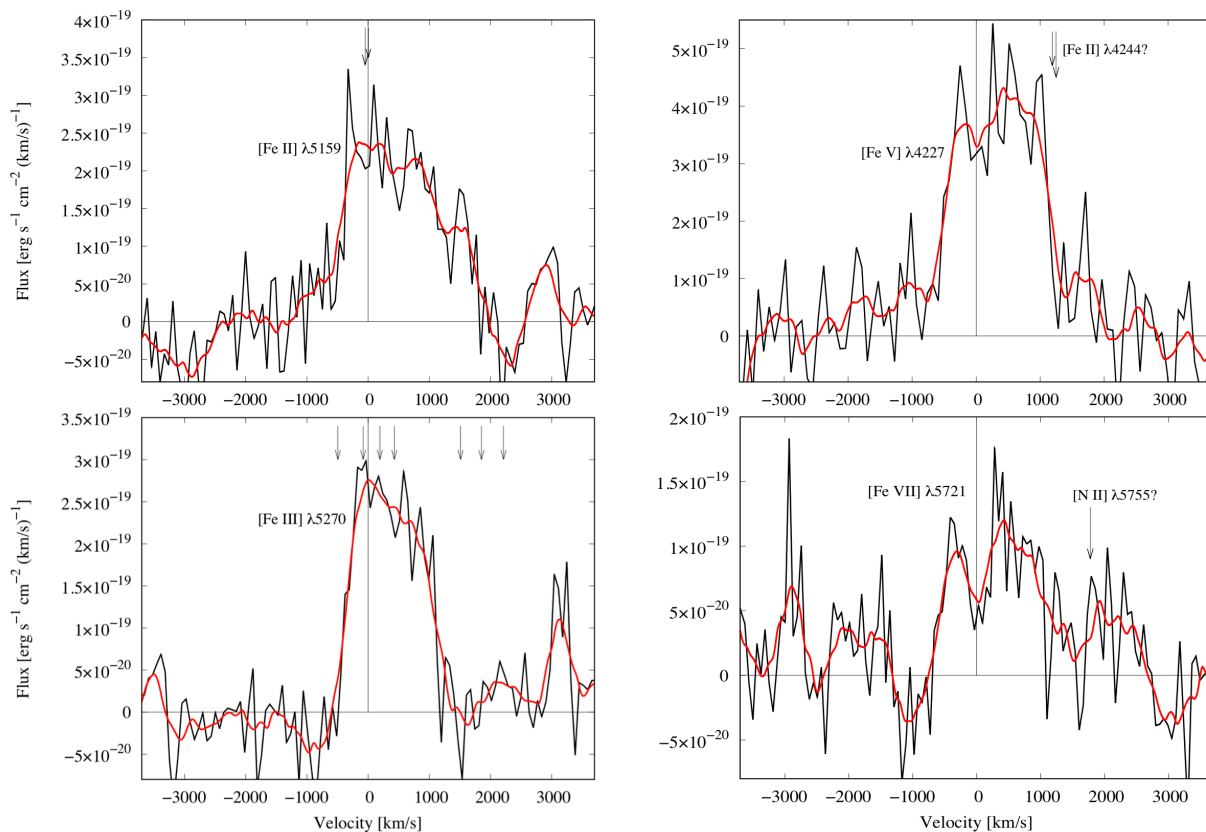


Fig. 23. Same in Fig. 22, but for several forbidden iron lines (black, and smoothed in red) instead of He I $\lambda 5876$. The velocities are centered on LMC rest frame velocities of [Fe II] $\lambda 5159$ (upper left panel), [Fe III] $\lambda 5270$ (lower left), [Fe V] $\lambda 4227$ (upper right) and [Fe VII] $\lambda 721$ (lower right). In each panel grey arrows mark velocities for other nebular lines seen in SNRs (Fesen & Hurford 1996). In particular, [Fe II] $\lambda 5159$ could be blended with (and even dominated by) [Fe VII] $\lambda 5159$. Note the broad wings of [Fe V] $\lambda 4227$, possibly reaching ± 2000 km s $^{-1}$.

which is more aligned with what other groups get, and would suggest an [S II] temperature of ~ 20000 K. The question remains regarding our high [S II] $\lambda\lambda 6716, 6731$ flux. We note that there are NTT/EMMI spectra covering [S II] $\lambda\lambda 6716, 6731$ from 1995 January, i.e., only one year before our NTT spectrum, which were shown in Caraveo et al. (1998). Unfortunately, these authors did not provide any fluxes. As there is activity going on in the south-western part of the PWN, at least between 1999–2007, the NTT spectra of Caraveo et al. (1998) could prove decisive regarding temporal variations in [S II] $\lambda\lambda 6716, 6731$. As discussed in Sect. 3.4.2, variations of elements other than oxygen on relative short time scale are conceivable.

Figure 22 shows that He I $\lambda 5876$ is very concentrated to within ± 500 km s $^{-1}$, in a fairly similar fashion to H β and [S II]. This means that hydrogen was deeply mixed into the core region during the explosion. Such mixing is expected from 3D explosion models (e.g., Hammer et al. 2010), and the amount of hydrogen mixed into the SNRC is sensitive to hydrodynamic instabilities at the composition interfaces (e.g., Wongwathanarat et al. 2015). A crude He/H ratio for the SNRC can be estimated from recombination theory, assuming similar ionization zones for H and He. The observed flux ratio of He I $\lambda 5876$ to H β for our slit 1 is ~ 0.24 , with at least 40% uncertainty. For a temperature in the range 10000 – 20000 K this translates into a mass ratio of He $^+$ /H $^+$ which is ~ 0.8 . As He 0 roughly has the same ionization potential as S $^+$, and [S II] emission dominates over [S III] in 0540 (Kirshner et al. 1989), a larger fraction of helium is likely to be neutral than that of hydrogen, and $M_{\text{He}}/M_{\text{H}}$ is likely to be larger

than 0.8 for the SNRC of 0540. The fraction of fully ionized helium could in principle be tested with He II $\lambda 4686$, but it sits in a spectral range with strong [Fe III] lines, and is not detected. SN 1987A may serve as interesting comparison for $M_{\text{He}}/M_{\text{H}}$, and we note that Jerkstrand et al. (2011) estimate that both H and He have $\sim 1.2 M_{\odot}$ each in the central 2000 km s $^{-1}$ region of SN 1987A, i.e., the mass ratio is $M_{\text{He}}/M_{\text{H}} \approx 1$, which is consistent with what we estimate for the SNRC of 0540.

Through slit 2 we also detect [Ar III] $\lambda 7136$ and [Ni II] $\lambda 7378$ with intensities relative to [O III] $\lambda 5007$ similar to what was reported by Kirshner et al. (1989) (cf. Table 2). On the other hand, the modeled [Ar III] $\lambda 7136$ flux by Williams et al. (2008) was more than twice as high as the observed relative fluxes of the line. This could suggest that Ar/O is less than the value of 0.1 assumed by Williams et al. (2008). Tuning the model results of Williams et al. (2008) with the observed [Ar III] $\lambda 7136$ fluxes then suggest $M_{\text{Ar}}/M_{\odot} \sim 0.02$. The nucleosynthesis yields in the model of Sieverding et al. (2020) give the same value, i.e., $M_{\text{Ar}}/M_{\odot} \sim 0.02$ for the total yield of Ar and O. The ratios in Chieffi & Limongi (2013) are ~ 0.01 for 13 – 20 M_{\odot} rotating, and 20 M_{\odot} for non-rotating progenitors, whereas the ratio is higher, ~ 0.02 , for 13 M_{\odot} non-rotating progenitors. Our multilevel model atoms suggest $M_{\text{Ar}}/M_{\odot} = 0.015(0.030)$ for equal ionization zones of Ar $^{2+}$ and O $^{2+}$ in the SNRC and for temperatures of 20000 (30000) K. The observed level of [Ar III] $\lambda 7136$ is therefore consistent with that expected from elemental yields in progenitor models and with [O III] temperatures.

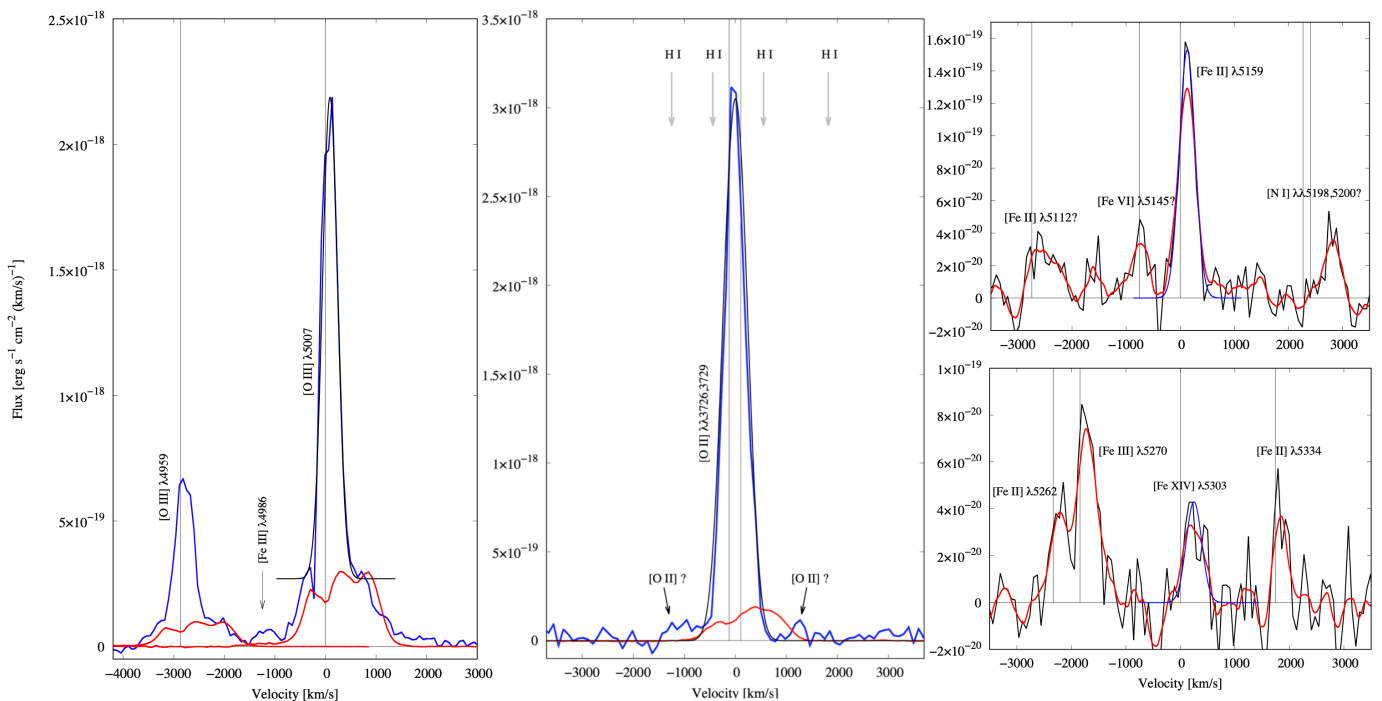


Fig. 24. Spectra of forbidden lines from F1 (cf. Figs. 5 and 13). All spectra are in the LMC rest frame and the velocities are for [O III] $\lambda 5007$ (left), 3727.5 Å (middle), [Fe II] $\lambda 5159$ (upper right) and [Fe XIV] $\lambda 5303$ (lower right). For the oxygen lines, the line profiles of the emission from the SNRC in Figs. 16 and 20, multiplied by a factor of 0.01, have been included for comparison (in red). The narrow spectral lines are unresolved, as highlighted for [O III] $\lambda 5007$ and the [O II] doublet, where the solid black lines show Gaussians with the expected FWHM of the instrument at 5007 Å and 3727.5 Å, i.e., ~ 355 km s $^{-1}$ and ~ 476 km s $^{-1}$, respectively. Note the broad bases seen for [O III] and possible broad base wings for [O II] $\lambda\lambda 3726,3729$. Lines of the H I Balmer series are marked in the middle panel. For the iron lines, Gaussians have also been drawn (in blue) according to the expected resolution. Several other lines have also been marked/indicated. Red marks Savitzky-Golay fitting to the spectrum.

As shown in Fig. 17 ([Fe III] $\lambda 4986$), Fig. 20 ([Fe V] $\lambda 3726$) and Fig. 23 ([Fe II] $\lambda 5159$, [Fe III] $\lambda 5270$, [Fe V] $\lambda 4227$ and [Fe VII] $\lambda 5721$) we detect several forbidden iron lines through slit 1, with decent signal-to-noise. We also detect [Fe II] $\lambda\lambda 4287, 4414, 5044$, [Fe III] $\lambda\lambda 4658, 4881, 4986$, [Fe V] $\lambda\lambda 3783-3797$ and [Fe VII] $\lambda 5721$. The strongest line is [Fe III] $\lambda 4658$, but it blends with several other [Fe III] lines, as do also several [Fe II] lines around ~ 4474 Å. Through slit 2 we detect [Fe II] $\lambda 5159$ and [Fe III] $\lambda\lambda 4658, 5270$, but with poor signal-to-noise.

We have chosen to concentrate on presumably unblended lines observed through slit1. In general, the line profiles are similar to those of the [O II] lines. In particular this is the case for [Fe III] $\lambda 5270$ and the core of [Fe V] $\lambda 4227$, whereas [Fe VII] $\lambda 5721$ is noisy, and perhaps also affected by [N II] $\lambda 5755$ in the far red wing. In Fig. 23 we have marked the velocities corresponding to other lines detected in SNRs (Fesen & Hurford 1996) which could perhaps contribute to the lines we have highlighted. For example, [Fe II] $\lambda 4247$ could contribute to the red wing of [Fe V] $\lambda 4227$, and our identification of [Fe II] $\lambda 5159$ could instead be dominated by [Fe VII] $\lambda 5159$, in particular since we also detect [Fe VII] $\lambda 5721$. To test this we have used our nine-level model atom for Fe $^{6+}$, including data from Berrington et al. (2000) and Del Zanna et al. (2021, and references therein). For $n_e = 10^3$ cm $^{-3}$ and $T = 30\,000$ K, the expected strongest [Fe VII] lines are (in order and normalized to [Fe VII] $\lambda 5721$): [Fe VII] $\lambda 6089$, [Fe VII] $\lambda 3759$, [Fe VII] $\lambda 3587$, [Fe VII] $\lambda 4990$ and [Fe VII] $\lambda 5159$ with relative strengths 1.9, 1.4, 1.0, 0.7 and 0.5, respectively. Unfortunately, [Fe VII] $\lambda 3587$ and [Fe VII] $\lambda 6089$ are outside the spectral range of our slit 1 observations, although

the latter line can, after smoothing, be hinted in the NTT/EMMI spectrum. [Fe VII] $\lambda 3759$ is clearly detected through slit 1, and [Fe VII] $\lambda 4990$ may add to [Fe III] $\lambda 4986$ in Fig. 17. Judging from the weak measured flux of [Fe VII] $\lambda 5721$, and that [Fe VII] $\lambda 5159$ is not expected to be stronger, we conclude that the spectral line at ~ 5171 Å (and ~ 5160 Å through slit 2) is dominated by [Fe II] $\lambda 5159$. The line has a possible broad blue wing, which is also hinted for [Fe V] $\lambda 4227$ (cf. Fig. 23). However, since no such wing is expected for [Fe II] lines, it is probably not real. Deeper observations are needed to check the wing of the [Fe V] line.

3.4.2. Masses and abundances - a summary

In the previous section we estimated the relative abundances in 0540. We now summarize this and estimate the total ejecta mass of the elements we have discussed. The mass of O $^{2+}$ ions in the SNRC emitting [O III] $\lambda 5007$ is

$$M(\text{O}^{2+}) \approx 3.2 \times 10^{-5} \left(\frac{f_{[\text{O III}]\lambda 5007}}{10^{-13} \text{ erg cm}^{-2} \text{ s}^{-1}} \right) \left(\frac{D}{50 \text{ kpc}} \right)^2 \left(\frac{n_e}{10^3 \text{ cm}^{-3}} \right)^{-1} \left(\frac{j_{[\text{O III}]\lambda 5007}}{10^{-21} \text{ erg cm}^3 \text{ s}^{-1} \text{ sr}^{-1}} \right)^{-1} M_{\odot}. \quad (3)$$

Here $f_{[\text{O III}]\lambda 5007}$ is the dereddened flux for one of the slit positions with a slit correction included to account for the full SNRC. For the SNRC we get $f_{[\text{O III}]\lambda 5007} \sim 3.0 \times 10^{-13}$ erg cm $^{-2}$ s $^{-1}$. $j_{[\text{O III}]\lambda 5007}$ is the emissivity of the $\lambda 5007$ transition, which for $T = 23\,500$ K is $\sim 1.1 \times 10^{-21}$ erg cm 3 s $^{-1}$ sr $^{-1}$. For $n_e = 10^3$ cm $^{-3}$ one then gets $M(\text{O}^{2+}) \sim 9 \times 10^{-5} M_{\odot}$.

A similar estimate for $M(\text{O}^+)$ from $[\text{O II}] \lambda\lambda 3726, 3729$ gives $M(\text{O}^+) \sim 5 \times 10^{-5} M_\odot$ when we use $T = 20\,000$ K (and from this $j_{[\text{O II}]\lambda\lambda 3726, 3729} \sim 1.1 \times 10^{-21} \text{ erg cm}^3 \text{ s}^{-1} \text{ sr}^{-1}$). A combined mass of $M(\text{O}^+) + M(\text{O}^{2+}) \sim 1.4 \times 10^{-4} M_\odot$ may seem like a surprisingly low mass considering that about two solar masses of oxygen should be present in 0540 (if similar to, e.g., SN 1987A). However, this estimate is only for the amount of oxygen in the SNRC that has been recently shocked. Those shocks are thin due to intense radiative cooling. The cooling time, calculated from a simple six-level model atom of pure O^{2+} at $T = 30\,000$ K with $n_e = 10^3 \text{ cm}^{-3}$, is ~ 0.02 years, and at $T = 50\,000$ K it is ~ 0.024 years. The similar numbers for pure O^+ at $T = 20\,000$ K and $T = 30\,000$ K are ~ 0.023 years and ~ 0.02 years. The real cooling time is longer if the shocked gas starts out hotter than $T = 50\,000$ K, although this is not so important since the cooling function for pure oxygen peaks around $\sim 2 \times 10^5$ K (cf. Borlowski & Shull 1990), and falls monotonically towards lower temperatures. More important is that the cooling is counteracted by photoionization of ambient photons from the PWN. With this in mind, a lower limit on the cooling time is ~ 0.05 years. Thus, $\sim 1.4 \times 10^{-4} M_\odot$ has to be replenished every ≥ 0.05 years, which means $\sim 0.3 M_\odot$ of shocked oxygen in ≥ 100 years.

Williams et al. (2008) did shock modeling for a similar situation where they assumed a low-velocity shock of 20 km s^{-1} aided by photoionization of PWN photons to account for the heavy-element ejecta lines. This is much lower than the shock velocity in Borlowski & Shull (1990) for Cas A, although that study only included preionization by photons produced by the shock. The oxygen column density of the emitting region in Williams et al. (2008) is $\sim 10^{14} \text{ cm}^{-2}$, and the mass flux of ejecta flowing into the low-velocity shocks is $\sim 0.01 M_\odot \text{ yr}^{-1}$, which appears consistent with our estimate of $\lesssim 0.003 X_{\text{other}} M_\odot \text{ yr}^{-1}$, where $X_{\text{other}} > 1$ is the correction factor to include all elements, and not only oxygen.

The mass fractions we estimated in Sect. 3.4.1 for the SNRC of 0540, namely $\text{O} : \text{Ne} : \text{S} : \text{Ar} = 1 : 0.07 : 0.10 : 0.02$ and $\text{H} : \text{He} = 1 : \geq 0.8$, are thus sampled over a very small fraction of the inner ejecta at any given time. How representative these numbers are for all inner ejecta is not very clear. However, one could imagine that there could be fluctuations on moderate time scales if the low-velocity shocks run into regions which are not fully microscopically mixed. This could be the reason for the apparent elevated sulphur abundance indicated by our NTT/EMMI observations.

3.4.3. The halo and beyond

Added to the mass of the SNRC is the mass of ejecta in the unshocked freely moving supernova ejecta. According to Williams et al. (2008), the inner part of this is photoionized to O^{2+} , so we use Equation 3 with $n_e = 1 \text{ cm}^{-3}$ and $f_{[\text{O III}]\lambda 5007} \sim 1.5 \times 10^{-13} \text{ erg cm}^{-2} \text{ s}^{-1}$, which corresponds to the integrated broad base of $[\text{O III}]$ emission in Fig. 19, and assuming that the VIMOS/IFU field-of-view misses roughly one third of the halo emission. For the photoionized halo we further assume a temperature of $\sim 12\,000$ K, so that $j_{[\text{O III}]\lambda 5007} \sim 4 \times 10^{-22} \text{ erg cm}^3 \text{ s}^{-1} \text{ sr}^{-1}$. With these assumptions, the mass of O^{2+} in the halo, $M(\text{O}^{2+})_{\text{halo}} \sim 0.12 M_\odot$. The mass is most likely higher since $n_e = 1 \text{ cm}^{-3}$ only stems from the 4 a.m.u. at the inner boundary of the unshocked SN ejecta estimated by Williams et al. (2008). The average electron density could be $n_e < 1 \text{ cm}^{-3}$ in the unshocked $[\text{O III}]$ emitting halo. According to Williams et al. (2008), enough ionizing photons are produced to ionize $\sim 1 M_\odot$ halo ejecta. In a mixed abundance model by Blinnikov

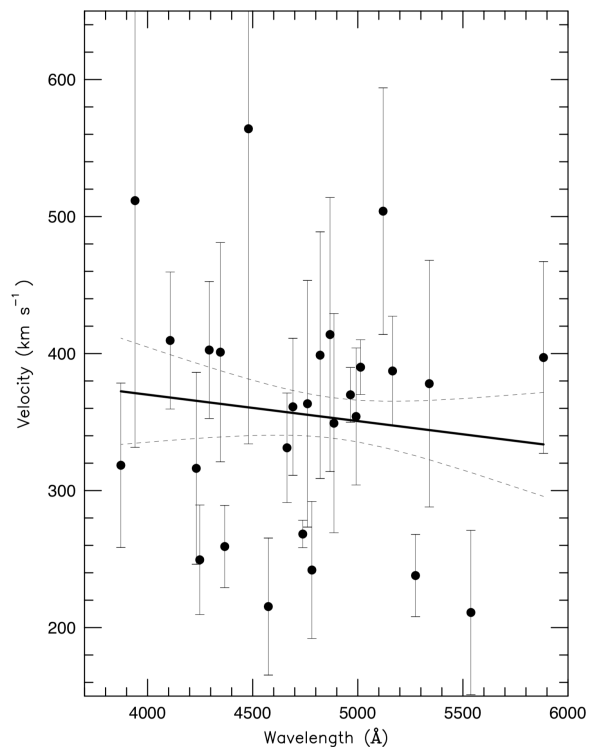


Fig. 25. Velocities estimated for emission lines from Filament F1. No doublets/multiplets are included except $[\text{O II}] \lambda\lambda 3726, 3729$. As can be seen, the wavelength calibration is stable across the spectrum. Interestingly, there is a group of lines with LMC redshift, although the majority has a redshift close to $\sim +120 \text{ km s}^{-1}$ compared to LMC redshift. See Table 3 and text for further details.

et al. (2000) for SN 1987A, which contains $\sim 2.0 M_\odot$ of oxygen with a drop in mass fraction just short of $2\,000 \text{ km s}^{-1}$, the mass fraction of oxygen falls from ~ 0.3 from $\sim 1\,300 \text{ km s}^{-1}$ to well below 0.1 at $2\,000 \text{ km s}^{-1}$. Choosing 0.1 for the 0540 halo makes our estimate for $M(\text{O}^{2+})_{\text{halo}}$ consistent with the ionized mass estimated by Williams et al. (2008), and if the total oxygen mass is similar to that in SN 1987A, roughly half of the oxygen is now confined to the filaments in the SNRC.

In SN 1987A, the total mass inside $2\,000 \text{ km s}^{-1}$ is dominated by He, O and H (cf. Blinnikov et al. 2000). We may assume the same situation for 0540. For a density of 4 a.m.u. at the inner boundary of the halo, corresponding to $V_{\text{halo,inner}} \sim 1\,200 \text{ km s}^{-1}$, and an outer velocity for the ionized halo of $V_{\text{halo,outer}} \geq 1\,900 \text{ km s}^{-1}$ (as is indicated by our results here), the total mass in this shell is $\sim 6.8 M_\odot$, assuming a flat density profile of the unshocked ejecta (cf. Williams et al. 2008). This compares well with the mixed model for SN 1987A by Blinnikov et al. (2000) in which the total mass inside the radius corresponding to this velocity is about $5 - 6 M_\odot$. It therefore seems that 0540 and SN 1987A could be fairly similar, and perhaps stem from progenitors with roughly similar zero-age-main sequence masses. The main difference between the dynamics in these events is of course the influence of a pulsar, which, if existent in SN 1987A (e.g., Cigan et al. 2019; Greco et al. 2021; Alp et al. 2021), plays a much smaller role than in 0540. On top of that, one has the 3D effects stemming from the explosion hydrodynamics, and possibly pre-explosion rotation. In our mass estimates for the halo we have compared with models assuming 1D, but from Sect. 3.1.1. it is evident that the halo is far from

spherically symmetric. This obviously introduces uncertainties in our mass estimates for the halo.

Moving further away from the SNRC, we introduced in Sect. 3.3.2 five interesting filaments which we have named F1-F5. For all filaments, the spectral lines are unresolved, except for F1, which displays broad bases of the [O III] $\lambda\lambda 4959, 5007$ line profiles, skewed to the red as compared to the positions of the narrow and strong (unresolved) peaks of these lines (cf. Fig. 24). The minimum and maximum velocities of the base (relative to LMC) are at least -900 km s^{-1} and $+1300 \text{ km s}^{-1}$, with a possible extension in the red to even larger velocities. No such features are seen in spectra of F2-F5. The presence of the broad base is consistent with the fact that F1 is projected onto the region showing the faint [O III] glow (cf. Fig. 10, top panel). As seen in the lower panel of Fig. 10, high redshifted velocities from the glow (which is emitted by the halo discussed above) occur close to the position of F1. Despite its projected proximity to the SNRC, the unresolved spectral components of filament F1 are therefore not part of the inner region of the SNR itself (see also below).

In Sect. 3.2 we connected the maximum recession velocity of the glow at F1 to the pulsar age. For a maximum velocity of $\gtrsim +1200 \text{ km s}^{-1}$, the pulsar would be older than 1200 years. Fig. 24 shows that this could be the case. However, a maximum velocity of $+1300 \text{ km s}^{-1}$ at the position of F1 would imply $v_{\text{true}} \sim 2130 \text{ km s}^{-1}$ for a pulsar age of 1200 years, which in turn would correspond to a radius of $\sim 10''8$ rather than $\sim 10''0$ in Fig. 5 for the same expansion as v_{true} in the westward direction orthogonal to the line-of sight. Fig. 5 does not really support this, which could indicate aspherical symmetry of the fastest glow even on smaller scales. Unfortunately, the VIMOS/IFU field does not reach this far from the pulsar to test the degree of non-sphericity over a larger scale, but Fig. 19 shows that even within the $13'' \times 13''$ field of view of VIMOS, there is large asymmetry of the fast “glow”. However, at the position of F1 specifically the broad base is fairly symmetric and less redshifted than the emission from the SNRC (highlighted in red in Fig. 24). Given the results in Sect. 3.2 and what is shown in Fig. 24, the pulsar age is closer to 1200 years than 1100 years. Given that the data we have analyzed were taken ~ 20 years ago, the pulsar age today should be close to 1200 years.

Fig. 24 also shows the [O II] $\lambda\lambda 3726, 3729$ doublet along with [Fe II] $\lambda 5159$, [Fe XIV] $\lambda 5303$, and other lines as marked in Fig. 24. [Fe II] $\lambda 5159$ and [Fe III] $\lambda 5270$ both showed hints of broad wings for the SNRC. Nothing like that is seen for the position at F1, but this could be due to the limited signal-to-noise. Of greater importance are the two spectral bumps on each side of the central unresolved blend of the [O II] doublet. One possible interpretation is that they originate in the same part of the ejecta as the [O III] halo, and possibly in its outermost part as a result of a transition of the photoionized state from O^{2+} to O^+ , at $v_{\text{true}} \sim 2000 \text{ km s}^{-1}$. Another possibility is that the bumps are due to Balmer lines emission from F1. We have marked the positions of them in the middle panel of Fig. 24. On the blue side H I $\lambda\lambda 3712, 3722$ emit at $\approx -1249 \text{ km s}^{-1}$ and $\approx -443 \text{ km s}^{-1}$, respectively (when we center on 3727.5 \AA), but on the red side, no H I line fits. Moreover, the strengths of the $\lambda 3712$ and $\lambda 3722$ lines are expected to be $< 1\%$ of [O II] $\lambda\lambda 3726, 3729$, using H β as template. Deeper observations are needed to test the [O II] interpretation, along with photoionization modeling like that in Williams et al. (2008).

Closing in on the narrow components of the lines from the filaments, the weighted velocity of individual lines can be used to test both the physical velocity of the filaments and to check

possible systematics in the wavelength calibration. The calibration is problematic far in the very blue due to warped spectra, which makes the velocities for [O II] $\lambda\lambda 3726, 3729$ systematically low. As an example, we show in Fig. 25 the velocities of the detected lines across the spectrum for F1. The velocity of [O II] $\lambda\lambda 3726, 3729$ was estimated using 3727.5 \AA (see below). We note that a group of lines tend to have LMC redshift, while most lines cluster at $\sim +120 \text{ km s}^{-1}$ compared to the LMC. The dashed lines in Fig. 25 shows 1σ uncertainty for the wavelength solution. Taking the extremes of this fit (i.e., the solid line in the figure) to assign a combined uncertainty, we arrive at $355 \pm 30 \text{ km s}^{-1}$ for F1. For the other filaments we find $260 \pm 25 \text{ km s}^{-1}$ for F2, $290 \pm 30 \text{ km s}^{-1}$ for F3, $255 \pm 20 \text{ km s}^{-1}$ for F4 and $240 \pm 20 \text{ km s}^{-1}$ for F5. This means that all of them have velocities consistent with LMC velocity, except for F1, which is redshifted by an extra $85 \pm 30 \text{ km s}^{-1}$.

In Table 5 we list [O III] temperatures of all filaments. The temperatures were calculated in the same way as for the SNRC in Sect. 3.3.2. For the filaments, we have assumed an electron density of $n_e = 10^3 \text{ cm}^{-3}$ (see below), but the difference in estimated temperature is very small for electron densities in the range $10^2 - \text{few} \times 10^3 \text{ cm}^{-3}$. The temperature is highest for F1. If we include [O III] $\lambda\lambda 4959, 5007$ with its full base we get $(3.6 \pm 0.4) \times 10^4 \text{ K}$. However, from the Gaussian fit for [O III] $\lambda 5007$ in Fig. 25 we estimate that only $\sim 60\%$ of the flux is in the spectrally unresolved component. If the base originates in a photoionized halo with a presumed temperature of $\lesssim 2 \times 10^4 \text{ K}$, no base is expected to be detected from F1 for the weak [O III] $\lambda 4363$ line, which is also confirmed by our data. For the unresolved component, a better estimate of the [O III] temperature could therefore be $\gtrsim 5.5 \times 10^4 \text{ K}$. For the other filaments we estimate $(3.0 \pm 0.4) \times 10^4 \text{ K}$ (F2), $(1.8 \pm 0.2) \times 10^4 \text{ K}$ (F3) $(1.9 \pm 0.2) \times 10^4 \text{ K}$ (F4) and $(2.5 \pm 0.4) \times 10^4 \text{ K}$ (F5). The temperatures are somewhat higher than reported in our preliminary analysis in Serafimovich et al. (2005). For the central peak of [O II] $\lambda\lambda 3726, 3729$, we tested possible skewness to reveal the density of F1 (cf. Sect. 3.4.1 for how $I_{[\text{O II}] \lambda 3729} / I_{[\text{O II}] \lambda 3726}$ depends on density). Unfortunately, the spectral resolution is too poor to draw any such conclusions.

The spectra of all filaments show many forbidden iron lines. Filaments F1 and F3 have lines of [Fe II] and [Fe III], whereas F2 also shows [Fe V] $\lambda 4227$. Filaments F1, F4 and F5 show the very highly ionized [Fe XIV] $\lambda 5303$ (cf. Fig. 25), possibly with some contamination from [Ca V] $\lambda 5309$. There is also a line at $\lambda 5537.9$ for F1 that could be [Ar X] $\lambda 5534$. Based on these findings, the X-ray morphology of the remnant, the filament dispositions (cf. Fig. 2), and the high temperatures of the filaments, it is likely that filaments F1, F2, F4 and F5 are ionized by the SNR, most likely through shock activity. Filament F3 sits $1/4$ east of the pulsar and has no physical connection to the remnant. However, it is not a normal H II region in the LMC. Typical [O III] temperatures in, e.g., the 30 Doradus region vary rather mildly ($\pm 140 \text{ K}$) from the average value of 10270 K (Krabbe & Copetti 2002). The high [O III] temperature of F3, $18000 \pm 2000 \text{ K}$, suggests that it too is affected by the remnant, presumably through intense photoionization by high-energy photons.

Brantseg et al. (2014) studied the radio and X-ray emission from 0540, and we note that one of the regions they studied in detail includes our filament F4. Their models of the detected X-ray emission from this region indicate a shock temperature of $T_s \sim 7 \times 10^6 \text{ K}$. Three of the five other outer SNR regions they studied have similar temperatures, whereas the two others are cooler and hotter by a factor of ~ 2 . Using the Rankine-Hugoniot relations for fully ionized plasma, this translates into a shock

speed of $V_s \sim 510 \text{ km s}^{-1}$ for the region including F4 (e.g., Brantseg et al. 2014). Brantseg et al. (2014) argue for a sufficiently short timescale for temperature equilibration between electrons and ions, and we will use this here as well. Brantseg et al. (2014) also estimated the electron density of the X-ray-emitting regions, and arrive at $n_e \sim \text{a few cm}^{-3}$, and for the region including F4 in particular, $n_e \sim 4.0^{+0.6}_{-0.3} \text{ cm}^{-3}$.

A shock with velocity $V_s \sim 510 \text{ km s}^{-1}$ can collisionally ionize iron up to Fe^{18+} , with almost no iron in Fe^{13+} if the plasma is in collisional equilibrium (e.g., Arnaud & Raymond 1992). However, with the low densities in the shocks studied by Brantseg et al. (2014), collisional equilibrium is not fully established, and one has instead to resort to non-equilibrium ionization. More specifically, the collisional ionization time-scale of Fe^{13+} to Fe^{14+} is

$$t_{\text{ion}}(\text{Fe}^{13+}) \approx 3.2 \left(\frac{C_{\text{ion}}(\text{Fe}^{13+})}{10^{-9} \text{ cm}^3 \text{ s}^{-1}} \right)^{-1} \left(\frac{n_e}{10 \text{ cm}^{-3}} \right)^{-1} \text{ years}, \quad (4)$$

where $C_{\text{ion}}(\text{Fe}^{13+})$ is the collisional ionization rate coefficient for collisions from Fe^{13+} . We use the formalism of Arnaud & Rothenflug (1985) which gives $C_{\text{ion}}(\text{Fe}^{13+}) \approx 6.8 \times 10^{-10} \text{ cm}^3 \text{ s}^{-1}$ for $T_s \sim 7 \times 10^6 \text{ K}$, which means $t_{\text{ion}}(\text{Fe}^{13+}) \sim 12$ years for $n_e = 4.0 \text{ cm}^{-3}$. The corresponding time scales $t_{\text{ion}}(\text{Fe}^{14+})$, $t_{\text{ion}}(\text{Fe}^{15+})$ and $t_{\text{ion}}(\text{Fe}^{16+})$ are ~ 15 years, ~ 29 years and ~ 230 years, respectively. For young enough shocks, there will certainly be no iron ionized beyond Fe^{16+} , and for shocks younger than a couple of decades, Fe^{13+} should still be present. Brantseg et al. (2014) estimate an ionization time scale of ~ 1600 years for $n_e = 4.0 \text{ cm}^{-3}$, which seems unreasonably long for F4, unless the density of the shocked gas is substantially higher than 4.0 cm^{-3} . This could be the case for a low filling factor of the shocked gas.

The ionization time scales should be compared with recombination time scales, and for the recombination from Fe^{13+} to Fe^{12+} , $t_{\text{rec}}(\text{Fe}^{13+})$, we write

$$t_{\text{rec}}(\text{Fe}^{13+}) \approx 317 \left(\frac{\alpha_{\text{rec}}(\text{Fe}^{13+})}{10^{-11} \text{ cm}^3 \text{ s}^{-1}} \right)^{-1} \left(\frac{n_e}{10 \text{ cm}^{-3}} \right)^{-1} \text{ years}, \quad (5)$$

where $\alpha_{\text{rec}}(\text{Fe}^{13+})$ is the recombination rate coefficient. If we use the results of Schmidt et al. (2006), i.e., $\alpha_{\text{rec}}(\text{Fe}^{13+}) \approx 1.55 \times 10^{-11} \text{ cm}^3 \text{ s}^{-1}$ at $T_s \sim 7 \times 10^6 \text{ K}$, we get $t_{\text{rec}}(\text{Fe}^{13+}) \sim 510$ years for $n_e = 4.0 \text{ cm}^{-3}$. This means that once ionized to Fe^{13+} , the ISM shocked by SNR 0540-69.3 would not have time to recombine. Collisional ionization to Fe^{14+} is far superior, which immediately shows that the low-density shocked ISM with $n_e = 4.0 \text{ cm}^{-3}$ is not the source of the low-ionization lines from filament F4.

This is further strengthened if we study the cooling time of the shocked gas. For this we use an expression for the shocked circumstellar matter of SN 1987A, which reads (Grönigsson et al. 2006), valid for $100 \text{ km s}^{-1} \lesssim V_s \lesssim 600 \text{ km s}^{-1}$,

$$t_{\text{cool}} \approx 580 \left(\frac{n_{\text{filament}}}{10^3 \text{ cm}^{-3}} \right)^{-1} \left(\frac{V_s}{500 \text{ km s}^{-1}} \right)^{3.8} \text{ years}. \quad (6)$$

Here n_{filament} is the density of the filament. Even though this expression was tailored for the enriched He and N abundances of SN 1987A, it is obvious that the cooling time for 0540 is far too long for the shocked gas to cool down to the temperature derived from [O III].

From our discussion we find that the shocks running into the low-density ISM are adiabatic. Fe^{13+} is most likely in a transitory state to becoming further ionized, although full collisional equilibrium will not be attained. This plasma cannot be the same

as that emitting low-ionization like, e.g., [O III] (see below). The situation could therefore be similar to that in the Cygnus Loop (Ballet et al. 1989; Fesen & Hurford 1996; Raymond et al. 2015), N49, N63A, N103b and SN 1987A in the LMC (Danziger & Dennefeld 1976; Murrin et al. 1978; Dopita & Mathewson 1979; Grönigsson et al. 2006; Dopita et al. 2019), Puppis A (Clark et al. 1979) and SNR S8 in IC 1613 (Fesen & Weil 2020), all in which coronal iron lines coexist with lower-ionization iron lines. The situation is different from that in, e.g., SNR 1E0102.2-7219 in the SMC (Vogt et al. 2017), where only coronal lines are seen, nicely tracing the blast wave. We return to [Fe XIV] $\lambda 5303$ below.

The low-ionization lines from F1, F2, F4 and F5 likely originate as results of shocks with lower velocity than the shocks studied by Brantseg et al. (2014). From Filament F1 we detect Fe^{6+} lines, and in collisional equilibrium this ion peaks in abundance at $\sim (2-3) \times 10^5 \text{ K}$, corresponding to a shock speed of $\sim 100 \text{ km s}^{-1}$. Since we expect the shock speed in the filaments to scale as $\propto n_{\text{filament}}^{1/2}$, the density of the filaments emitting the low-ionization lines should be $\sim 4.0 (V_{\text{X-ray}}/V_{\text{opt}})^2 \text{ cm}^{-3}$, where $V_{\text{X-ray}}$ and V_{opt} are the shock speeds in the X-ray emitting region and low-ionization line emitting region, respectively. This points to $n_{\text{filament}} \sim 10^2 \text{ cm}^{-3}$ for the low-ionization line emitting regions. According to Equation 5, this would mean $t_{\text{cool}} \sim 13$ years (for $V_{\text{opt}} = 100 \text{ km s}^{-1}$). These shocks are therefore radiative (as opposed to the adiabatic shock created by the blast wave). If the postshock gas is in near pressure equilibrium, the density in the [O III]-emitting region should be a factor of ~ 10 higher than that emitting [Fe VII] lines, i.e., $\sim 10^3 \text{ cm}^{-3}$. This justifies our choice of 10^3 cm^{-3} when we estimated the [O III] temperature earlier in this subsection. A decisive measurement for this picture would be to measure the density from [O II] and/or [S II]. Unfortunately, [S II] emits outside the spectral range of our filament spectra, and the spectral resolution is too low to draw conclusions from [O II].

While four of our filaments have velocities consistent with LMC velocity, Figs. 24 and 25 show that filament F1 recedes by $85 \pm 30 \text{ km s}^{-1}$ compared to the others. This is also the only filament which is not situated at, or outside the projected position of the blast wave. According to the Rankine-Hugoniot shock relations for polytropic index $\gamma = 5/3$, this means that the shocked gas in the low-ionization line-emitting medium is accelerated to $3V_{\text{opt}}/4$. For a spherically-symmetric model with a shock radius corresponding to $\sim 20'' - 25''$ at the distance of LMC, and $8/5$ for the projected distance between the pulsar and F1, the observed $85 \pm 30 \text{ km s}^{-1}$ for F1 translates into $90 \pm 35 \text{ km s}^{-1}$. If we correct for the factor $4/3$, we arrive at $V_{\text{opt}} = 120 \pm 45 \text{ km s}^{-1}$, which is fully consistent with what we estimated from the estimated shock velocity required to ionize up to Fe^{6+} for a radiative shock being responsible for the low-ionization lines. In reality, there are most likely a range of shock velocities depending on the distribution of densities, much in the same way as for the well-studied inner ring of SN 1987A (Grönigsson et al. 2006). We reiterate that the broad and narrow lines from the F1 region come from completely different components; the broad [O III] lines come from the halo of freely coasting SN ejecta, while the narrow lines from the shocks at the SNR front on the rear side of the remnant, presumably some $\sim 20'' - 25''$ from the pulsar. Filaments F2, F4 and F5 are moving mainly orthogonal to the line-of-sight, and do not show any blue- or redshift compared to LMC velocity.

In this picture, the [Fe XIV] $\lambda 5303$ velocity for F1 should be more redshifted than lines from low-ionization ions, i.e., if it comes from behind the blast wave. Although [Fe XIV] $\lambda 5303$

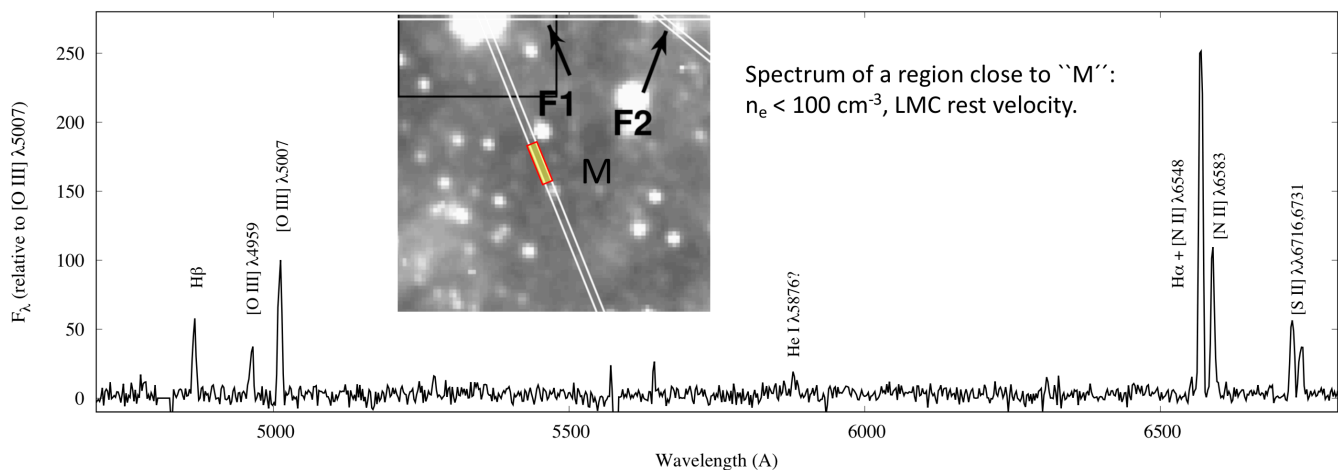


Fig. 26. Spectrum of a region (marked in yellow) along the NTT/EMMI slit close to the “N-rich” region identified by Mathewson et al. (1980), here marked with “M”. The map in the inset is from Fig. 2. The spectrum was dereddened with $E(B - V) = 0.19$, and plotted relative to [O III] $\lambda 5007$. The electron density is from [S II] $\lambda\lambda 6716, 6731$, and the velocity of the emitting gas is LMC rest velocity. See text for further details.

may be slightly more redshifted than the bulk of emission lines (cf. Table 3 and Fig. 25), we do not see a several hundred km s^{-1} difference in velocity. There could be at least two explanations for this. The first is that we have misinterpreted another spectral line for being [Fe xiv] $\lambda 5303$, and the second is that if [Fe xiv] $\lambda 5303$ is indeed the correct identification, it is not emitted immediately behind the inter-cloud fast shock. Instead it originates from closer to the clouds. To check the first explanation, we focus on the right panels of Fig. 25 in which the stronger iron lines peak around $130 - 140 \text{ km s}^{-1}$, whereas [Fe xiv] $\lambda 5303$ peaks at $\sim 180 \text{ km s}^{-1}$. The Gaussian fit to [Fe xiv] $\lambda 5303$ is consistent with a single feature. The FWHM is $\approx 335 \text{ km s}^{-1}$, so any thermal broadening of the line is impossible to trace. That the line may appear somewhat broader than the Gaussian fit is likely due to poor signal-to-noise. In the line list by Fesen & Hurford (1996), there are a few lines close to [Fe xiv] $\lambda 5303$, namely [Fe II] $\lambda 5297$ and [Ca v] $\lambda 5309$. (None of them marked in Fig. 25). Their velocities relative to [Fe xiv] $\lambda 5303$ are -340 km s^{-1} and $+357 \text{ km s}^{-1}$, respectively. Whereas there is no hint for the [Fe II] line, [Ca v] line could be responsible for a possible slight extension of the [Fe xiv] $\lambda 5303$ main part of the line feature. This is why we have added the [Ca v] $\lambda 5309$ line in Tables 3 and 4. That [Fe xiv] $\lambda 5303$ is present seems solid.

But why is then [Fe xiv] $\lambda 5303$ from F1 not more redshifted than the lower-ionization iron lines in Fig. 25? The results of Miceli et al. (2006) may provide a clue. These authors performed 2D axial symmetric simulations of a fast shock interacting with a cloud in a tenuous medium. The setup was intended to model the X-ray emission from the Vela SNR, but general conclusions can be drawn. They tested two geometries, a spherical cloud, and an elliptical cloud with major axis along the shock direction (to simulate a filament). In the spherical cloud case (which we will concentrate on), the shock interaction results in something like a two-temperature situation, where soft X-rays are produced in the transmitted shock in the cloud, and a higher-temperature region in the shocked tenuous medium emits harder X-rays. What is important is that the hard X-ray emission does not mainly come from region immediately behind the blast wave. It instead comes from a halo around the cloud. Conduction between the cloud and the hot shocked tenuous medium drives an

evaporation of the cloud and the formation of a hot diffuse halo. We suggest that [Fe xiv] $\lambda 5303$ originates in this zone along with the hard X-rays. As this zone is tied to the cloud, there should not be any significant difference in velocity as determined from the line profiles. Future tests of this scenario would be to study the 0540 filaments in higher spectral resolution, as well as in the red part of the spectrum to probe, e.g., [Fe x] $\lambda 6374$ and [Fe xi] $\lambda 7892$, as well as to measure the [S II] density.

Moving to regions in the south-western part of SNR 0540-69.3, the possibly N-rich filament identified by Mathewson et al. (1980) is outside the reach of our slits and the field-of-view of the VIMOS/IFU of Sandin et al. (2013). However, our NTT/EMMI slit covers a region close to it which shows strong nebular emission. In Fig. 26 we show this region and its spectrum, dereddened using $E_{B-V} = 0.19$, and normalized to [O III] $\lambda 5007$. (The region discussed by Mathewson et al. 1980, is marked with an “M”.) The electron density from [S II] in the yellow-marked region along the EMMI slit is $\lesssim 10^2 \text{ cm}^{-3}$, which is fully consistent with an H II region in the LMC, as is also the velocity of the emitting region. However, there is an oddity with the overall spectrum in that it is very red. With $E_{B-V} = 0.19$ the Balmer decrement $H\alpha/H\beta \sim 5.0$, which is almost a factor of ≈ 1.8 higher than expected from an H II region. The simplest solution to this is that the emission comes from an H II region, but that $E_{B-V} \sim 0.95$ for this area rather than the value we use for 0540. From a visual inspection of Fig. 1 it is clear that the nebulous emission is less pronounced in an area that includes both the yellow part along the slit in Fig. 26 and the region M highlighted by Mathewson et al. (1980). Absence of [O III]-emission is also very clearly seen for this region in Figure 1A of Mathewson et al. (1980). Such patchy structure is expected if there are dusty regions embedded in a large H II region like N 158 (Heinze 1956) with its superbubble around the OB association LH 104 in the north (Lucke & Hodge 1970; Testor & Niemela 1998), which dominates this part of the LMC. Finally, we note that the filter used by Mathewson et al. (1980) to study [N II] was centered on 6584 \AA with a FWHM of 16 \AA . With an LMC redshift of 270 km s^{-1} , $H\alpha$ is redshifted to $\sim 6569 \text{ \AA}$ and [N II] $\lambda 6584$ to 6589 \AA . In the spectrum of Fig. 26, $I_{[\text{N II}]\lambda 6584}/I_{H\alpha} \sim 2.2$, and if this is also the case for region “M”, $\sim 20\%$ of the emission in the 6584 \AA filter used by Mathewson et al. (1980) is due to $H\alpha$

(if Gaussian), however, the exact fraction being sensitive to the transparency of the blue wing of their 6584 Å filter.

4. Conclusions

A combination of [O III] filters centered on 0 km s⁻¹ and +3 000 km s⁻¹ was used to reveal structures in the central part of SNR 0540-69.3 (SNRC), not previously detected by HST filters, and disproves some structures indicated by the VLT/VIMOS integral-field-unit (IFU) observations by Sandin et al. (2013). We detect [O III] emission out to ~ 10'' from the pulsar, which corresponds to an average ejecta velocity of ~ 2 000 km s⁻¹ for an age of 1 200 years. The filter images complement the IFU images in [O III] to suggest ring-like structures around a symmetry axis from north-east to south-west, also seen in [S II] (Sandin et al. 2013). In a 3D-representation, the symmetry axis crosses the projected pulsar position ~ 500 km s⁻¹ on the receding side of the remnant, which if it is due to pulsar activity, could indicate that the pulsar shares the same general redshift as the SNRC. Such pulsar activity could occur if the pulsar jet is oriented along this axis rather than as displayed in Fig. 6. It is emphasized that there is evidence for substantial past and present activity along the suggested jet axis (cf. Lundqvist et al. 2011), but the rings could also have an origin related to the supernova explosion.

SNR 0540-69.3 was also studied through two slits roughly orthogonal to each other (PA = 22° and PA = 88°). Several new spectral lines are identified for the SNRC, and 2D spectroscopy along the slits reveals fast [O III]-emitting ejecta outside the SNRC corresponding to a space velocity of $v_{\text{true}} \sim 2\,100$ km s⁻¹ on the receding western part. This velocity agrees with our imaging, as well as a pulsar age of $\approx 1\,200$ years. In the southwest on the receding side of $v_{\text{true}} \gtrsim +2\,200$ km s⁻¹. On the approaching side, the [O III] emission reaches $v_{\text{true}} \sim 1\,900$ km s⁻¹. Although substantially weaker, [Ne III] emission has similar structure to that of [O III], whereas [O II], [S II], [Ar III] and H β are emitted by the more compact structure of the SNRC, in agreement with the [S II] IFU image of Sandin et al. (2013). The luminosity-weighted average of the lines is $+440 \pm 80$ km s⁻¹ with respect to the host galaxy, which is accord with previous findings, as well as the possible pulsar motion.

The average [O III] temperature of the SNRC is $23\,500 \pm 1\,800$ K, which is somewhat lower than previously reported, mainly because we have included a correction of the [O III] $\lambda 4363$ flux due to the blend with H γ . The electron density derived from [S II] $\lambda \lambda 6716, 6731$ is found to be $n_e \sim 10^3$ cm⁻³, which is slightly higher than in the density map of Sandin et al. (2013).

The VIMOS/IFU data of Sandin et al. (2013) were used to construct slit correction factors for our spectroscopic data in order to estimate overall abundances and masses of various elements in the SNRC. Infrared data from *Spitzer* (Williams et al. 2008) were also included in these estimates. In particular, relative mass ratios were found to be O : Ne : S : Ar $\approx 1 : 0.07 : 0.10 : 0.02$. Those ratios are consistent with explosion models of 13 – 20 M $_{\odot}$ progenitors (e.g., Chieffi & Limongi 2013; Sieverding et al. 2020), as well as SN 1987A (cf. Jerkstrand et al. 2011). The argon abundance is a factor of ~ 2 lower than used in the models by Williams et al. (2008) (which was also suggested by those authors as a possibility). The fact that we detect H and He mixed in deep into the central region is a clear sign of explosive mixing, as in SN 1987A. The mass ratio of He/H in the SNRC is estimated to be at least ~ 0.8, which is another similarity with SN 1987A.

The mass of [O II] and [O III] emitting oxygen in the SNRC is only $\sim 1.4 \times 10^{-4}$ M $_{\odot}$, but the cooling time of shocked gas in the SNRC is so short ($\gtrsim 0.05$ years) that the mass flux through the low-velocity shocks in the SNRC can be up to $\sim 0.003 X_{\text{other}} M_{\odot} \text{ yr}^{-1}$, where X_{other} is the correction factor to include all elements, not only oxygen. This is on the low side compared with $\sim 0.01 M_{\odot} \text{ yr}^{-1}$ estimated by Williams et al. (2008). The rapid cooling of the shocked gas in the SNRC could in principle make it possible to detect fluctuations in the flux of lines other than those from oxygen if the SNRC is not microscopically mixed. We note a possible such fluctuations in [S II] $\lambda \lambda 6716, 6731$ between 1989–2006. This effect could potentially make abundance estimates for the whole SNRC vulnerable for elements other than oxygen in the SNRC. IFU images for various spectral lines separated in time by several years could resolve this uncertainty.

The fastest emitting [O III] ejecta (which have components with velocities in excess of 2 000 km s⁻¹) come from a freely coasting halo of photoionized supernova ejecta. The mass of the halo is ~ 0.12 M $_{\odot}$ if spherical symmetry is assumed. However, the halo shows clear asymmetry with no detectable emission on the receding side to the north and only weak emission on the approaching side to the south. On the approaching side, there appears to be a “wall”-like feature centered slightly to the north-west of the projected pulsar position and it has velocities more blueward than ~ -750 km s⁻¹. We have used the VIMOS/IFU results of Sandin et al. (2013) to constrain that structure. There is a hint of [O II] $\lambda \lambda 3726, 3729$ emission from fast photoionized ejecta (both approaching and receding), which would mark the outer boundary of the photoionized region. Oxygen-rich ejecta out to ~ 2 000–2 200 km s⁻¹, and a total mass of oxygen which is ~ 2 M $_{\odot}$ are yet other similarities with SN 1987A (cf. Jerkstrand et al. 2011, and references therein for properties of SN 1987A). However, for 0540 most of the oxygen is likely to be located in filaments in a pulsar-wind nebula, which for SN 1987A is not the case.

A third slit was placed along the western part of the supernova remnant shock. Two optical filaments, named F4 and F5, are detected for this slit position, and three further filaments (F1, F2 and F3) are identified for the PA = 88° slit. Although having an [O III] temperature of $18\,000 \pm 2\,000$ K, filament F3 lies too far from SNR 0540-69.3 to be physically connected to it, and is most likely an H II region in the vicinity of the remnant. The other filaments are hotter, and three of them (F2, F4 and F5) show [Fe XIV] $\lambda 5303$ emission. The hottest (F1), with an [O III] temperature in excess of 55 000 K, is redshifted by 85 ± 30 km s⁻¹ relative to the LMC redshift, and is located only 8'' west of the pulsar. We argue that the redshift was acquired when F1 was shocked by the SNR blast wave. Similar acceleration for F2, F4 and F5 would have occurred orthogonal to the line of sight since they show no red- or blueshift. Filament F4 overlaps with a region studied in X-rays by Brantseg et al. (2014), and including temperatures and densities from the X-ray modeling by these authors, we conclude that most of the optical lines from F1, F2, F4 and F5 come from radiative shocks in ISM clouds, overtaken by the supernova blastwave. The electron density of the [O III] emitting gas is estimated to be $\sim 10^3$ cm⁻³. Lines from more highly ionized ions, and in particular [Fe XIV] $\lambda 5303$, are argued to come from an evaporation zone in connection with the radiatively cooled gas. Future observations of these filaments at higher spectral resolution is needed to test these conclusions.

Finally, a portion of the slit with PA = 22° was used to probe a region close to a possibly N-rich filament identified by Mathewson et al. (1980). Our spectrum reveals that the emission is

highly reddened with a Balmer decrement of $H\alpha/H\beta \sim 5.0$, and that the emitting gas has a low electron density ($\lesssim 10^2 \text{ cm}^{-3}$). It is most likely emission from an H II region unrelated to the supernova. The severe reddening boosts red lines compared to, e.g., [O III] which is weak in this region. The [N II] filter used by Mathewson et al. (1980) could also have been affected by $H\alpha$ emission. An N-rich supernova filament in this region therefore seems unlikely.

Acknowledgements. We thank R. J. Cumming for helping out with the NTT observations and A. Koptsevich for being part of the preparations of the VLT observations. We are also grateful to C. Fransson, J. Larsson, C. Sandin and J. Sollerman for discussions. The research of PL is sponsored by the Swedish Research Council. Early on in this project, PL was a Research Fellow at the Royal Swedish Academy supported by a grant from the Wallenberg Foundation, and NL was supported by the Swedish Institute. YuAS is partially supported by the Russian Foundation for Basic Research (RFBR) according to the project 19-52-12013. We made use of the Atomic Line List (Van Hoof 2018), and the CHIANTI data base. CHIANTI is a collaborative project involving George Mason University, the University of Michigan (USA), University of Cambridge (UK) and NASA Goddard Space Flight Center (USA). This research has also made use of NASA's Astrophysics Data System Bibliographic Services.

References

- Alp, D., Larsson, J., Fransson, C. 2021, ApJ, in press (arXiv:2103.02612)
- Arnaud, M., & Raymond, J., 1992, ApJ, 398, 394
- Arnaud, M., & Rothenflug, R., 1985, A&AS., 60, 425
- Avila, G., Gero, R., & Beckers, J. M. 1997, in Optical Telescopes of Today and Tomorrow, SPIE 2871, ed. A. Ardeberg, 1135
- Balick, B., Heckman, T. 1978, ApJ, 226, L7
- Ballet, J., Caplan, J., Rothenflug, R., Dubreuil, D., Soutoul, A. 1989, A&A, 211, 217
- Berrington, K. A., Nakazaki, S., Norrington, P. H. 2000, A&AS, 142, 313
- Blair, W. P., Davidson, K., Fesen, R.A., et al. 1997, ApJS, 109, 473
- Blinnikov, S., Lundqvist, P., Bartunov, O., Nomoto, K., Iwamoto, K. 2000, ApJ, 532, 1132
- Borkowski, K. J., Shull, J. M. 1990, ApJ, 348, 169
- Brocklehurst, M. 1971, MNRAS, 153, 471
- Brantseg, T., McEntaffer, R. L., Bozzetto, L. M., Filipovic, M., Grieves, N. 2014, ApJ, 780, 50
- Caraveo, P. A., Bignami, G. F., Mereghetti, S., Mombelli, M. 1992, ApJ, 395, L103
- Caraveo, P. A., Mignani, R., Bignami, G. F. 1998, Memorie della Societa Astronomia Italiana, 69, 1061
- Chanam, G. A., Helfand, D. J., Reynolds, S. P. 1984, ApJ, 287, L23
- Charlebois, M., Drissen, L., Bernier, A. -P., Grandmont, F., Binette, L. 2010, AJ, 139, 2083
- Chevalier, R. A. 2006, in Proceedings of 2006 STScI May Symposium on Massive Stars, astro-ph/0607422
- Chieffi, A., & Limongi, M., 2013, ApJ, 764, 21
- Cigan, P., Matsuura, M., Gomez, H. L., et al. 2019, ApJ, 886, 51
- Clark, D. H., Murdin, P., Zarnecki, J. C., Culhane, J. L. 1979, MNRAS, 188, 11
- Danziger, I. J., Dennefeld, M. 1976, PASP, 88, 44
- Davidson, K. 1979, ApJ, 228, 179
- Davidson, K., & Fesen, R. A. 1985, ARA&A, 23, 119
- De Luca, A., Mignani, R. P., Caraveo, P. A., Bignami, G. F. 2007, ApJ, 667, 77
- Del Zanna, G., Dere, K. P., Young, P. R., Landi, E. 2021, ApJ, 999, 38
- Dopita, M. A., Mathewson, D. S. 1979, ApJ, 231, L147
- Dopita, M. A., Seitzzahl, I. R., Sutherland, R. S., Nicholls, D. C., Vogt, F. P., Ghavamian, P., Ruiter, A. J. 2019, AJ, 157, 50
- Dopita, M. A., Tuohy, I. R., 1984, ApJ, 282, 135
- Fesen, R. A., Hurford, A. P., 1996, ApJS, 106, 563
- Fesen, R. A., Weil, K. E., 2020, ApJ, 902, 19
- Ge, M. Y., Lu, F. J., Yan, L. L., et al. 2019, Nature Astronomy, 3, 1122
- Gomez, H. L., Krause, O., Barlow, M. J. et al. 2012, ApJ, 760, 96;
- Gotthelf, E. V., Wang, Q. D. 2000, ApJ, 532, L117
- Greco, E., Miceli, M., Orlando, S., Olmi, B., Bocchino, F., Nagataki, S., Ono, M., Dohi, A., Peres, G. 2021, ApJ, 908, L45
- Gröningsson, P., Fransson, C., Lundqvist, P., et al. 2006, A&A, 456, 581
- Hammer, M., Janka, H.-Th., Müller, E. 2010, ApJ, 714, 1371
- Hamuy, N., J., Suntzeff, N. B., Heathcote, S. R. 1994, PASP, 106, 566
- Henize, K. G. 1956, ApJS, 2, 315
- Hester, J. J. 1998, RevMexAA, 7, 90
- Hwang, U., Petre, R., Holt, S. S., Szymkowiak, A. E. 2001, ApJ, 560, 742
- Jerkstrand, A., Fransson, C., Kozma, C. 2011, A&A, 530, 45
- Kirshner, R. P., Morse, J. A., Winkler, P. F., Blair, W. P. 1989, ApJ, 342, 260
- Kozma, C., Fransson, C. 1998, ApJ, 497, 431
- Krabbe, A. C., Copetti, M. V. F. 2002, A&A, 387, 295
- Lucke, P., Hodge, P.W. 1970, AJ, 75, 171
- Lundqvist, N., Lundqvist, P., Björnsson, C.-I., Olofsson, G., Pires, S., Shibanov, Yu. A., Zyuzin, D. A. 2011, MNRAS, 413, 611
- Lundqvist, P., Lundqvist, N., Vlahakis, C., et al. 2020, MNRAS, 496, 1834
- MacAlpine, G. M., Lawrence, S. S., Sears, R. L., et al. 1996, ApJ, 463, 650
- Manchester, R. N., Mar, D. P., Lyne, A. G., Kaspi, V. M., Johnston, S. 1993a, ApJ, 403, 29
- Manchester, R. N., Staveley-Smith, L., Kesteven, M. J. 1993b, ApJ, 411, 756
- Maran, S. P., Sonneborn, G., Pun, C. S. J., et al. 2000, ApJ, 545, 390
- Martin, T., Milisavljevic, D., Drissen, L. 2021, MNRAS, 502, 186
- Mathewson, D. S., Dopita, M. A., Tuohy, I. R., Ford, V. L. 1980, ApJ, 242, L73
- Mattila, S., Lundqvist, P., Gröningsson, P., Meikle, P., Stathakis, R., Fransson, C., Cannon, R. 2010, ApJ, 717, 1140
- M. Miceli, M., Reale, F., Orlando, S., Bocchino, F. 2006, A&A, 458, 213
- Middleditch, R., N., Pennypacker, C., R. 1985, Nature, 313, 659
- Mignani, R. P., De, A., Hummel, W. et al. 2012, A&A, 544, 100
- Mignani, R. P., Shearer, A., de Luca, A., et al. 2019, ApJ, 871, 246
- Morse, J. A. 2003, Revista Mexicana de Astronomia y Astrofisica Conference Series, 15, 243
- Morse, J. A., Smith, N., Blair, W. P., Kirshner, R. P. et al. 2006, ApJ, 644, 188
- Murdin, P., Clark, D. H., Culhane, J. L. 1978, MNRAS, 183, 79
- Osterbrock, D. E. & Ferland, G. J., 2006. Astrophysics of gaseous nebulae and active galactic nuclei. (Sausalito, CA: University Science Books)
- Owen, P. J. & Barlow, M. J. 2015, ApJ, 801, 141;
- Pavlov, G. G., Zavlin, V. E., Aschenbach, B., Trümper, J., Sanwal, D. 2000, ApJ, 531, L53
- Pietrzyński, G., Graczyk, D., Galloway, A., et al. 2019, Nature, 567, 200
- Raymond, J. C., Edgar, R. J., Ghavamian, P., Blair, W. P. 2015, ApJ, 805, 152,
- Reynolds, S. P. 1985, ApJ, 291, 152
- Rudie, G. C., Fesen, R. A., Yamada, T. 2008, ApJ, 384, 1200
- Sandin, C., Lundqvist, P., Lundqvist, N., Björnsson, C.-I., Olofsson, G., Shibanov, Yu. A. 2013, MNRAS, 432, 2854
- Sauvageot, J. L., Ballet, J., Dubreuil, D., Rothenflug, R., Soutoul, A., Caplan, J. 1990, A&A, 232, 203
- Schmidt, E. W., Schippers, S., Müller, A. 2006 ApJ, 641, L157
- Serafimovich, N. I., Shibanov, Yu. A., Lundqvist, P., Sollerman, J. 2004, A&A, 425, 1041
- Serafimovich N. I., Lundqvist, P., Shibanov, Yu. A., Sollerman, J. 2005, AdSpR, 35, 1106
- Seward, F. D., Harnden, F. R., Jr., Helfand, D. J. 1984, ApJ, 287, L19
- Sieverding, A., Müller, B., Qian, Y. -Z. 2020, ApJ, 904, 163
- Tananbaum, H. 1999, IAU Circ. 7246, 1
- Testor, G., Niemela, V. 1998, A&AS, 130, 527
- Tziamtzis, A., Schirmer, M., Lundqvist, P., Sollerman, J. 2009, A&A, 497, 167
- Van Hoof, P. A. M. 2018, Galaxies, 6, 63
- Vogt, F. P., Seitzzahl, I. R., Dopita, M. A., Ghavamian, P., 2017, A&A, 602, L4
- Williams, B. J., Borkowski, K. J., Reynolds, S. P., et al. 2008, ApJ, 687, 1054
- Wongwathanarat, A., Müller, E., Janka, H.-Th. 2015, A&A, 577, A48
- Yang, H., & Chevalier, R. A. 2015, ApJ, 816, 153

Table 3. Dereddened line fluxes relative to H β and line velocity in H II regions along the VLT “slit 1”.

Line	(F1) 8'' from pulsar			(F2) 25'' from pulsar			(F3) 62'' from pulsar		
	Measured (Å)	flux ^a	velocity ^b (km s ⁻¹)	Measured (Å)	flux ^c	velocity ^b (km s ⁻¹)	Measured (Å)	flux ^d	velocity ^b (km s ⁻¹)
[O II] $\lambda\lambda 3726, 3729^e$	3730.8	478.3	270 \pm 70	3729.7	756.3	180 \pm 10	3730.6	529.8	250 \pm 60
H I $\lambda 3771$							3773.5	5.2	230 \pm 90
H I $\lambda 3798$				3799.7	20.1	140 \pm 50	3800.7	5.6	220 \pm 90
H I $\lambda 3835$				3838.7	23.2	260 \pm 50	3838.7	8.0	260 \pm 80
[Ne III] $\lambda 3869$	3872.9	37.1	320 \pm 60	3871.8	146.3	230 \pm 50	3872.1	21.1	260 \pm 10
H I + He I $\lambda 3889$	3894.6	28.0	430 \pm 150	3892.2	26.9	260 \pm 20	3892.3	20.6	270 \pm 10
Ca II $\lambda 3934$	3939.2	26.3	420 \pm 110	3941.3	12.5	580 \pm 180	3937.6	4.3:	120 \pm 200
[Ne III] + Ca II + H I ^f	3972.6	35.9	300 \pm 70	3971.5	68.9	210 \pm 40	3972.9	25.1	320 \pm 50
He I $\lambda 4026$							4031.2	4.2:	370 \pm 90
[S II] $\lambda 4069^g$	4072.6	26.8		4072.9	11.9		4072.6	4.0	
[S II] $\lambda 4076^g$	4082.9	13.9		4080.9	5.5		4080.9	2.3	
H δ	4107.3	24.3	410 \pm 50	4105.2	34.6	260 \pm 30	4105.7	26.8	300 \pm 30
[Fe V] $\lambda 4227$	4231.7	10.0	320 \pm 70	4231.0	17.6	270 \pm 40			
[Fe II] $\lambda 4244$	4248.3	8.0	250 \pm 100						
[Fe II] $\lambda 4287$	4293.2	7.3	400 \pm 90				4291.5	2.3:	290 \pm 90
H γ	4346.2	44.4	400 \pm 50	4344.2	55.7	260 \pm 20	4344.8	47.1	300 \pm 40
[O III] $\lambda 4363$	4367.1	25.5	270 \pm 50	4367.0	79.3	270 \pm 10	4367.2	6.3	280 \pm 70
He I $\lambda 4471$	4478.7	11.9:	480 \pm 100				4476.2	4.9	320 \pm 60
[Mg I] $\lambda 4563$							4567.5	2.4:	320 \pm 90
Mg I] $\lambda 4571$	4574.4	6.4	220 \pm 100				4576.0	2.2:	320 \pm 110
[Fe III] $\lambda 4658$	4663.2	19.0	330 \pm 80	4661.8	16.3	250 \pm 30	4662.7	11.5	300 \pm 40
He II $\lambda 4686$	4691.3	14.3	360 \pm 90	4690.1	36.3	280 \pm 50			
[Fe III] $\lambda 4702$							4706.5	3.4	320 \pm 60
[Fe III] + [Ar IV] + [Ne IV] ^j	4713.8	14.9	300 \pm 70	4717.3	15.0	380 \pm 90			
He I $\lambda 4713$							4718.6	1.5:	340 \pm 90
[Ne IV] $\lambda 4726$				4730.2	8.3	290 \pm 30			
[Fe III] $\lambda 4734$	4738.2	16.5	270 \pm 80				4738.9	1.0:	320 \pm 100
[Ar IV] $\lambda 4740$				4744.3	8.8	260 \pm 30			
[Fe III] $\lambda 4755$	4760.6	6.0	360 \pm 110				4759.2	2.0:	290 \pm 50
[Fe III] $\lambda 4769$							4774.8	1.8:	340 \pm 60
[Fe III] $\lambda 4778$	4781.7	7.0	240 \pm 100				4782.4	0.9:	290 \pm 80
[Fe II] $\lambda 4814$	4820.8	7.1	400 \pm 90						
H β	4867.9	100	410 \pm 60	4865.4	100	260 \pm 10	4866.2	100	310 \pm 20
[Fe III] $\lambda 4881$	4886.6	6.9	350 \pm 80	4885.0	7.1	250 \pm 50	4885.9	3.4:	300 \pm 70
He I $\lambda 4922$							4927.4	3.0:	340 \pm 70
[O III] $\lambda 4959$	4965.0	121.1	370 \pm 20	4963.4	455.0	270 \pm 10	4963.9	75.6	300 \pm 30
[Fe III] $\lambda 4986$	4991.9	8.2	350 \pm 50	4990.3	15.8	260 \pm 60	4990.9	14.5	300 \pm 50
[O III] $\lambda 5007$	5013.2	358.8	390 \pm 20	5011.5	1370.2	290 \pm 10	5011.9 ^h	222.2	310 \pm 10
[Fe II] $\lambda 5112$	5120.2	9.9	500 \pm 90						
[Fe II] $\lambda 5159$	5165.4	16.9	390 \pm 100				5162.9	2.5:	240 \pm 100
[N I] $\lambda\lambda 5198-5200$	5211.0	8.7:	680 \pm 240				5201.9	2.5:	160 \pm 140
[Fe III] $\lambda 5270$	5274.6	19.2	240 \pm 80	5276.0	7.6	320 \pm 70	5275.9	6.4	310 \pm 80
[Fe XIV] $\lambda 5303$ + [Ca V] $\lambda 5309$	5311.3	9.8	300 \pm 100						
[Fe II] $\lambda 5334$	5340.2	5.9	380 \pm 90						
[Ar X] $\lambda 5534$	5537.9	8.0	210 \pm 60						
[Fe VII] + [Fe II] $\lambda 5721$	5724.6	15.2	270 \pm 80						
He I $\lambda 5876$	5883.4	13.5	400 \pm 70	5881.2	11.9	290 \pm 60	5881.8	12.2	310 \pm 70

^a The flux of H β is 3.4×10^{-16} ergs cm⁻² s⁻¹^c The flux of H β is 8.1×10^{-16} ergs cm⁻² s⁻¹^e [O II] $\lambda 3727.5$ was used for velocity estimate^g Deblending for [S II] was carried out assuming Gaussian line profiles^b Not corrected for the LMC redshift (~ 270 km s⁻¹)^d The flux of H β is 2.1×10^{-15} ergs cm⁻² s⁻¹^f For velocity estimate used $\lambda 3968.67$ ^h He I $\lambda 5015$ detected in the red wing of [O III] $\lambda 5007$, but flux is uncertain.

Table 4. Dereddened line fluxes relative to H β and line velocities in H II regions along the VLT “slit 3”.

Line	(F4)			(F5)		
	Measured (Å)	flux ^a	velocity ^b (km s ⁻¹)	Measured (Å)	flux ^c	velocity ^b (km s ⁻¹)
[O II] $\lambda\lambda 3726, 3729^d$	3729.2	299.6	140 \pm 50	3729.5	377.1	160 \pm 60
H I $\lambda 3798$	3802.1	12.6	330 \pm 80	3802.0	7.4	330 \pm 50
H I $\lambda 3835$	3837.7	7.1	180 \pm 90			
[Ne III] $\lambda 3869$	3871.6	48.1	220 \pm 20	3871.5	80.3	210 \pm 20
H I + He I $\lambda 3889$	3891.7	18.8	220 \pm 30	3892.7	24.9	290 \pm 30
[Ne III] + H I + Ca II ^e	3971.9	31.5	240 \pm 50	3971.4	38.3	210 \pm 40
[S II] $\lambda\lambda 4069, 4076$	4072.5	10.6		4071.5	8.3	
H δ	4104.8	29.8	230 \pm 40	4104.9	24.3	230 \pm 40
[Fe V] $\lambda 4227$	4230.5	3.3:	230 \pm 110	4230.0	6.7	200 \pm 90
H γ	4343.9	46.3	250 \pm 20	4343.9	44.4	240 \pm 20
[O III] $\lambda 4363$	4366.5	17.0	230 \pm 30	4366.6	41.2	240 \pm 30
He I $\lambda 4471$	4475.2	4.0	250 \pm 90	4472.6	5.4	80 \pm 140
[Fe III] $\lambda 4658$	4661.5	8.0	230 \pm 80	4661.7	10.5	230 \pm 50
He II $\lambda 4686$	4690.1	8.3	290 \pm 80	4689.8	13.6	270 \pm 60
[Ar IV] $\lambda 4711$ + [Ne IV] $\lambda 4714^f$				4716.5	5.7	240 \pm 70
[Ar IV] $\lambda 4740$				4743.3	3.3	200 \pm 100
[Fe III] $\lambda 4756$				4758.1	3.2	210 \pm 110
H β	4865.1	100	240 \pm 10	4865.1	100	240 \pm 10
[O III] $\lambda 4959$	4963.3	186.0	260 \pm 10	4963.1	282.2	260 \pm 20
[Fe III] $\lambda 4986$	4989.9	7.1	230 \pm 80	4990.8	10.3	290 \pm 60
[O III] $\lambda 5007$	5011.2	553.9	270 \pm 10	5011.1	851.8	260 \pm 10
[Fe II] $\lambda 5159$	5163.4	2.5:	270 \pm 100	5163.7	4.2	290 \pm 90
[Fe III] $\lambda 5270$	5276.3	3.3:	330 \pm 120	5275.6	4.8	290 \pm 80
[Fe XIV] $\lambda 5303$ + [Ca V] $\lambda 5309$	5312.8	11.5	380 \pm 110	5308.9	7.3	170 \pm 90
He I $\lambda 5876$	5880.3	12.0	240 \pm 50	5880.8	12.4	270 \pm 40

^a The flux of H β is 1.8×10^{-15} ergs cm⁻² s⁻¹^c The flux of H β is 1.0×10^{-15} ergs cm⁻² s⁻¹^e Velocity estimated using 3968.67^b Not corrected for LMC redshift (~ 270 km s⁻¹)^d [O II] $\lambda 3727.5$ was used for velocity estimate^f Velocity estimated using mean value

Table 5. Temperatures¹ in SNR 0540-69.3 and neighboring filaments along the VLT slits “1” and “3” (cf. Fig. 1) estimated from the intensity ratio of [O III] $\lambda\lambda 4959, 5007$ to [O III] $\lambda 4363$, and assuming $E(B - V) = 0.19$.

	Source	Temperature (10^4 K)
Slit 1	SNR 0540-69.3	2.35 ± 0.18^2
	F1 (full line)	3.6 ± 0.4
	F1 (unresolved component only)	≥ 5.5
	F2	3.0 ± 0.4
	F3	1.8 ± 0.2
Slit 3	F4	1.9 ± 0.2
	F5	2.5 ± 0.4

¹ Temperatures were estimated using the method and atomic data described in Sect. 3.3.2.

² [O III] $\lambda 4363$ was deblended from a contribution of H γ (see text).